A Novel Method for Studying Nucleated Pathways in Membranes: Development and Applications for Gene Delivery

Thesis by

Christina L. Ting

In Partial Fulfillment of the Requirements

for the Degree of

Doctor of Philosophy

California Institute of Technology

Pasadena, California

2013

(Defended August 27, 2012)

Acknowledgments

First and foremost, I am grateful to my advisor, Zhen-Gang Wang. His patience, honesty, and encouragement during my time at Caltech has been instrumental in my scientific and personal growth. It has been a pleasure to be the student of such an inspirational person.

I am thankful to Kathy Bubash and Alison Ross for welcoming me to Caltech, and later for always being helpful and positive. I am also thankful to the past and present members of the Wang group for their support, especially to Brad for his mentorship, Issei for taking care of Kiki, and Bilin for organizing the group lunches and hikes.

I wish to thank the members of my committee, William Clemons, Mark Davis and Doug Rees, for helpful discussions on the work done in this thesis.

Of course, my friends and family have made this experience a lot more enjoyable. BG, Steve, Cindy, Aron: thanks for keeping life at and around Caltech fun, I hope part of us never grows up. Special thanks to Aron for not giving up on me during this time. To my cycling friends: thanks for all the adventures in the mountains (asphalt and dirt). These rides have kept me sane. To my family: thanks for your ongoing love and support.

Finally, I want to express my gratitude to Daniel. I could not have done this without you.

Abstract

The development of a safe, selective, and efficient gene delivery system is key to the success of human gene therapy. In polymer-based gene delivery systems, biocompatible polymers electrostatically bind and condense the genetic material into protective nanoparticles. These nanoparticles must subsequently overcome several challenges, which remain poorly understood. In particular, once internalized by the cell, the nanoparticles are trapped inside a membrane-bound compartment called the endosome. In the proton sponge hypothesis, the buffering capacity of the polymers leads to an increase in osmotic pressure that eventually ruptures the endosomal membrane and releases the trapped nanoparticles.

To obtain a mechanistic understanding of the endosomal escape, we first develop a coarse-grained model to study the equilibrium interaction between a positively charged nanoparticle and a lipid membrane. Results indicate the existence of a pore with an inserted particle, whose metastability depends on the membrane tension and particle properties (size and charge). These pores are subsequently shown to lower the critical tension necessary for membrane rupture, thus possibly enhancing the release of the trapped genetic material from the endosome.

Next, we address the actual escape pathway, which is likely a thermally nucleated process and cannot be simulated directly or studied by equilibrium methods. Hence, we develop a novel method for studying minimum free energy paths in membranes. Our results indicate that thermally nucleated rupture may be an important factor for the low rupture strains observed in lipid membranes. Under the moderate tensions found in this regime, there are multiple pathways for crossing the membrane: (1) particle-assisted membrane rupture, (2) particle insertion into a metastable pore followed by translocation and membrane resealing, and (3) particle insertion into a metastable pore followed by membrane rupture. This suggests a direct role of the nanoparticle in the endosomal escape not previously envisioned in the proton sponge hypothesis, and illustrates the importance of having an induced tension on the membrane.

Finally, the methodology developed in this work represents the most advanced theoretical technique for describing nucleation pathways in soft condensed matter systems that also include hard-particle degrees of freedom. We expect the method to be useful for studying a wide range of nucleation phenomena beyond membrane systems, for example, in nanoparticle polymer composites.

Contents

List of Figures

List of Tables

Chapter 1

Introduction

Gene therapy is the insertion of a corrective gene into cells to alleviate the symptoms of disease. With advances in the identification of the genetic and molecular origins of diseases, gene therapy holds the potential to treat hereditary diseases by replacing errant genes and nonhereditary diseases by delivering genes to alter the production of naturally occurring or cytotoxic proteins. The latter may be used to treat diseases such as cancer and acquired immunodeficiency virus (AIDS). While simple in principle, several issues remain to be overcome before gene therapy can be successfully applied in the clinic. The primary challenge is developing an efficient method for delivering the gene to the target cells [1–3]. In this thesis we will address the intracellular barriers associated with the gene delivery issue.

The delivery of the genetic material to the nucleus is achieved through the use of delivery vectors, which can be divided into two major categories: viral and nonviral. Although viral vectors are extremely efficient, serious safety concerns limit their clinical applications [4–6]. In contrast, nonviral vectors, which rely on cationic molecules to electrostatically complex with the nucleic acids into protective nanoparticles, are less toxic and less immunogenic [7]. We will consider cationic polymers, which have the added benefit of facile preparation with immense flexibility to incorporate multiple features, such as targeting ligands. However, to achieve an efficiency comparable to that of their viral vector counterparts, a mechanistic understanding of each step during the gene delivery process is still needed, including: the formation and stability of the nanoparticles; the systemic delivery and targeting; the internalization, endosomal escape, cytoplasmic trafficking and nuclear transport;

and finally the unpackaging of the nucleic acid from the nanoparticle and incorporation into the genome [8]. While many of the above issues involve detailed biochemistry, some are clearly physical in nature can be addressed with theory and simulation, using concepts in polymer and membrane biophysics. In particular, the motivation for this thesis will be to address the endosomal escape mechanism.

Understanding the endosomal escape mechanism is critical for the design of efficient polymer-based gene delivery systems. Once the nanoparticle is internalized by the cell, it becomes trapped inside a membrane-bound compartment called the endosome. At later stages, the endosome fuses with the lysosome, a vesicle specialized for the intracellular digestion of macromolecules. Hence, the nanoparticle containing the polymer-gene complex must escape or face degradation. In the proton sponge hypothesis [9–11], it is believed that the buffering capacity of the polymers leads to an increase in osmotic pressure that translates to increased tension on the endosomal membrane. Eventually, the membrane forms pores and ruptures, thus releasing the trapped nanoparticles into the cytosol.

Two biophysical questions arise naturally from the proton sponge hypothesis: *How does a membrane form a pore and rupture? And can the nanoparticle interact with the membrane to play a direct role (beyond simply serving as substrate for protonation) in this process?* Though apparently simple, these questions remain unanswered and are fundamental to understanding how to design nanoparticles that can successfully escape the endosome. Our goal is to provide a molecular-level picture of these processes. This has required substantial efforts in developing new computational tools capable of capturing the essential features of these complex biological systems and the time scales of these events.

We have developed a coarse-grained model consisting of amphiphilic, double-tailed lipids in explicit solvent with added salt ions. Importantly, the model accounts for both the short-ranged hydrophobic interactions and the long-range Coulomb interactions of the hydrophobic tails and the negatively charged head groups, respectively, as well as the lipid chain configurational entropy. This difficult many-body problem is converted into a one-body problem, using a well-established tech-

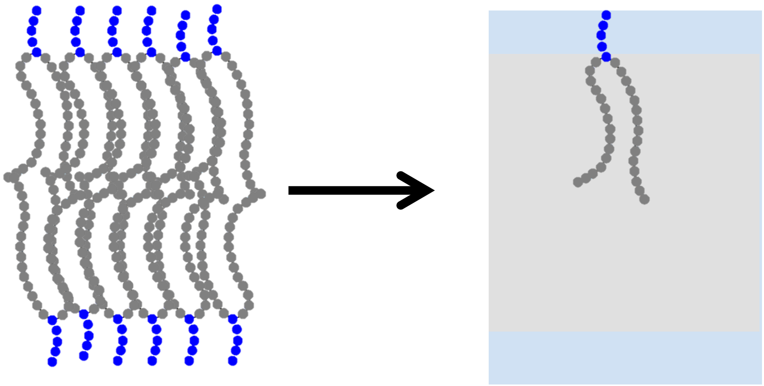

Figure 1.1: Schematic of the self-consistent (mean) field theory: replacing the interactions among molecules with the interaction between a single molecule and an average external field [12]

nique in the polymer community known as the self-consistent field theory (SCFT); see Fig. 1.1. In Chapter 2, we use this model to study the equilibrium interaction between a positively charged nanoparticle and a lipid membrane as a function of the particle size, charge, and membrane tension. For moderately high membrane tensions and for nanoparticles comparable to the membrane thickness, we find a metastable pore state (Fig. 1.2) that significantly reduces the critical tension for the mechanical rupture of the membrane, defined as the limit of metastability. This suggests that if the nanoparticle can insert into the membrane, the endosomal escape is enhanced. However, the kinetic pathways for particle insertion and the subsequent membrane rupture cannot be addressed with the equilibrium calculations used in this study. Furthermore, membranes are examples of soft matter systems that can undergo many interesting processes as thermally nucleated *(rare)* events; particle insertion and rupture are two likely examples.

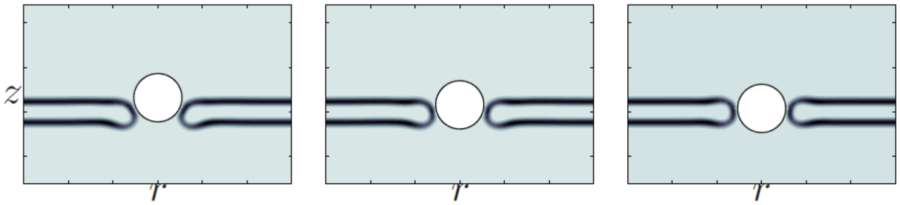

Figure 1.2: Solutions to the SCFT equations, where the particle position is fixed. The rightmost image corresponds to the metastable pore state. Contour plot shows the lipid head density in cylindrical coordinates.

Developing a method to study rare events in soft matter systems is a difficult problem due primarily to the following challenges:

1. *Long timescales:* Conventional molecular dynamics simulations attempt to overcome the long timescales by setting up the system in such an unstable state that the phase transition occurs instantaneously, i.e., via spinodal decomposition, rather than nucleation.
2. *High dimensional reaction coordinate:* The potential of mean constraint force method artificially selects a reaction coordinate constraint that, in general, does not coincide with the true transition pathway involving the many molecular degrees of freedom.
3. *Complex molecules:* Simple toy models are developed in an effort to reduce the computational load of the problem. The interpretation of structures comparable to the molecular size is highly problematic for these overly simplified models.

We have developed a novel approach that overcomes all of the aforementioned challenges. The method captures the full minimum free energy path (MFEP) of nucleated events by using a string [13] to identify the pathway for barrier crossing on a known free energy landscape. In SCFT the free energy functional is not known *a priori*. Thus we traverse the free energy landscape by evaluating the gradients "on the fly" [14–16].

In Chapter 3, we present results showing that the free energy barrier for pore formation and rupture becomes surmountable well before the onset of mechanical instability of the membrane, thus offering a possible explanation for the low rupture strains observed in lipid membranes [17]. In Chapter 4, we further demonstrate that the nanoparticle is able to insert into pores and either translocate or assist in the rupture of the membrane. From a practical point of view, this result suggests that engineering the nanoparticle to interact with the membrane in a way that lowers the nucleation barrier in these pathways can be an effective way to increase the endosomal escape rate.

To achieve efficiencies comparable to the viral vectors, it may be necessary to combine multiple tactics for overcoming the endosomal escape barrier. Recent experiments suggest that if there are excess cationic polymers that have not condensed with the genetic material into nanoparticles, the endosomal escape is enhanced [18,19]. The effects of these free polymers are hypothesized to be twofold. First, the polymer can insert into the endosomal membrane, thereby decreasing the mechanical strength and lowering the nucleation barrier for membrane rupture. Second, if these polymers are only partially inserted into the membrane, then the polymer segment sticking out may obstruct the fusion of the endosome with lysosomal vesicles containing hydrolytic enzymes. Results from Chapters 3 and 4 already suggest that rupture of the endosomal membrane is a nucleated event and that the nanoparticle can directly assist in lowering this barrier. Future studies are expected to reveal whether these free polymers can be used to further enhance the endosomal escape. A molecular picture of the pathways associated with these processes is obtainable for the first time using the method developed in this thesis.

Although the focus of this thesis is on the endosomal escape of polymer-based gene delivery systems, the guiding principle used here can be extended to the investigation of other biophysical problems. We have shown that coarse-grained models solved using appropriate computational methods can provide interesting insights into seemingly complex biological systems. In Chapter 5, two additional studies in line with this theme are included. First, we develop a kinetic model to describe the dynamics of cellulase, a two-domain enzyme that converts biomass into biofuels. This study revealed the role of the flexible linker region for achieving an optimal hydrolysis rate. Second, we define a thermodynamic model for the self-assembly of RNA viruses. Using this model, we were able to explain—for the first time—the source of the net negative charge that is prevalent in naturally occurring viruses, a topic of considerable controversy in the virology community.

Bibliography

[1] R. C. Mulligan, *Science* **260**, 926 (1993).

[2] I. M. Verma and N. Somia, *Nature* **389**, 239 (1997).

[3] M. Nishikawa and L. Huang, *Human Gene Therapy* **12**, 861 (2001).

[4] A. D. Miller, *Nature* **357**, 455 (1992).

[5] M. A. Kay, J. C. Glorioso, and L. Naldini *Nat. Med.* **7**, 33 (2001).

[6] C. E. Thomas, A. Ehrhardt, and M. A. Kay *Nat. Rev. Genet.* **4**, 346 (2003).

[7] M. A. Mintzer and E. A. Simanek *Chem. Rev.* **109**, 259 (2009).

[8] D. W. Pack, A. S. Hoffman, S. Pun, and P. S. Stayton, *Nat. Rev. Drug Discov.* **4**, 581 (2005).

[9] J. Haensler and F. C. Szoka, *Bioconjugate Chem.* **4**, 372 (1993).

[10] J. P. Behr, *Chimia.* **51**, 34 (1997).

[11] N. D. Sonawane, F. C. Szoka, and A. S. Verkman, *J. Biol. Chem.* **278**, 44826 (2003).

[12] G. H. Fredrickson, *The Equilibrium Theory of Inhomogeneous Polymers* (Oxford University Press, New York, 2005).

[13] W. N. E, W. Q. Ren, and E. Vanden-Eijnden, *Phys. Rev. B* **66**, 052301 (2002).

[14] J. Fraaije, *J. Chem. Phys.* **99**, 9202 (1993).

[15] N. M. Maurits and J. G. E. M. Fraaije, *J. Chem. Phys.* **107**, 5879 (1997).

[16] S. W. Sides, B. J. Kim, E. J. Kramer, and G. H. Fredrickson, *Phys. Rev. Lett.* **96**, 250601 (2006).

[17] K. Olbrich, W. Rawicz, D. Needham, and E. Evans, *Biophys. J.* **79**, 321 (2000).

[18] S. Boeckle, K. von Gersdorff, S. van der Piepen, C. Culmsee, E. Wagner, and M. Ogris, *J. Gene Med.* **6**, 1102 (2004).

[19] Y. Yue, F. Jin, R. Deng, J. Cai, Y. Chen, M. C. M. Lin, H.-F. Kung, and C. Wu, *J. Control. Release* **155**, 67 (2011).

Chapter 2

Interactions of a Charged Nanoparticle with a Lipid Membrane: Implications for Gene Delivery

We use self-consistent field theory to study the thermodynamics of membrane-particle interactions in the context of polymer-based gene delivery systems. Our aim is to guide the design of dendrimers that can overcome the endosomal escape barrier by inserting into membranes and creating pores. We study the interaction between a dendrimer, which we model as a nanoparticle, and a membrane under controlled tension as a function of their separation. In all the cases considered, the lowest free energy state corresponds to the particle absorbing onto the surface of the membrane. However, with moderate tension, we find that a G5 (or larger) generation dendrimer, through thermal fluctuation, can insert into membranes to form metastable pores. These pores are subsequently shown to significantly lower the critical tension necessary for membrane rupture, thus possibly enhancing the release of the trapped genetic material from the endosomal vesicle [1].

2.1 Introduction

Polymer-based synthetic vectors hold great promise as gene delivery vehicles. They afford immense flexibility in design, are easy to manufacture, and allow repeated administration without adverse immune responses. The synthetic vectors rely on the ability of the positively charged polymers to electrostatically bind and condense the genetic material into nanoparticles, which are termed polyplexes. Rational design of an efficient gene delivery vehicle requires a mechanistic understanding of each step during the gene delivery process, including the formation and stability of the polyplexes; the systemic delivery and targeting; the cellular internalization, endososomal escape, cytoplasmic trafficking and nuclear transport; and finally the unpackaging of the nucleic acid from the polyplex and incorporation into the genome [2].

In this thesis, we focus on the endosomal escape mechanism. As the polyplex is trafficked from the endosome to the lysosome, acidification activates hydrolytic enzymes that degrade the trapped genetic material. In the proton sponge hypothesis [3–5], it is believed that cationic polymers are able to avoid this fate by absorbing the protons. This causes the polymer to swell and additional protons to be pumped into the endosome. Together with an attendant influx of counterions, this results in an increase in osmotic pressure that eventually ruptures the membrane and releases the trapped polyplexes into the cytosol.

In addition to the proton sponge effect of the polymers, it has been experimentally shown that nonspecific interactions between free polyamidoamine (PAMAM) dendrimers and lipid membranes enhance membrane permeability and hole formation, depending on dendrimer size (generation, G) and charge (terminal functional groups) [6–9]. Specifically, G7 amine-terminated dendrimers induce the formation of holes, while G5 amine-terminated dendrimers primarily expand pre-exisiting defects, and G5 acetamide-terminated (charge neutral) dendrimers do not cause hole formation. With respect to overcoming the endosomal escape barrier, these observations, together with results indicating that the presence of excess free polymers can increase the transfection efficiency by two orders of magnitude [10, 11], suggest that a molecular understanding of the membrane-particle interactions can provide a foundation for the design of dendrimers as efficient gene delivery vehicles (in what follows, we use the terms dendrimer and particle interchangeably).

Towards this end, recent advances in computation power and simulation methodologies have produced interesting observations that both complement the experimental findings and provide additional molecular-level insights [12]. In particular, Lee and Larson have performed coarse-grained

MD simulations of G3 to G7 dendrimers on a dipalmitoylphosphatidylcholine (DPPC) bilayer. Their results suggest that the dendrimer is more efficient in inducing membrane permeability, as compared to flexible linear polymers, because its rigid spherical structure prefers to gain favorable electrostatic interactions from both leaflets, thus facilitating the formation of a pore [13].

Here we use self-consistent field theory (SCFT) [14] to explore the structural and energetic properties of metastable and unstable states involved in dendrimer-induced pore formation and membrane rupture. In comparison to direct molecular simulation, SCFT allows access to both true equilibrium and metastable states without limitations due to short simulation times. Furthermore, thermodynamic variables such as the membrane tension are easily and directly controlled. We seek to understand how the effect of the dendrimer is coupled to the effect of the tension in the membrane. Our aim is to find conditions favoring the formation of a metastable pore, which we show can nucleate membrane rupture. As was demonstrated by Lee and Larson [13], this requires properly treating the electrostatics. In particular, we account for the spatially varying dielectric constant and include the Born energy of the ions [15]. Although SCFT has been applied to similar systems, electrostatic effects from charged species were not included [16, 17]. Thus, we begin with a brief description of the model and SCFT derivation.

2.2 Model

Our system consists of a membrane bilayer assembled from double-tailed lipids (L) in solvent (S) with salt ions ($\pm$). The lipids are represented as graft copolymers, which we model as discrete Gaussian chains, consisting of a negatively charged head segment of N_H solvophilic head monomers with volume v_H and two identical tail segments, each consisting of N_T solvophobic tail monomers with volume v_T, see Fig. 2.1. The harmonic potential for the connectivity of chain i takes the form

$$h_i = \frac{3k_BT}{2b^2}\sum_{j=1}^{N-1}(\mathbf{r}_{i,j+1} - \mathbf{r}_{i,j})^2. \tag{2.1}$$

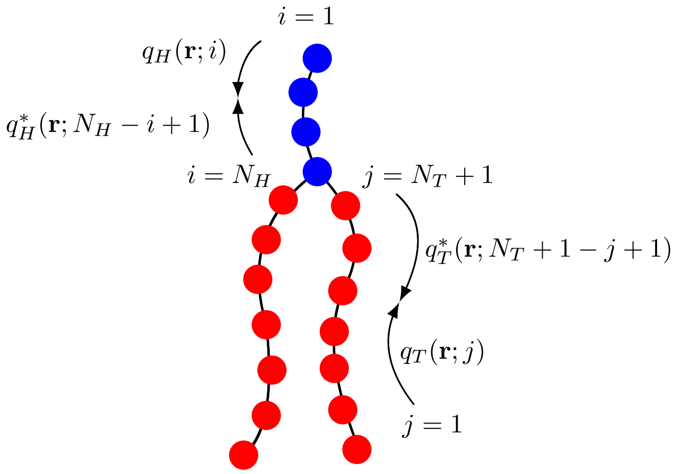

Figure 2.1: A double-tailed lipid model consisting of head (blue) and tail (red) monomers. q_I and q_I^*, where $I=H,T$, are the chain propagator and complementary chain propagator, respectively, used for calculating the single chain statistics; see Appendix C.

Here $\mathbf{r}_{i,j}$ is the position of the jth monomer in the ith chain, b is the bond length, N is the total number of monomers in the chain, k_B is the Boltzman constant, and T is the temperature. In what follows, we set $k_{\mathrm{B}}T=1$. We note that in using the discrete Gaussian chain as our model, we have ignored bending rigidity. Indeed, real lipid molecules have bonds with limited flexibility; in particular, unsaturated lipids contain double bonds, or kinks. However, bond order parameters calculated from similar lattice models [18–20] in the same spirit as our discrete Gaussian chain model have shown good qualitative agreement with experimental findings [21–23], and even excellent agreement with molecular dynamics simulations [24–26]. We use the Gaussian model primarily for convenience, as it is the simplest model that captures the conformational degrees of freedom of the lipid molecules. Similar models have been used to study membrane processes such as fusion [27].

In addition to the lipids, there are solvent monomers with volume v_S, and salt ions taken as point charges of elementary electron charge e and valency $z_\pm$. We work mostly in the grand canonical ensemble, where the number of lipid, solvent, and ion molecules are controlled by their chemical potentials μ_I $(I=L,S,\pm)$, which are obtained from the homogeneous bulk phase. For a range of dendrimer generations and charge densities, we calculate the free energy of the system as a function of the dendrimer position with respect to the membrane. In other words, we include a fixed dendrimer in the system, whose position and density profile we specify, and solve for the remaining density profiles of the lipids, solvents, and ions; the free energy follows immediately from these solutions.

We begin with a particle-based Hamiltonian for our system, given by

$$\mathcal{H} = \sum_{i=1}^{n_L} h_i + \int d\mathbf{r}d\mathbf{r}' \left\{ \sum_{JK} \hat{\phi}_J(\mathbf{r}) u_{JK}(\mathbf{r}-\mathbf{r}') \hat{\phi}_K(\mathbf{r}') + \frac{e^2}{2}\hat{\rho}_c(\mathbf{r}) C(\mathbf{r},\mathbf{r}') \hat{\rho}_c(\mathbf{r}') + \frac{z_\pm^2 e^2 \hat{c_\pm}(\mathbf{r})}{8\pi a_\pm \epsilon(\mathbf{r})} \right\}. \tag{2.2}$$

In this expression, the first term accounts for the chain connectivity of the n_L lipids. The second term accounts for the pairwise energetic interaction potentials among species, where the summation is over $JK \in \{HT, TS, SH\}$ and the instantaneous volume fractions of solvent, head, and tail monomers are defined

$$\begin{aligned} \hat{\phi}_S(\mathbf{r}) &= v_S \sum_{j=1}^{n_S} \delta(\mathbf{r}-\mathbf{r}_j), \\ \hat{\phi}_H(\mathbf{r}) &= v_H \sum_{i=1}^{n_L} \sum_{a=1}^{N_H} \delta(\mathbf{r}-\mathbf{r}_{ia}), \\ \hat{\phi}_T(\mathbf{r}) &= 2v_T \sum_{i=1}^{n_L} \sum_{b=1}^{N_T} \delta(\mathbf{r}-\mathbf{r}_{ib}). \end{aligned} \tag{2.3}$$

We assume the pairwise interaction potential $u_{JK}(\mathbf{r}-\mathbf{r}')$ to be short-ranged, so that one may perform a gradient expansion to quadratic order; see Appendix A. This gives the following approximation:

$$\begin{aligned} \mathcal{H} \approx \sum_{i=1}^{n_L} h_i + \int d\mathbf{r}d\mathbf{r}' \Bigg\{ & \sum_{JK} \left[\hat{\phi}_J(\mathbf{r}) \chi_{JK} \hat{\phi}_K(\mathbf{r}) + \frac{\kappa_J}{2} |\nabla \hat{\phi}_J(\mathbf{r})|^2 \right] \\ & + \frac{e^2}{2}\hat{\rho}_c(\mathbf{r}) C(\mathbf{r},\mathbf{r}') \hat{\rho}_c(\mathbf{r}') + \frac{z_\pm^2 e^2 \hat{c_\pm}(\mathbf{r})}{8\pi a_\pm \epsilon(\mathbf{r})} \Bigg\}. \end{aligned} \tag{2.4}$$

Here, the local interactions are captured by the terms containing the Flory χ parameters and non-local interactions are captured by the gradient terms [28]. We comment that in modeling systems involving long polymers, such gradient terms are usually not included, as the chain connectivity is sufficient to capture the nonlocal effects on length scales of interest. Because we are treating shorter chains, we include these terms to account for nonlocal effects at shorter length scales due to the short chain nature of the lipids.

The third term in Eq. (2.4) is the Coulomb energy of the system, where

$$C(\mathbf{r},\mathbf{r}') = \frac{1}{4\pi\epsilon|\mathbf{r}-\mathbf{r}'|} \tag{2.5}$$

is the Coulomb operator satisfying $[-\nabla\cdot(\epsilon\nabla)]C(\mathbf{r},\mathbf{r}') = \delta(\mathbf{r}-\mathbf{r}')$. Later, it will be useful to note that its inverse operator is

$$C^{-1}(\mathbf{r},\mathbf{r}') = -\epsilon\nabla^2\delta(\mathbf{r}-\mathbf{r}'). \tag{2.6}$$

The Coulomb energy accounts for the long-ranged electrostatic interactions from the total charge density of all charged species:

$$e\hat{\rho}_c(\mathbf{r}) = c_F\phi_F(\mathbf{r}) - \frac{c_H}{v_H}\hat{\phi}_H(\mathbf{r}) + z_+e\hat{c}_+(\mathbf{r}) - z_-e\hat{c}_-(\mathbf{r}). \tag{2.7}$$

Here c_F is the magnitude of the charge density on the fixed dendrimer and c_H is the magnitude of the charge per head monomer (and is dimensionless). $\hat{c}_\pm(\mathbf{r})$ is the instantaneous number density of the ions. Note that the density profile $\phi_F(\mathbf{r})$ for the dendrimer is specified by us. Any reasonable function may be used. We choose a hyperbolic tangent function with a characteristic width for the interface [29] so that the dielectric constant $\epsilon(\mathbf{r})$, which is spatially varying and depends on the volume fractions of the different species, will be smooth and continuous in $\mathbf{r}$. However, with respect to the lipids, the dendrimer is impenetrable and the density profile of the fixed particle is essentially a step function. Finally, the forth term in Eq. (2.4) is the Born self-energy of the ions in a weakly varying dielectric medium.

The grand canonical partition function Ξ is obtained by summing over all particle degrees of freedom, including the position of each solvent and ion molecule, as well as the position and conformation of each lipid chain:

$$\begin{aligned}\Xi = \sum_{n_{\{L,S,\pm\}}=0}^{\infty} & \frac{\mathrm{e}^{(\mu_L n_L+\mu_S n_S+\mu_\pm n_\pm)}}{n_L!n_S!n_\pm!{v_L}^{n_L}{v_S}^{n_S}{v_\pm}^{n_\pm}}\int\prod_{i=0}^{n_L}\mathcal{D}\mathbf{r}_i\int\prod_{j=0}^{n_S}d\mathbf{r}_j\int\prod_{k=0}^{n_\pm}d\mathbf{r}_k \\ & \times\prod_{\mathbf{r}}\delta\Big[1-\hat{\phi}_H(\mathbf{r})-\hat{\phi}_T(\mathbf{r})-\hat{\phi}_S(\mathbf{r})-\phi_F(\mathbf{r})\Big]\mathrm{e}^{-\mathcal{H}}.\end{aligned} \tag{2.8}$$

Here, the delta functional accounts for the incompressibility at all positions $\mathbf{r}$ within the system volume, the notation $\mathcal{D}\mathbf{r}_i$ is shorthand for integrating over all monomers in the chain, i.e., $\mathcal{D}\mathbf{r}_i \equiv d\mathbf{r}_{i,1} d\mathbf{r}_{i,2} \ldots d\mathbf{r}_{i,N}$, and the Boltzmann factor $\mathcal{H}$ is given by Eq. (2.4).

In SCFT, the first step is to replace the above (computationally intractable) particle-based model with a field-theoretic model, using a series of techniques related to Hubbard-Stratonovich transformations. This decouples the interactions among particles and replaces them with interactions between single particles and effective fields; for details, see Appendix B. The final result for the field-theoretic partition function can be generically written in the form

$$\Xi = \int D\omega \exp(-F[\omega]), \tag{2.9}$$

where F is an effective Hamiltonian that is complex and depends on the (multidimensional) field variable ω. In general, the field-theoretic partition function cannot be evaluated in closed form. The mean-field, or self-consistent field approximation, amounts to assuming that a single field configuration ω^* dominates the functional integral, i.e., $\Xi \approx \exp(-F[\omega^*])$, where $F[\omega^*]$ in our model is given by

$$\begin{aligned} F = & -\frac{\mathrm{e}^{\mu_L}}{v_L} Z_L(\xi_H, \xi_T) - \frac{\mathrm{e}^{\mu_S}}{v_S} Z_S(\xi_S) - \frac{\mathrm{e}^{\mu_\pm}}{v_\pm} Z_\pm(\psi) \\ & + \int d\mathbf{r} \left\{ \sum_{JK} (\chi_{JK}\phi_J\phi_K - \xi_J\phi_J + \frac{\kappa_J}{2}[\nabla\phi_J]^2) + \psi\big(c_F\phi_F - \frac{c_H}{v_H}\phi_H\big) - \frac{\epsilon}{2}(\nabla\psi)^2 \right\}. \end{aligned} \tag{2.10}$$

In Eq. (2.10), and in what follows, we recognize the imaginary nature of the potential field variables at the saddle point and redefine the conjugate chemical potential fields $i\xi \to \xi$, and the electrostatic potential field $-i\psi \to \psi$. Also, the incompressibility constraint is invoked to eliminate ϕ_S in favor of ϕ_H, ϕ_T, and ϕ_F. Finally, the $\mathbf{r}$ dependence has been dropped for notational conciseness.

The partition functions that arise in the above expression are for a single molecule in its respective field(s) and are given by

$$\begin{aligned} Z_S(\xi_S) &= \int d\mathbf{r}\,\exp\{-v_S\xi_S\}, \\ Z_\pm(\psi) &= \int d\mathbf{r}\,\exp\big\{\mp\psi e z_\pm - u^b_\pm\big\}, \\ Z_l(\xi_H,\xi_T) &= \int d\mathbf{r} q_H(\mathbf{r};N_H)q_T^2(\mathbf{r};N_T+1)\mathrm{e}^{2v_H\xi_H}, \end{aligned} \tag{2.11}$$

for the solvents, ions and lipids, respectively. The form of $Z_S(\xi_S)$ is simple enough; $Z_\pm(\psi)$ and $Z_l(\xi_H,\xi_T)$ require some explanation. Firstly, we have introduced the Born self-energy of the ions

$$u^b_\pm = \frac{z_\pm^2 e^2}{8\pi a_\pm \epsilon}, \tag{2.12}$$

where ϵ is the spatially varying dielectric constant. Although the volume of the salt ions does not enter into the incompressibility, with respect to the self-energy of an ion, we specify $a_\pm = 0.3$ nm as the radius. $u^b_\pm$ cannot be absorbed into a redefinition of the chemical potential for a spatially varying dielectric medium. The derivation of the expression for the Born energy of a spatially varying dielectric medium is rather involved and we refer the interested reader to a complete derivation by Wang [15]. Secondly, we have introduced the chain propagator $q_I(\mathbf{r};i)$ for $I = H,T$, where i is the monomer index, to obtain the single-chain statistics of the lipid. The propagator accounts for the chain connectivity and the Boltzmann weight due to the self-consistent potential field. Calculation of the propagator for our discrete Gaussian chain is described in Appendix C, with the initial condition for placing the end monomers:

$$\begin{aligned} q_H(\mathbf{r};1) &= \exp\{-v_H\xi_H\}, \\ q_T(\mathbf{r};1) &= \exp\{-v_T\xi_T\}. \end{aligned} \tag{2.13}$$

The total partition function for a single chain follows naturally by joining the chain propagators at the branch point, where an extra exponential factor $\mathrm{e}^{2v_H\xi_H}$ is included in the partition function to correct for over-counting the joined monomer; see Fig. 2.1.

Finally, the mean-field configuration that gives $F[\omega^*]$ is obtained by requiring that Eq. (2.10) is stationary with respect to variations in the fields. Variation with respect to the volume fraction fields ϕ_H and ϕ_T gives,

$$\begin{aligned}\xi_H =&\xi_S + \chi_{SH}(1-2\phi_H-\phi_T-\phi_F) + (\chi_{HT}-\chi_{ST})\phi_T\\ &-\kappa_H\Delta\phi_H - \frac{c_H}{v_H}\psi - (\epsilon_H-\epsilon_S)\left(\frac{(\nabla\psi)^2}{2}+\frac{z_\pm^2 e^2 c_\pm}{8\pi a_\pm \epsilon^2}\right),\\ \xi_T =&\xi_S + \chi_{ST}(1-\phi_H-2\phi_T-\phi_F) + (\chi_{HT}-\chi_{SH})\phi_H\\ &-\kappa_T\Delta\phi_T - (\epsilon_T-\epsilon_S)\left(\frac{(\nabla\psi)^2}{2}+\frac{z_\pm^2 e^2 c_\pm}{8\pi a_\pm \epsilon^2}\right).\end{aligned} \tag{2.14}$$

Here, $c_\pm = \mathrm{e}^{\mu_\pm} v_\pm^{-1}\exp\big\{\mp z_\pm e\psi - u_\pm^b\big\}$ is the ion distribution. Variation with respect to ψ gives,

$$-\nabla(\epsilon\nabla\psi) = c_F\phi_F - \frac{c_H}{v_H}\phi_H \pm (z_\pm e c_\pm)\,; \tag{2.15}$$

with respect to ξ_S gives,

$$1-\phi_H-\phi_T-\phi_F = \mathrm{e}^{\mu_S}\exp\{-v_S\xi_S\}; \tag{2.16}$$

and with respect to ξ_H and ξ_T gives,

$$\begin{aligned}\phi_H(\mathbf{r}) &= \frac{v_H \mathrm{e}^{\mu_L}}{v_L}\sum_{\mathrm{i}=1}^{N_H} q_H(\mathbf{r};i)\mathrm{e}^{v_H\xi_H} q_H^*(\mathbf{r};N_H-i+1),\\ \phi_T(\mathbf{r}) &= 2\frac{v_T \mathrm{e}^{\mu_L}}{v_L}\sum_{\mathrm{i}=1}^{N_T} q_T(\mathbf{r};i)\mathrm{e}^{v_T\xi_T} q_T^*(\mathbf{r};N_T+1-i+1).\end{aligned} \tag{2.17}$$

Here we have introduced the complementary chain propagator $q_I^*(\mathbf{r};i)$, which also satisfies a similar equation to that for $q_I(\mathbf{r};i)$, but with the initial conditions (for beginning at the branch point):

$$\begin{aligned}q_H^*(\mathbf{r};1) &= \mathrm{e}^{v_H\xi_H} q_T(\mathbf{r};N_T+1)q_T(\mathbf{r};N_T+1),\\ q_T^*(\mathbf{r};1) &= \mathrm{e}^{v_H\xi_H} q_T(\mathbf{r};N_T+1)q_H(\mathbf{r};N_H).\end{aligned} \tag{2.18}$$

Eq. (2.15) is the Born-energy augmented Poisson-Boltzmann equation [15]. Eq. (2.16) can be trivially solved to to yield $\xi_S = -v_S^{-1}\log(1-\phi_H-\phi_T-\phi_F)$, where we have defined $\mu_S \equiv 0$ because the chemical potentials of the solvents and lipids are not independent for an incompressible system. Numerical SCFT requires solving eqs. (2.14–2.17), together with Eq. (C-2) for the chain propagators, iteratively until convergence. From these solutions, the free energy is obtained from Eq. (2.10).

2.3 Results

In this section, we study the thermodynamics of membrane-particle interactions and consider the implications to the endosomal escape, where, in addition to the proton sponge effect, another possible effect of the dendrimers is to insert into the endosomal membrane and form pores that can nucleate rupture at significantly lower tensions. As a reference, we first study the tension required to rupture a uniform membrane in the absence of the dendrimer.

2.3.1 Rupture of a Uniform Lipid Membrane

Lipid membranes such as DPPC are often used as models for understanding the more complex and diverse biological membranes that define the boundaries of (and within) a cell. We begin by developing a coarse-grained model of a lipid membrane in a volume containing explicit solvent and mobile ion species at physiological salt concentration, 150 mM. For the lipid we choose $N_H = 2$ and $N_T = 8$ (per tail), with the monomer volumes $v_H = v_T = 0.05$ nm^3. With these values, the total volume of our lipid is $v_l = 0.9$ nm^3, which is on the order of the value for a lipid in a fully hydrated bilayer ($v_l = 1.232$ nm^3) as determined by Nagle [30]. The desired surface charge density is experimentally obtained by specifying the composition of lipid species in the membrane [31]. For simplicity, we choose to distribute the charge evenly among the head monomers and set $c_H = 0.25$ for the (dimensionless) charge magnitude per head monomer.

The Flory and square gradient interaction parameters are chosen so that the model captures realistic features of a lipid membrane. Setting $\chi_{HT} = 75$, $\chi_{TS} = 25$, $\chi_{SH} = 0$ and $\kappa_H = \kappa_T = 2, \kappa_S = 0$, we obtain, in the tensionless state, an area per lipid of 0.74 nm^2 and a membrane width of ~ 3.5 nm;

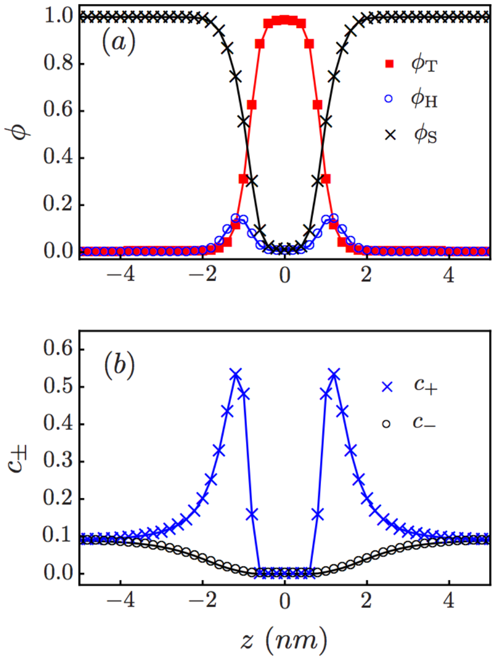

Figure 2.2: (a) Volume fractions and (b) ion number concentrations (nm^{-3}) across the axis perpendicular to the membrane

see Fig. 2.2(a). Both values are similar to those obtained from experiments and molecular dynamic simulations [32]. We choose $\epsilon_T = 2$ and $\epsilon_H = 50$ for the dielectric constants of the tail and head regions [33], respectively, and for the solvent we use $\epsilon_S = 80$. Figure 2.2(b) shows an accumulation of cations in the head region due to the negatively charged head monomers, and a depletion of ions in the tail region due to the low value of the dielectric constant, ϵ_T.

The above parameters are chosen based on experimental results for membranes in the tensionless state. The tension is defined by $\gamma = \partial \mathcal{F}/\partial A|_{n_l}$, where $\mathcal{F}$ is the appropriate free energy and A is the area. To study the limit of stability for a membrane under increasing tensions, we work in a semi-open system (open with respect to solvent and small ions but closed with respect to the number of lipids so that the number of lipids in the membrane is fixed) and obtain the free energy per unit area f as a function of the area per lipid σ. The tension is then evaluated according to

$$\gamma = f + \sigma \left. \frac{\partial f}{\partial \sigma} \right|_{n_l} . \tag{2.19}$$

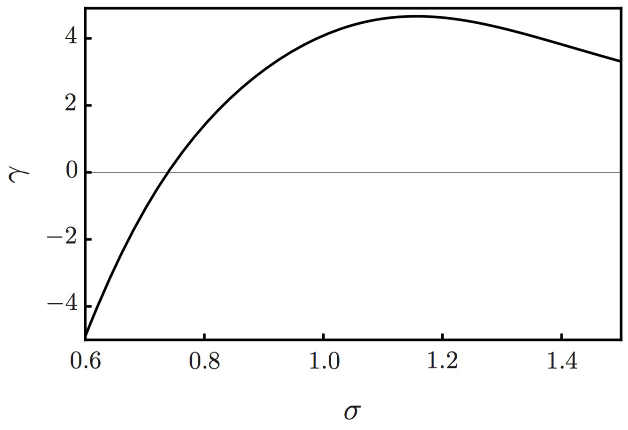

Figure 2.3: Membrane tension ($k_{\mathrm{B}}T/\mathrm{nm}^2$) as a function of the area per lipid (nm^2). The limit of metastability occurs where $\partial\gamma/\partial\sigma = 0$.

For a mechanically stable membrane, $(\partial\gamma/\partial\sigma) > 0$. Therefore, the condition $(\partial\gamma/\partial\sigma) = 0$ signals the onset of mechanical instability, which we identify with the point of rupture and term the value of tension at this point the critical tension. In Fig. 2.3, the rupture corresponds to the maximum of the tension-area curve, with a critical value of the areal expansion of ~ 0.45, and critical tension $\gamma_c \sim 4.5$ $\mathrm{k_BT/nm^2}$. The same calculation is repeated in the grand canonical ensemble, which is open to all species. In this system, the excess grand potential (given by Eq. (2.10) relative to the uniform bulk solution) per unit area directly gives the tension up to the rupture value. The results from these two ensembles are identical. For convenience, particularly when a dendrimer is present, in what follows we work in the grand canonical ensemble.

We note that the rupture captured by this one-dimensional calculation is the limit of metastability for a uniform static membrane. In reality, thermal fluctuations and lipid rearrangements are responsible for regions of membrane thinning [34, 35] that lead to rupture under much lower tensions. Therefore, it is not surprising that our value for the critical tension is higher than the values determined from micropipette aspiration experiments ($0.75 - 2.5$ $\mathrm{k_BT/nm^2}$, depending on degree of saturation of the lipid tails [36]), and the areal expansion we obtain is an order of magnitude greater than the areal expansion obtained experimentally for lipid vesicles [37] (but comparable to the results for polymersome mebranes [38]). We emphasize that these results do not suggest that our model is unphysical, but rather that the experimentally observed rupture is likely a nucleated event. In what follows, we explore the thermodynamics of membrane-particle interactions.

2.3.2 Thermodynamics of Membrane-Particle Interactions

Properties of the fixed particle are chosen to capture the size and charge of different generations of PAMAM dendrimers [39]. Because the outer surface of a high-generation dendrimer is highly congested and unlikely to be penetrated by lipids (see Zhang [6] and references within), we define a radius R_F, which excludes any lipids from within the volume of the particle. The total charge of the particle is given by the number of terminal amine groups, which are essentially all protonanted at neutral pH [40]. Due to significant backfolding of these amines [41], the charge can be assumed to be distributed evenly in the volume of the particle (see Fig. 2.7 for the dendrimer sizes and charge densities used in this work).

We find the results insensitive to the dielectric constant chosen for the particle, and assign $\epsilon_F = \epsilon_S = 80$. Because the system is axially symmetric, we work in cylindrical coordinates, with the center of the particle defined as $\mathbf{r}_F = (r_F, z_F) = (0, z_F)$ and the membrane positioned at $z = 0$. The vertical position of the particle z_F then becomes a natural reaction coordinate for the system. In what follows, we constrain the position of the particle and numerically solve the set of SCF equations at each position. The solutions to the uniform membrane case are used as the boundary condition, holding the membrane at fixed tension and its outer edges at fixed position.

In general, the SCF equations can have multiple solutions, corresponding to different free energy minima, with one being the global minimum and the rest being the metastable minima. Capturing all the free energy minima is a nontrivial task. However, symmetry and simple physical intuition can often be used to limit the search. Here, we take advantage of the different ways of initializing the SCF equations as a means to access the stable and metastable minima. We consider two methods:

1. We begin with a noninteracting membrane-particle system and *slowly* move the particle along the path of decreasing z_F. At each step, the previous solutions are used to initialize the new equations.

2. We instantaneously place the particle at z_F, sometimes initializing the configurations with a

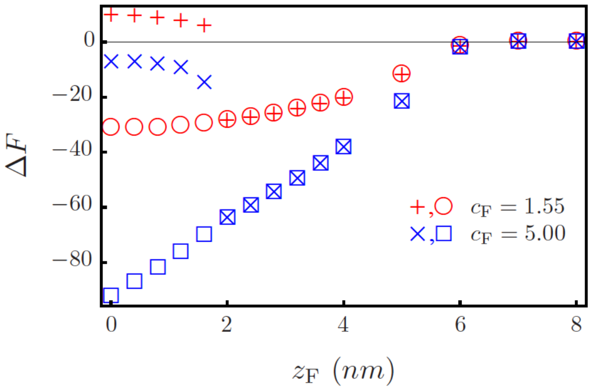

Figure 2.4: Free energy profile ($k_{\mathrm{B}}T$) for the tensionless membrane. ΔF is relative to a noninteracting membrane-particle system, where $z_F \rightarrow \infty$. The particle is a G5 dendrimer with radius $R_F = 2.7$ nm and charge density $c_F = 1.55$ nm^{-3} (all 128 surface amines are protonated). For comparison, we have also plotted the results for a hypothetical G5 dendrimer with $c_F = 5.00$ nm^{-3}. Empty symbols correspond to method 1; + and × correspond to method 2 (see text for description).

hole in the membrane. This hole can be interpreted as a temporary defect caused by fluctuations.

2.3.2.1 Tensionless Membrane

We first apply method 1 to a tensionless membrane and a fully protonated G5 dendrimer. While the specific interactions are local, the electrostatic interactions are long-ranged and rearrangements of the lipid molecules allow the membrane to reach out and meet the particle, as shown in Fig. 2.5(a). At this point, the particle is within the attractive range of the membrane. This is depicted in Fig. 2.4, where the potential well in the free energy profile is due to a competition between satisfying the favorable electrostatic interactions and deforming the membrane. From the free energy profile, we see that the particle will continue towards $z_F \sim 0$ nm, corresponding to a metastable, partially wrapped state.

Interestingly, if we imagine an external force which continues to *slowly* push the particle, we find that the membrane does not rupture. Instead, it deforms until the two sides of the membrane trailing the leading edge of the particle fuse together, and a dendrimer-filled vesicle naturally pinches off from the membrane. Although beyond the scope of this article, further analysis of this process

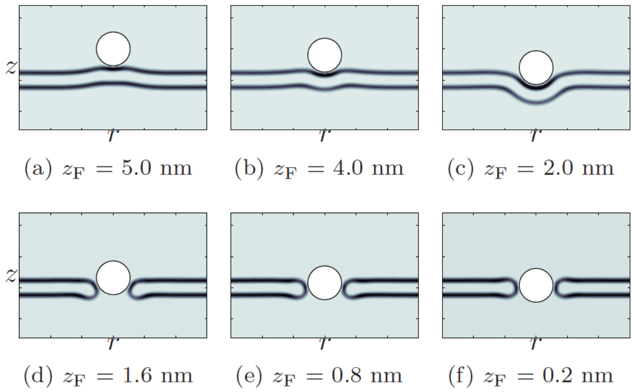

(a) z_F = 5.0 nm (b) z_F = 4.0 nm (c) z_F = 2.0 nm

(d) z_F = 1.6 nm (e) z_F = 0.8 nm (f) z_F = 0.2 nm

Figure 2.5: ϕ_H in cylindrical coordinates for a tensionless membrane and a fully protonated G5 dendrimer with $c_F = 1.55$ nm^{-3}. (a–c) are solutions to both methods 1 and 2, while (d–f) are only solutions to the latter.

of pushing the particle through the membrane could provide information as to the energetics and forces required by the cell (in particular, the proteins recruited) to enforce shape transitions of the membrane involved in endocytosis.

We next solve the same SCF equations by method 2. Depending on the extent of the hole created by the particle and the parameters of the system (membrane tension, dendrimer charge and dendrimer size), the system will fall into one of two solutions: either the membrane reseals the hole and partially wraps the particle, or the membrane forms a head-lined pore around the particle. This is observed from the density plots (Fig. 2.5) and from the free energy profile (Fig. 2.4), where the SCF solutions correspond to a partially wrapped particle until $z_F \sim 2.0$ nm. Beyond this, if thermal fluctuations initiate a hole (as simulated by method 2), then the system will find the solutions to the higher energy path corresponding to a membrane pore. However, the particle must squeeze its way into the pore, as can be seen in Fig. 2.5(d) and the free energy increases with decreasing z_F. This indicates that any pore induced into a tensionless membrane is highly unstable and will be short-lived. In all of our calculations, it is important to remember that the particle position is fixed. In other words, we have constrained the SCF equations so that the membrane is forced to respond to a particle at fixed z_F. If we lift this constraint, the membrane will expel the particle and reseal the pore. The system will then find the metastable state corresponding to the partially wrapped particle.

From the above analysis for a fully protonated G5 dendrimer interacting with a tensionless membrane, it is clear that the pore state cannot exist without constraining the position of the particle. It is of interest to know whether the pore state can be stabilized by appropriately modifying the dendrimer. If the increase in free energy is due to the particle having to squeeze its way through the pore as it deforms the membrane, increasing the particle size is not the solution. Instead, suppose that we can increase the charge density on the dendrimer by chemically modifying the functional groups.

In Fig. 2.4 we compare the result for a hypothetical, highly charged G5 dendrimer ($c_F = 5.00$ nm^{-3}) to the result for a fully protonated G5 dendrimer ($c_F = 1.55$ nm^{-3}). Due to screening by the salt ions, increasing the charge density does not increase the range of electrostatic attraction. It increases the extent and stability of the wrapped state. If the system manages to reach the unstable pore state, it will be short-lived, according to the same explanation given in the preceding paragraph for $c_F = 1.55$ nm^{-3}. From method 1, we find that electrostatic interactions alone are insufficient for a dendrimer to induce holes in a tensionless membrane. From method 2, even if thermal fluctuations assist by initiating temporary holes, we find that the dendrimer is unable to stabilize pores in a tensionless membrane.

2.3.2.2 Membrane Under Tension

In the proton sponge hypothesis, an increase in osmotic pressure is believed to rupture the endosome. We account for the osmotic pressure by applying a tension to the membrane, and explore the combined effects of the applied tension and the electrostatic interactions between the membrane and the particle. In Fig. 2.6, we continue with a fully protonated G5 dendrimer and plot the free energy profile for $\gamma = 0.74$ k$_\mathrm{B}$T/nm^2. The cost of deforming a membrane under tension has shifted the metastable state from partially wrapped ($z_F \sim 0$ nm) to surface-absorbed ($z_F \sim 2.8$ nm). The membrane is also less successful at healing defects (e.g., those initialized by method 2) and transitions earlier to the pore state, which now corresponds to a *second* metastable state. It is also known that

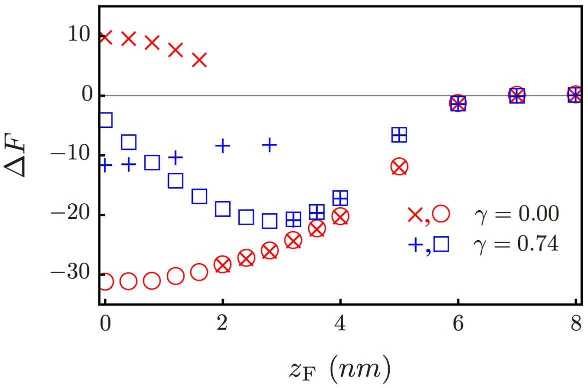

Figure 2.6: Free energy profile ($k_B T$) for a membrane with $\gamma = 0.74$ $k_B T/\mathrm{nm}^2$, shown together with the tensionless membrane from Fig. 2.4. The particle is once again a fully protonated G5 dendrimer. Empty symbols correspond to method 1; $+$ and $\times$ correspond to method 2 (see text for description). Note that we are well below the limit of metastability for a homogeneous membrane, where rupture occurs at $\gamma_c \sim 4.5$ $k_B T/\mathrm{nm}^2$.

membrane permeability and hole formation are dependent on dendrimer generation and terminal functional groups [6–9]. Therefore, we also consider G3–G7 dendrimers. Our results agree with experimental trends, where we find that G3 dendrimers do not stabilize pores, while G5 and G7 dendrimers do, see Fig. 2.7.

However, with respect to the endosomal escape, our interest lies in dendrimers that can nucleate rupture, not stabilize pores. Recall that rupture of a uniform membrane occurs at $\gamma_c \sim 4.5$ $\mathrm{k_B T/nm^2}$. Consider the membrane under tension with an inserted G5 dendrimer ($c_F = 1.55$ nm^{-3}) shown in Fig. 2.6, where the pore state is metastable. If we slowly increase the tension from this state, we find that the limit of metastability occurs at $\gamma_c \sim 0.84$ $\mathrm{k_B T/nm^2}$, see Fig. 2.8. For tensions exceeding this value, the pore radius expands indefinitely and the membrane ruptures. Interestingly, even a highly charged particle, which should have strong adhesion to the head-lined pore periphery, lowers the rupture tension, where γ_c levels off at ~ 1.3 $\mathrm{k_B T/nm^2}$.

We should comment that increasing the charge on dendrimers makes the pore state energetically more favorable as compared to the wrapped state. So even though membranes containing higher-charged dendrimers require higher rupture tensions, the higher-charged dendrimers are more effective at stabilizing the pore state to begin with (see Fig. 2.7), and therefore more effective at facilitating

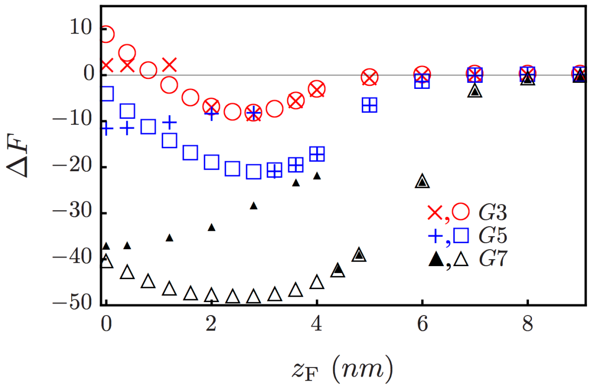

Figure 2.7: Free energy profile ($k_\mathrm{B}T$) for a membrane with $\gamma = 0.74\ k_\mathrm{B}T/\mathrm{nm}^2$ interacting with G3 ($R_F = 1.8$ nm, $c_F = 1.30\ \mathrm{nm}^{-3}$), G5 ($R_F = 2.7$ nm, $c_F = 1.55\ \mathrm{nm}^{-3}$), and G7 ($R_F = 4.0$ nm, $c_F = 2.0\ \mathrm{nm}^{-3}$) dendrimers. Empty symbols correspond to method 1; +, ×, and ▲ correspond to method 2 (see text for description).

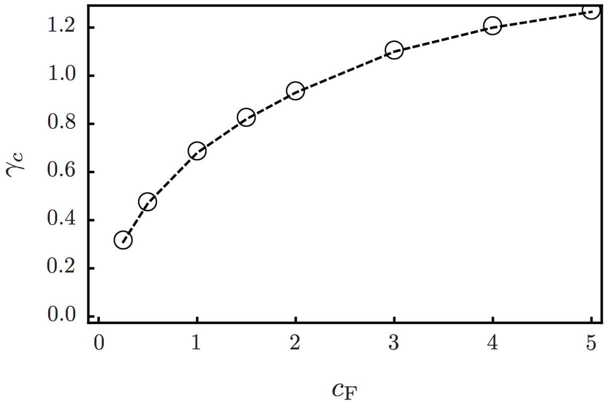

Figure 2.8: Rupture tension ($k_\mathrm{B}T/\mathrm{nm}^2$) for a membrane containing a pore, plotted as a function of the charge density (nm^{-3}) of the G5 dendrimer stabilizing the pore

rupture. The study of the actual nucleation barriers and pathways to pore formation and rupture are beyond the scope of this work. Nevertheless, these results show that highly charged dendrimers can greatly lower the rupture tensions. In terms of the endosomal escape, this dendrimer-induced rupture at significantly lower tensions is precisely what we seek.

2.4 Conclusion

In this work, we have used SCFT to study the thermodynamics of membrane-particle interactions in the context of polymer-based gene delivery systems. We have focused on the endosomal escape mechanism, where our main goal is to understand the role of the dendrimer in nucleating membrane rupture (with the eventual release of the genetic material from the endosome). For different membrane tensions, dendrimer sizes and charge densities, we have explored the structural and energetic properties of the system. In what follows, we summarize our main findings and the implications for designing polymer-based gene delivery vectors.

For tensionless membranes, we find that the hydrophilic pore with an inserted dendrimer is unstable; the tensionless membrane prefers to satisfy the favorable electrostatic interactions by partially wrapping the dendrimer. Our results indicate that increasing the charge density of the dendrimer only increases the extent and stability of the wrapped state, while the pore state, if somehow created, remains unstable and short-lived. In other words, the tensionless membrane is so robust that even a highly charged particle is unable to insert into the membrane and stabilize a pore. This suggests that the osmotic pressure contribution from the proton sponge hypothesis is a necessary component if the endosomal escape is to be enhanced by particle insertion into the membrane.

To study the effect of the osmotic pressure, we apply a tension $\gamma = 0.74\ \mathrm{k_BT/nm^2}$ to the membrane. This value is well below the limit of metastability for a uniform membrane, for which $\gamma_c \sim 4.5\ \mathrm{k_BT/nm^2}$. For G5 dendrimers and higher, we find that the pore corresponds to a metastable state, while for G3 dendrimers the pore is unstable. This agrees with experimental trends on the ability of the dendrimer to cause membrane permeability and hole formation [6–9]. Lee and Larson [13], using MD simulations on similar membrane-particle systems, found that dendrimer-induced membrane disruption was dependent on generation *and* concentration. We believe that the apparent concentration dependence is related to local membrane tensions that are induced by nearby particles due to the fixed membrane area. This is in agreement with the effect of tension in our findings, where metastable pores exist only in combination with an applied tension. Finally, our results indicate that these same metastable pores can act as nucleation sites for rupture.

With respect to overcoming the endosomal escape barrier (one of many to consider in gene delivery systems), we have shown that there are at least two properties to consider in the design of the vector: (1) the dendrimer should be able to induce a tension on the membrane, e.g., by increasing the osmotic pressure through the proton sponge mechanism; and (2) the dendrimer should be sufficiently large and with enough charge so as to stabilize the pore state. Without the combined effect of the two, the membrane would prefer to satisfy the electrostatic interactions by partially wrapping around the dendrimer.

Finally, we comment on the limitations of our present study. In all of our calculations, we have fixed the position of the dendrimer z_F so that the solutions we obtain are subject to this constraint. The free energy profile in this sense yields the potential of mean force between the particle and the membrane. The multiple unstable and metastable states are obtained from the behavior of the free energy as a function of z_F. However, the reaction coordinate for nucleating rupture most likely will not be z_F, but will involve the rearrangement of the lipids in the pre-pore state. The current study does not address how the particle becomes inserted into the membrane from the partially wrapped state, nor does it address the subsequent nucleation event leading to rupture.

To study the pathways associated with these activated processes will require minimum energy path (MFEP) calculations using, e.g., the nudged elastic band [42, 43] or the string method [44]. We note that simpler calculations, where physical insight is used to impose one or more reaction coordinate constraints (in a similar spirit to our particle position z_F) have sometimes been used to study nucleation processes in membrane fusion [27]. However, the structures associated with dendrimer-induced pore formation and membrane rupture are more complicated and it is not obvious that some simple constraints can be identified. In Chapter 3, we apply MFEP calculations to dynamic SCF theory to address the actual nucleation events involved in the dendrimer-induced pore formation and membrane rupture.

The authors gratefully acknowledge support from the Jacobs Institute for Molecular Engineering for Medicine at Caltech. C.L.T. is thankful for financial support from an NIH training grant.

Appendix A: Gradient Expansion

For the second term in Eq. (2.2), we focus on one term in the sum and perform a change of variables $\bar{\mathbf{r}} = \mathbf{r} - \mathbf{r}'$ and expand around $\mathbf{r}'$

$$\begin{gathered}\int d\mathbf{r} d\mathbf{r}' \hat{\phi}_J(\mathbf{r}) u_{JK}(\mathbf{r}-\mathbf{r}') \hat{\phi}_K(\mathbf{r}') = \int d\bar{\mathbf{r}} d\mathbf{r}' \hat{\phi}_J(\bar{\mathbf{r}}+\mathbf{r}') u_{JK}(\bar{\mathbf{r}}) \hat{\phi}_K(\mathbf{r}') \approx \\ \int d\bar{\mathbf{r}} d\mathbf{r}' \left[\hat{\phi}_J(\mathbf{r}') + \bar{\mathbf{r}}^T \nabla \hat{\phi}_J(\mathbf{r}') + \frac{1}{2} \bar{\mathbf{r}}^T \nabla\nabla \hat{\phi}_J(\mathbf{r}') \bar{\mathbf{r}} \right] u_{JK}(\bar{\mathbf{r}}) \hat{\phi}_K(\mathbf{r}').\end{gathered} \tag{A-1}$$

The zeroth-order term in Eq. (A-1) defines the Flory interaction parameter

$$\int d\bar{\mathbf{r}} u_{JK}(\bar{\mathbf{r}}) \int d\mathbf{r}' \hat{\phi}_J(\mathbf{r}') \hat{\phi}_K(\mathbf{r}') \equiv \chi_{JK} \int d\mathbf{r}' \hat{\phi}_J(\mathbf{r}') \hat{\phi}_K(\mathbf{r}'). \tag{A-2}$$

Assuming $u_{JK}(\bar{\mathbf{r}})$ is symmetric, the first-order term vanishes; performing an integration by parts, the second-order term defines the phenomenological square gradient parameter κ_{JK}

$$-\frac{1}{2} \int d\bar{\mathbf{r}}\, \bar{\mathbf{r}}^T \bar{\mathbf{r}} u_{JK}(\bar{\mathbf{r}}) \int d\mathbf{r}' \nabla \hat{\phi}_J(\mathbf{r}')^T \nabla \hat{\phi}_K(\mathbf{r}') \equiv \frac{\kappa_{JK}}{2} \int d\mathbf{r}' \nabla \hat{\phi}_J(\mathbf{r}')^T \nabla \hat{\phi}_K(\mathbf{r}'). \tag{A-3}$$

Neglecting the cross square gradient terms and defining $\kappa_{JJ} \equiv \kappa_J$ gives the following approximation to Eq. (2.2):

$$\mathcal{H} \approx \sum_{i=1}^{n_L} h_i + \int d\mathbf{r} d\mathbf{r}' \left\{ \sum_{JK} \left[\hat{\phi}_J(\mathbf{r}) \chi_{JK} \hat{\phi}_K(\mathbf{r}) + \frac{\kappa_J}{2} |\nabla \hat{\phi}_J(\mathbf{r})|^2 \right] + \frac{e^2}{2} \hat{\rho}_c(\mathbf{r}) C(\mathbf{r},\mathbf{r}') \hat{\rho}_c(\mathbf{r}') \right\}. \tag{A-4}$$

Appendix B: From a Particle-Based to a Field-Theoretic Model

We will make use of the following two identities:

1. The Hubbard-Stratanovich transformation:

$$\exp\left[-\frac{1}{2}\int dx \int dx' J(x)A(x,x')J(x')\right] = \frac{\int \mathcal{D}f \exp\left[-\frac{1}{2}\int dx \int dx' f(x)A^{-1}(x,x')f(x') + i\int dx J(x)f(x)\right]}{\int \mathcal{D}f \exp\left[-\frac{1}{2}\int dx \int dx' f(x)A^{-1}(x,x')f(x')\right]} \tag{B-1}$$

   where J is the instantaneous density, A is the operator and f is the auxiliary field.

2. Alternatively, one can introduce the field variables ϕ_I through a series of formal functional analysis identities for the Dirac distribution. First the instantaneous densities (expressed as a unitless volume fractions) are converted into smooth scalar density fields $\hat{\phi}_I = \phi_I$:

$$\int \mathcal{D}\phi_I \delta\Big[\phi_I(\mathbf{r}) - \hat{\phi}_I(\mathbf{r})\Big] F[\phi_I(\mathbf{r})] = F[\hat{\phi}_I(\mathbf{r})]. \tag{B-2}$$

   Then the associated (conjugated) fields ξ_I are introduces via the formal Fourier representation of $\delta[f(\mathbf{r}) - g(\mathbf{r})]$:

$$\delta\Big[f(\mathbf{r}) - g(\mathbf{r})\Big] = \int \mathcal{D}\xi_I \exp\left\{i\int d\mathbf{r}\xi_I(\mathbf{r})\Big[f(\mathbf{r}) - g(\mathbf{r})\Big]\right\}. \tag{B-3}$$

   These two steps also decouple the interactions among particles and replace them with interactions between single particles and effective fields.

Using these two identities, we can now write the partition function in Eq. (2.8) as

$$\begin{aligned}
\Xi = &\sum_{n_{\{L,S,\pm\}}=0}^{\infty} \frac{\mathrm{e}^{(\mu_L n_L + \mu_S n_S + \mu_\pm n_\pm)}}{n_L! n_S! n_\pm! {v_L}^{n_L} {v_S}^{n_S} {v_\pm}^{n_\pm}} \int \prod_{i=0}^{n_L} \mathcal{D}\mathbf{r}_i \int \prod_{j=0}^{n_S} d\mathbf{r}_j \int \prod_{k=0}^{n_\pm} d\mathbf{r}_k \\
&\int \mathcal{D}\phi_I \int \mathcal{D}\xi_I \exp\left\{ i \int d\mathbf{r} \xi_I(\mathbf{r}) [\phi_I(\mathbf{r}) - \hat{\phi}_I(\mathbf{r})] \right\} \\
&\times \exp\left\{ -\sum_{i=1}^{n_L} h_i - \int d\mathbf{r} \left(\sum_{JK} \left[\phi_J(\mathbf{r}) \chi_{JK} \phi_K(\mathbf{r}) + \frac{\kappa_J}{2} |\nabla \phi_J(\mathbf{r})|^2 \right] + \frac{z_\pm^2 e^2 \hat{c_\pm}(\mathbf{r})}{8\pi a_\pm \epsilon(\mathbf{r})} \right) \right\} \\
&\times \int \mathcal{D}\psi \, \exp\left\{ i \int d\mathbf{r} \psi(\mathbf{r}) \left[c_F \phi_F(\mathbf{r}) - \frac{c_H}{v_H} \phi_H(\mathbf{r}) \pm z_\pm e \hat{c}_\pm(\mathbf{r}) \right] - \int d\mathbf{r} \frac{\epsilon(\mathbf{r})}{2} (\nabla \psi(\mathbf{r}))^2 \right\}.
\end{aligned} \tag{B-4}$$

Where we have used Eq. (B-1), together with Eq. (2.6), to decouple the quadratic terms in the Coulomb energy. Note, also, that incompressibility condition is imposed directly by defining $\phi_S = 1 - \phi_H - \phi_T - \phi_F$. Separating the terms containing the microscopic densities from those containing the fields, we write

$$\begin{aligned}
\Xi = &\int \mathcal{D}\phi_I \int \mathcal{D}\xi_I \int \mathcal{D}\psi \\
&\times \sum_{n_L=0}^{\infty} \frac{e^{\mu_L n_L}}{{v_L}^{n_L} n_L!} \int \prod_{i=0}^{n_L} \mathcal{D}\mathbf{r}_i \exp\left\{ -\sum_{i=1}^{n_L} h_i - \int d\mathbf{r} \xi_{H,T} \hat{\phi}_{H,T} \right\} \\
&\times \sum_{n_S=0}^{\infty} \frac{e^{\mu_S n_S}}{v_S^{n_S} n_S!} \int \prod_{j=0}^{n_S} d\mathbf{r}_j \exp\left\{ -\int d\mathbf{r} \xi_S \hat{\phi}_S \right\} \\
&\times \sum_{n_\pm=0}^{\infty} \frac{e^{\mu_\pm n_\pm}}{v_\pm^{n_\pm} n_\pm!} \int \prod_{k=0}^{n_\pm} d\mathbf{r}_k \exp\left\{ -\int d\mathbf{r} e z_+ \psi \, \hat{c}_\pm - \int d\mathbf{r} \frac{z_\pm^2 e^2 \hat{c_\pm}}{8\pi a_\pm \epsilon} \right\} \\
&\times \exp\left\{ -\int d\mathbf{r} \psi \left(c_F \phi_F - \frac{c_H}{v_H} \phi_H \right) - \frac{\epsilon}{2} (\nabla \psi)^2 \right\} \\
&\times \exp\left\{ -\int d\mathbf{r} \sum_{JK} \left(\chi_{JK} \phi_J \phi_K - \xi_J \phi_J - \frac{\kappa_J}{2} [\nabla \phi_J]^2 \right) \right\}.
\end{aligned} \tag{B-5}$$

In anticipation of the imaginary nature for the field variables ξ_I and ψ at the saddle point, we have redefined the real field $i\xi_I \to \xi_I$ and $-i\psi \to \psi$. Noting that the molecules within each species are indistinguishable and making use of the microscopic density operators, this can be rewritten:

$$\begin{aligned}\Xi = &\int \mathcal{D}\phi_I \int \mathcal{D}\xi_I \int \mathcal{D}\psi \\ &\times \exp\left\{ \frac{e^{\mu_L}}{v_L} \int \mathcal{D}\mathbf{r} e^{-h - v_{H,T}\xi_{H,T}} + \frac{e^{\mu_S}}{v_S} \int d\mathbf{r} e^{-v_s \xi_s} + \frac{e^{\mu_\pm}}{v_\pm} \int d\mathbf{r} e^{\mp e z_\pm \psi - u^b_\pm} \right\} \\ &\times \exp\left\{ -\int d\mathbf{r} \psi \left(c_F \phi_F - \frac{c_H}{v_H}\phi_H \right) - \frac{\epsilon}{2} (\nabla\psi)^2 \right\} \\ &\times \exp\left\{ -\int d\mathbf{r} \sum_{JK} \left(\chi_{JK}\phi_J\phi_K - \xi_J\phi_J - \frac{\kappa_J}{2}[\nabla\phi_J]^2 \right) \right\}. \end{aligned} \tag{B-6}$$

Fitting this expression into Eq. (2.9), it is evident that the field theoretic partition function is given by Eq. (2.10) with the single molecule partition functions given by Eq. (2.11). For the lipids, the Boltzmann factor contains the term h for the chain connectivity. This is further weighted by the external fields ξ_H and ξ_T. To obtain the single chain statistics for the lipids, our approach will be to compute the chain propagators q_H and q_T, as described in Appendix C. Finally, we comment that the Boltzmann factor for the ions contains the Born-self energy $u^b_\pm$ in a spatially varying dielectric medium [15].

Appendix C: Propagator for a Single Chain in External Fields

We introduce the chain propagator by analogy to a Markovian process, where the monomer index i can be thought of as the analogue of a discrete time variable in a stochastic process. In this way we seek to build up the configuration of the graft copolymer, from the free end of each arm to the branch point, beginning with the initial condition that

$$q_I(\mathbf{r},1)=\mathrm{e}^{-v_I\xi_I(\mathbf{r})} \tag{C-1}$$

for $I=H,T$. Moving to subsequent monomers i corresponds to propagating forward in the "time" index:

$$q_I(\mathbf{r};i)=\mathrm{e}^{-v_I\xi_I(\mathbf{r})}\int d\mathbf{r}'\Gamma(|\mathbf{r}-\mathbf{r}'|)q_I(\mathbf{r}';i-1). \tag{C-2}$$

Here $i\in(2,N_I)$ and Γ denotes the transition probability from one monomer to the next, assumed to be Gaussian. For notational simplicity, in what follows we drop the subscript I and denote $q(\mathbf{r},i)$ as simply $q^i(\mathbf{r})$. The above expression is essentially a reduced partition function for a chain beginning at $\mathbf{r}$ and ending anywhere. Rather than attempt to evaluate Eq. (C-2) directly by an integration scheme, we recognize that for a reasonably smooth external potential, the contributions are dominated by the transitions for which $|\mathbf{r}-\mathbf{r}'|$ is on the order of the range of (or less than) the Gaussian. Thus, following the usual practice in deriving a differential equation from the Chapman-Kolmogoroff equation, we expand $\mathbf{r}'$ around $\mathbf{r}$ to quadratic order. Further representing the spatial derivatives by differences in cylindrical coordinates for our axially-symmetric membrane-particle system, we get

$$\begin{aligned} q^{i+1}(r_j,z_k)=\mathrm{e}^{-v\xi(r_j,z_k)}\Big\{&\big[1-4\gamma\big]q^i(r_j,z_k)+\gamma q^i(r_j,z_{k+1})+\gamma q^i(r_j,z_{k-1})\\ &+\gamma(1+\frac{1}{2j})q^i(r_{j+1},z_k)+\gamma(1-\frac{1}{2j})q^i(r_{j-1},z_k)\Big\}. \end{aligned} \tag{C-3}$$

Here we have defined $\gamma = b^2/6h^2$, where b^2 is the variance of the transition probability and and h is the grid spacing, and we have discretized space by a uniform grid:

$$(r_j, z_k) = (jh, kh), \quad j = 0, ..., n_{\mathrm{r}}, \quad k = -n_{\mathrm{z}}, ..., n_{\mathrm{z}}. \tag{C-4}$$

From Eq. (C-3), we can identify the following transition probabilities on the discretized lattice:

$$\begin{aligned}
\Gamma(r_j, z_{k+1} \to r_j, z_k) &= \gamma, \\
\Gamma(r_j, z_{k-1} \to r_j, z_k) &= \gamma, \\
\Gamma(r_{j+1}, z_k \to r_j, z_k) &= \gamma(1 + \frac{1}{2j}), \\
\Gamma(r_{j-1}, z_k \to r_j, z_k) &= \gamma(1 - \frac{1}{2j}), \\
\Gamma(r_j, z_k \to r_j, z_k) &= 1 - 4\gamma,
\end{aligned} \tag{C-5}$$

where the last expression can be thought of as the "survival probability". Eq. (C-3) applies to $j \neq 0$. For $j = 0$, we have

$$q^{i+1}(r_0, z_k) = \mathrm{e}^{-v\xi(r_0,z_k)} \Big\{ \big[1 - 6\gamma\big] q^i(r_0, z_k) + \gamma q^i(r_0, z_{k+1}) + \gamma q^i(r_0, z_{k-1}) + 4\gamma q^i(r_1, z_k) \Big\}, \tag{C-6}$$

from which we similarly obtain the transition probabilities. Note that the positivity of the transition probabilities requires that $\gamma < 1/6$. Continuing with the analogy to a Markovian process, we can define an equivalent "master equation" for the chain propagator on our discrete grid, and Eq. (C-2) becomes

$$q^i(r_j, z_k) = \mathrm{e}^{-v\xi(r_j,z_k)} \sum_{r'_j, z'_k} \Gamma(r'_j, z'_k \to r_j, z_k) q^{i-1}(r'_j, z'_k), \tag{C-7}$$

where it is understood that the summation is restricted to the nearest neighbors of (r_j, z_k). The discretization scheme we have used assumes that the range of a bond joining two monomers is on the order of (or less than) the grid spacing h. More precisely $b < \sqrt{3/2}h$. For cases where we wish to lengthen the range of the bonds, we can include next-nearest neighbor transitions (and beyond) by inserting fictitious monomers at intermediate positions. These intermediate beads satisfy Eq. (C-3) and Eq. (C-6), but without the Boltzmann weight associated with the external field. Finally, we comment that the discrete Gaussian chain given here, unlike the continuous Gaussian chain model, has finite range of bond lengths, which are specified by the grid spacing h and the number of intermediate beads.

Bibliography

[1] C. L. Ting and Z.-G. Wang, *Biophys. J.* **100**, 1288 (2011).

[2] D. W. Pack, A. S. Hoffman, S. Pun, and P. S. Stayton, *Nat. Rev. Drug Discov.* **4**, 581 (2005).

[3] J. Haensler and F. C. Szoka, *Bioconjugate Chem.* **4**, 372 (1993).

[4] J. P. Behr, *Chimia.* **51**, 34 (1997).

[5] N. D. Sonawane, F. C. Szoka, and A. S. Verkman, *J. Biol. Chem.* **278**, 44826 (2003).

[6] Z.-Y. Zhang and B. D. Smith, *Bioconjugate Chem.* **11**, 805 (2000).

[7] S. Hong, A. U. Bielinska, A. Mecke, B. Keszler, J. L. Beals, X. Shi, L. Balogh, B. G. Orr, J. R. Baker, and M. M. Banaszak Holl, *Bioconjugate Chem.* **15**, 774 (2004).

[8] A. Mecke, I. J. Majoros, A. K. Patri, J. R. Baker, M. M. Banaszak Holl, and B. G. Orr, *Langmuir* **21**, 10348 (2005).

[9] J. Chen, J. A. Hessler, K. Putchakayala, B. K. Panama, D. P. Khan, S. Hong, D. G. Mullen, S. C. DiMaggio, A. Som, G. N. Tew, A. N. Lopatin, J. R. Baker, M. M. Banaszak Holl and B. G. Orr, *J. Phys. Chem. B* **113**, 11179 (2009).

[10] S. Boeckle, K. von Gersdorff, S. van der Piepen, C. Culmsee, E. Wagner, and M. Orgis, *J. Gene. Med.* **6**, 1102 (2004).

[11] Y. Yue, F. Jin, R. Deng, J. Cai, Y. Chen, M. Lin, H.-F. Kung, and C. Wu, *J. Control. Release* **155**, 67 (2011).

[12] H. Lee and R. G. Larson, *Molecules* **14**, 423 (2009).

[13] H. Lee and R. G. Larson, *J. Phys. Chem. B* **112**, 12279 (2008).

[14] G. H. Fredrickson, *The Equilibrium Theory of Inhomogeneous Polymers* (Oxford University Press, New York, 2005).

[15] Z.-G. Wang, *Phys. Rev. E* **81**, 021501 (2010).

[16] Q. Zhang and Y. Ma, *J. Chem. Phys.* **125**, 164710 (2006).

[17] V. V. Ginzburg and S. Balijepalli, *Nano Lett.* **7**, 3716 (2007).

[18] A. Ben-Shaul, I. Szleifer, and W. M. Gelbart, *Proc. Natl. Acad. Sci. USA* **81**, 4601 (1984).

[19] I. Szleifer and A. Ben-Shaul, *J. Chem. Phys.* **83**, 3597 (1985).

[20] I. Szleifer, A. Ben-Shaul, and W. M. Gelbart, *J. Chem. Phys.* **83**, 3612 (1985).

[21] T. Zemb and C. Chachaty, *Chem. Phys. Lett.* **88**, 68 (1982).

[22] J. Charvolin, *J. Chim. Phys. Phys. Chim. Biol.* **80**, 15 (1983).

[23] B. Lindman, "Physics of Amphiphiles: Micelles, Vesicles and Microemulsions," *Proceedings of the International School of Physics "Enrico Fermi"* (North-Holland, 2005).

[24] P. van der Ploeg and H. Berendsen, *J. Chem. Phys.* **76**, 3271 (1982).

[25] P. van der Ploeg and H. Berendsen, *Mol. Phys.* **49**, 233 (1983).

[26] O. Edholm, H. Berendsen, and P. van der Ploeg, *Mol. Phys.* **48**, 379 (1983).

[27] K. Katsov, M. Müller, and M. Schick, *Biophys. J.* **87**, 3277 (2004).

[28] K. Hong and J. Noolandi, *Macromolecules* **13**, 964 (1980).

[29] M. W. Matsen and R. B. Thompson, *Macromolecules* **41**, 1853 (2008).

[30] J. F. Nagle and M. C. Wiener, *Biochem. Biophys. Acta* **942**, 1 (1988).

[31] T. K. Rostovtseva, V. M. Aguilella, I. Vodyanoy, S. M. Bezrukov, and V. A. Parsegian, *Biophys. J.* **75**, 1783 (1998).

[32] D. P. Tieleman and H. J. C. Berendsen, *J. Chem. Phys.* **105**, 4871 (1996).

[33] H. Brockman, *Chem. Phys. Lipids* **73**, 57 (1994).

[34] M. A. Wilson and A. Pohorille, *J. Am. Chem. Soc.* **116**, 1490 (1994).

[35] E. Lindahl and O. Edholm, *Biophys. J.* **79**, 426 (2000).

[36] K. Olbrich, W. Rawicz, D. Needham, and E. Evans, *Biophys. J.* **79**, 321 (2000).

[37] E. A. Evans, R. Waugh, and L. Melnik, *Biophys. J.* **16**, 585 (1976).

[38] B. M. Discher, Y. Y. Won, D. S. Ege, J. C. M. Lee, F. S. Bates, D. E. Discher, and D. A. Hammer, *Science* **284**, 1143 (1999).

[39] P. K. Maiti, T. Cagin, G. F. Wang, and W. A. Goddard, *Macromolecules* **37**, 6236 (2004).

[40] M. F. Ottaviani, F. Montalti, M. Romanelli, N. J. Turro, and D. A. Tomalia, *J. Phys. Chem.* **100**, 11033 (1996).

[41] P. K. Maiti and W. A. Goddard, *J. Phys. Chem. B* **110**, 25628 (2006).

[42] G. Henkelman, B. P. Uberuaga, and H. Jonsson, *J. Chem. Phys.* **113**, 9901 (2000).

[43] G. Henkelman and H. Jonsson, *J. Chem. Phys.* **113**, 9978 (2000).

[44] W. N. E, W.Q. Ren, and E. Vanden-Eijnden, *Phys. Rev. B* **66**, 052301 (2002).

Chapter 3

The Minimum Free Energy Path to Membrane Pore Formation and Rupture

We combine dynamic self-consistent field theory with the string method to calculate the minimum energy path to membrane pore formation and rupture. In the regime where nucleation can occur on experimentally relevant time scales, the structure of the critical nucleus is between a solvophilic stalk and a locally thinned membrane. Classical nucleation theory fails to capture these molecular details and significantly overestimates the free energy barrier. Our results suggest that thermally nucleated rupture may be an important factor for the low rupture strains observed in lipid membranes [1].

3.1 Introduction

Membrane bilayers define boundaries for cells and are directly involved in many cellular functions [2]. Understanding the natural processes of the cell therefore requires understanding the physical and mechanical properties of its membranes. The fusion of membranes and the controlled transport of materials across cells involve the formation of transient membrane pores, while the resistance against cell lysis (rupture) is determined by the stability of the membrane against the formation of pores, e.g., during osmotic swelling. In addition to these natural processes, pores can be formed by antimicrobial peptides [3] or electroporation [4]. The latter is a common method for introducing foreign material, such as drugs or genes, to the cell [5].

Several experimental methods have been developed to study pore formation under an applied tension [6–8]. A variety of computational methods have also been used to study the energetic and structural properties of membrane pores [9–15]. Conventional molecular dynamics simulations often require very high tensions, where pore formation is no longer a rare event. On the other hand, the potential of mean constraint force method can be applied to study pore formation as an *activated* process [13–15]. The method requires *artificially* selecting a reaction coordinate constraint that, in general, may not coincide with the true transition pathway involving local lipid rearrangements. Furthermore, computer simulations are limited by the number of amphiphiles and are usually performed under constant area. A pore opening under such conditions simultaneously relaxes the surface tension and can either expand, reseal, or stabilize, depending in a nontrivial manner on the system size [15]. In solvent-free models consisting of two- or three-bead "lipids", there is disagreement between density functional predictions [10] and Monte Carlo simulations [12] with regard to the existence of small metastable pores. The interpretation of structures comparable to the lipid molecular size is highly problematic for these overly simplified models.

3.2 Model and Method

In this chapter, we study the full *minimum free energy path* (MFEP) to pore formation and rupture by combining the string method [16] with dynamic self-consistent field (DSCF) theory [17]. As opposed to calculations that require physical insight to impose one or more constraints on the system [18], the string method automatically determines the reaction coordinate of the MFEP connecting two stable states on a given free energy landscape, while DSCF theory provides a full description (at the mean-field level) of the lipid conformation changes. We begin with an arbitrary set of states between two free energy minima. The states are connected on the free energy landscape by a string and relax towards the MFEP by an iterative procedure. First, all states are evolved independently for some time Δt according to

$$\frac{\partial \phi_I}{\partial t} = -D \frac{\delta F}{\delta \phi_I}, \tag{3.1}$$

where ϕ_I is the monomer volume fraction, D is the mobility coefficient, and F is the free energy functional of the system. Note that for a system not at equilibrium, the gradient cannot be computed using the usual SCF theory. Instead, we solve for a hypothetical external potential $V(\mathbf{r})$, which makes the *given* nonequilibrium density $\phi_I(\mathbf{r})$ an "equilibrium" one; see [19] for details. Briefly, $V(\mathbf{r})$ must satisfy

$$\phi_I(\mathbf{r}) = e^{\mu_I} \sum_{i=1}^{N} q_I(\mathbf{r}, i) e^{V(\mathbf{r})} q_I^*(\mathbf{r}, N - i), \tag{3.2}$$

where the chain propagator $q_I(\mathbf{r}, i)$ is again obtained using the discrete version of Eq. (C-2), i.e., Eq. (C-7). The equation of motion then becomes

$$\frac{\partial \phi_I}{\partial t} = -D \left[\xi_I(\mathbf{r}) - V_I(\mathbf{r}) \right], \tag{3.3}$$

where ξ_I is the usual field obtained by taking the variation of the free energy functional, i.e., $\frac{\delta F}{\delta \phi_I}$.

Then, to prevent the states from falling into one of the two end states (the trivial equilibrium solutions), we make use of the connectivity imposed by the string. Precisely, we compute the total arc length l of the string according to its Euclidian distance:

$$l = \sum_{i=1}^{N_{states}-1} ||\phi_{i+1} - \phi_i||, \tag{3.4}$$

and interpolate the new states so that they are equidistantly spaced along the string:

$$s = l/(N_{states} - 1). \tag{3.5}$$

The procedure is repeated until the dynamics balance the reparameterization, i.e., the evolution of the string has reached a steady state. At this point the string coincides with the MFEP [16] and the free energy and density profiles of all states along the MFEP are immediately known without additional calculations. We note that a similar strategy was recently employed to study the nucleation of order-order transitions in diblock copolymer melts [20].

A starting point for discussing pore formation and rupture is often based on classical nucleation

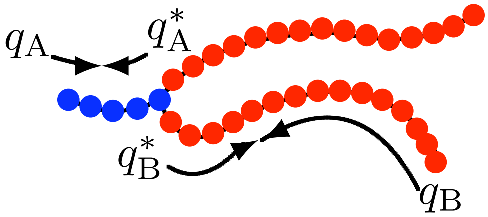

Figure 3.1: An amphiphile consisting of a solvophilic (A) segment of $N_A = 5$ monomers with volume $v_A = 0.05\ \text{nm}^3$ (blue) and two solvophobic (B) segments, each with $N_B = 15$ monomers with volume $v_B = 0.05\ \text{nm}^3$ (red). q_I and q_I^*, where $I = A, B$, are the chain propagator and complementary chain propagator, respectively. Additional parameters include the solvent (S) monomer volume: $v_S = 0.15\ \text{nm}^3$, and interaction parameters: $\chi_{AB}, \chi_{BS}, \chi_{SA} = 75, 18, 0$ and $\kappa_A, \kappa_B, \kappa_S = 0, 8, 0$.

theory (CNT) [21,22]. For a membrane under tension $\gamma > 0$, CNT defines the free energy of a pore of radius r as

$$F = 2\pi r\sigma - \pi r^2\gamma. \tag{3.6}$$

Here $\sigma > 0$ is the line energy. The first term is the cost of forming the rim of a pore and the second term is the relief in elastic energy. The above expression leads to a free energy barrier $F^* = \pi\sigma^2/\gamma$ at a critical radius $r^* = \sigma/\gamma$, beyond which the pore grows indefinitely (ruptures).

For membranes with different tensions γ, we obtain properties of the nucleation pathway, including the structure and activation energy F^* of the critical nucleus. Comparing the values of our calculated F^* with those predicted by CNT, we find that CNT is valid only for small γ, where the free energy barrier is nearly insurmountable on experimentally realistic time scales. For the physically relevant regime, where $F^* \lesssim \mathcal{O}(10\ kT)$, CNT significantly overestimates the barrier height. Furthermore, in this regime the critical nuclei are not well-defined pores, as assumed by CNT, but rather “stalks” of amphiphile head groups or, in the case of large γ, merely a local thinning of the membrane.

Our model consists of a bilayer assembled from double-tailed amphiphiles in explicit solvent. The amphiphiles are modeled as discrete Gaussian chains having a solvophilic block and two solvophobic tails; see Fig. 3.1. The solvents are represented as monomers. The different monomer species are assumed to interact with short-ranged, pairwise potentials, and the hard-core repulsion is accounted for by treating the system as incompressible. We work mostly in the grand canonical ensemble, where the numbers of amphiphile and solvent molecules are controlled by their chemical potentials. kT is used as the energy unit. The particle-based Hamiltonian for the system, accounting for the chain connectivity of the n amphiphiles and the pairwise energetic interactions among species, is

$$\mathcal{H} = \sum_{i=1}^{n} h_i(\{\mathbf{r}\}) + \sum_{\substack{JK \\ \in\{AB,BS,SA\}}} \int d\mathbf{r}d\mathbf{r}' \hat{\phi}_J(\mathbf{r}) u_{JK}(\mathbf{r},\mathbf{r}') \hat{\phi}_K(\mathbf{r}'). \tag{3.7}$$

The particle to field transformation follows the same derivation given in Chapter 2. Briefly, the interactions among particles are decoupled and replaced with interactions between particles and effective fields; see also [23]. The resulting field-theoretic partition function can be generically written $\Xi = \int D\omega \exp(-F[\omega])$, where F is an effective, complex-valued free energy that depends on the field variable ω. Here, we make the mean-field approximation, which amounts to assuming that a single field configuration ω^* dominates the functional integral so that $\Xi \approx \exp(-F[\omega^*])$. In our model $F[\omega^*]$ is given by

$$F = -\frac{\mathrm{e}^{\mu_P}}{v_P} Z_P(\xi_A, \xi_B) - \frac{\mathrm{e}^{\mu_S}}{v_S} Z_S(\xi_S) + \sum_{\substack{JK \\ \in\{AB,BS,SA\}}} \int d\mathbf{r} \left[\chi_{\mathrm{JK}} \phi_J \phi_K - \xi_J \phi_J + \frac{\kappa_{\mathrm{J}}}{2} (\nabla \phi_{\mathrm{J}})^2\right]. \tag{3.8}$$

The Flory χ parameters and the square-gradient coefficients capture, respectively, the local and non-local part of the short-ranged interactions [24]. Their values are chosen to reproduce some known experimental properties of lipid membranes. The incompressibility condition $\phi_S + \phi_A + \phi_B = 1$ is used to eliminate ϕ_S and we have used the imaginary nature of the potential field variables at the saddle point to redefine the conjugate potential fields $i\xi \to \xi$ [23]. The partition functions that arise in Eq. (3.8) are for a single molecule in its respective field(s) and are given by $Z_S = \int d\mathbf{r} \mathrm{e}^{-v_S \xi_S}$ for the solvents and $Z_P = \int d\mathbf{r} q_A(\mathbf{r}; N_A) \mathrm{e}^{2v_A \xi_A} q_B^2(\mathbf{r}; N_B + 1)$ for the amphiphiles. The chain propagators q_A and q_B account for the chain connectivity and the Boltzmann weight due to the self-consistent potential field. They begin at the free ends and are used to obtain the single-chain statistics for each arm of the amphiphile. The total partition function for the amphiphile follows naturally by joining the propagators at the branch point, where an extra exponential factor $\mathrm{e}^{2v_A \xi_A}$ is included to correct for over-counting the joined monomer; see C for details on the chain propagator calculation. We then apply DSCF theory, together with the string method, to the free energy functional given by Eq. (3.8). In what follows, we discuss the main results.

3.3 Results

Consider a membrane under tension γ. If the membrane size is much larger than the size of the critical nucleus, we may regard pore formation and rupture as occurring at constant tension, which we implement as the boundary condition. In what follows, we work in the grand canonical ensemble, as it is most convenient for studying the MFEP. In this open system, the excess grand potential (Eq. (3.8) relative the bulk solution) per unit area directly gives the tension up to the rupture value, identified as the point of vanishing slope in Fig. 3.2 inset. This corresponds to a critical tension $\gamma_c \sim 4.77\ kT/\mathrm{nm}^2$ and an areal strain of ~ 0.6. The linear stretching modulus is found to be 170 mN/m, which falls within the range for lipid membranes, as determined from micropipette aspiration experiments [26]. Finally, to confirm that the results are independent of the ensemble choice, we repeat the same calculation in the canonical ensemble. In this closed system, the tension is evaluated according to

$$\gamma = f + a \left.\frac{\partial f}{\partial a}\right|_n . \tag{3.9}$$

Here f is the Helmholtz free energy per unit area and a is the area per lipid. The results from these two ensembles are identical.

The rupture captured above corresponds to the limit of metastability for a uniform membrane. In reality, thermal fluctuations and lipid rearrangements can nucleate pore formation and rupture when the membrane is subjected to a positive tension γ. If the timescale for nucleation is sufficiently long relative to the timescale for molecular relaxation, then the nucleation rate is of the form $\nu = \nu_0 \exp(-F^*/kT)$, where ν_0 is some transition frequency associated with the molecular relaxation. Assuming a molecular relaxation time on the order of 10 μs [27], nucleation will take place on experimentally relevant timescales if $F^* \lesssim \mathcal{O}(10\ kT)$. For any given tension, the DSCF-

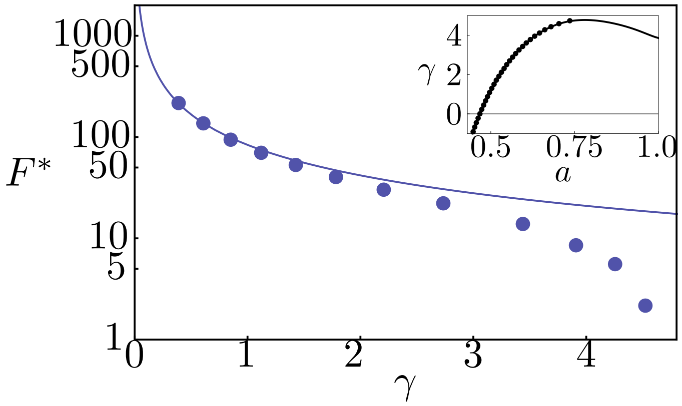

Figure 3.2: The free energy barrier as a function of the surface tension: DSCF-MFEP (markers) and CNT (line). Inset: the surface tension as a function of the area per lipid: grand canonical (markers) and canonical (line) ensemble.

MFEP calculations provide an exact description (within the mean-field framework) of the nucleation pathway. In Fig. 3.2, we plot the free energy barrier F^* as a function of the membrane tension γ on a log-linear plot. Also shown is the result from CNT [Eq. (3.6)], where the line energy σ is a phenomenological parameter that is assumed constant and used to describe the excess free energy cost associated with forming the rim of a pore. An equilibrium line energy is only well-defined for a pore with zero curvature in a tensionless membrane. Our SCF method determines this value ($\sigma_{eq} = 5.16\ kT/\text{nm}$) as input into the CNT. For small γ, the predictions from CNT agree well with the DSCF-MFEP calculations. Indeed, we expect CNT to become exact in the limit $\gamma = 0$. However, in this regime, the barrier is too high, and the rate vanishingly small, for nucleation to be a relevant mechanism. As γ increases, the free energy barrier decreases (reflecting the fact that the metastable intact membrane becomes less stable) and vanishes at the critical tension (γ_c), corresponding to the spinodal. From Fig. 3.2, CNT severely over-predicts the free energy barrier in the important regime where $\gamma \sim 3-4\ kT/\text{nm}^2$, and completely fails to capture the spinodal. To understand the source of discrepancy between CNT and our results, we examine the MFEP for three representative values of γ.

On the left panel of Fig. 3.3, we show the free energy profile and the line energy (inset) as a function of a reduced reaction coordinate, here taken to be the deficiency in the number of lipid molecules in the bilayer, m. We choose to use m rather than the radius r because the latter is only

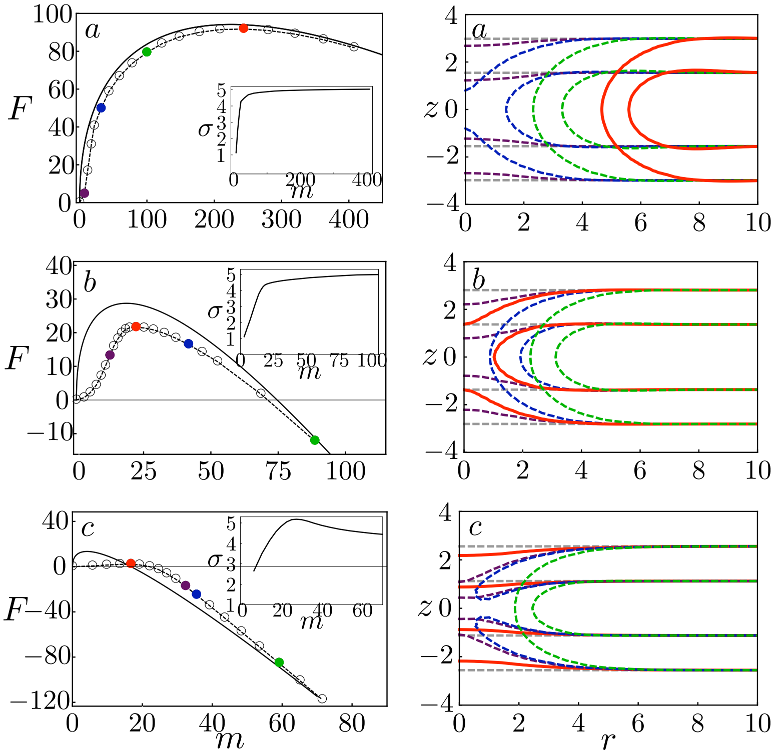

Figure 3.3: Left: Free energy as a function of the deficiency in the number of lipids: MFEP (dashed lines, states given by the colored markers) and CNT (solid lines). Right: density profiles for images along the respective MFEPs. The contour lines correspond to 25% of the maximum solvophilic (A) density of the initial intact membrane. In all cases, the critical nucleus is shown in red and the intact membrane in grey. From top to bottom: $\gamma_a, \gamma_b, \gamma_c = 0.85, 2.73, 4.52$.

well-defined for macroscopic pores. The free energies of the states along the MFEP are given by the markers and the prediction from CNT is given by the solid line. Here the line energy used for the CNT result is obtained from the respective membrane containing a pore with zero curvature. On the right panel, we plot the density profiles of the amphiphiles for selected states along the MFEP.

For $\gamma = 0.85\ kT/\text{nm}^2$ [Fig. 3.3(a)], except at the very initial stages, the MFEP closely follows the prediction from CNT, with the nucleation process largely involving the expansion of a well-defined solvophilic pore with negligible penetration of solvents. The density profile is nearly invariant (but shifted in radial direction) once the pore forms. For this low γ, the free energy barrier is $F^* = 92.18\ kT$, indicating that nucleation of a large pore leading to rupture is highly improbable. In fact, even smaller, transient pores are unlikely. The blue image where the membrane has not yet formed a pore already requires a substantial free energy cost. Next consider $\gamma = 2.73\ kT/\text{nm}^2$

[Fig. 3.3(b)] and observe that CNT over-predicts the free energy barrier and under-predicts the size of the critical nucleus. From the density profiles obtained from the DSCF-MFEP calculations, we see that the critical nucleus is not even a well-defined pore, but rather a “stalk” of solvophilic monomers that contains finer molecular structure than can be captured by CNT. Therefore, CNT is not a good model for the MFEP in the intermediate regime where $F^* = 21.59\ kT$. We note that a similar structure has been observed as a transition state [18] for the fusion of two bilayers. Finally, consider a membrane approaching the spinodal: $\gamma = 4.52\ kT/\mathrm{nm}^2$ [Fig. 3.3(c)]. Here CNT grossly over-predicts the nucleation barrier and under-predicts the size of the critical nucleus. In fact, the nucleation pathways predicted by the two methods qualitatively differ, with the CNT prediction crossing the MFEP and approaching it from below at large pore sizes. From the density profiles [Fig. 3.3(c), right], we find, not surprisingly, that a small perturbation involving local membrane thinning is enough to nucleate pore formation and rupture. Interestingly, rupture occurs even before the membrane is able to fully prepare for pore formation and a *solvophobic* hole that is penetrated by solvents forms in the membrane. Only afterwards do the amphiphiles rearrange to line the pore with solvophilic monomers and seal off the hole. This can be seen from the contour lines given in blue and green. The free energy barrier in this case is only twice the thermal energy, and hence we do not expect the picture of nucleation as a rare event to hold. However, with longer-chain amphiphiles, such as in the case of polymersomes [6], we expect a higher barrier height for the same amount of strain. Thus the scenario presented in this near-spinodal case can still be relevant.

To gain further insight, we separate the free energy from our DSCF-MFEP calculations into a piece involving the reduction in the elastic free energy, and other contributions. In analogy with CNT, we consider the reduction in the elastic energy to be given by the second term in Eq. (3.6), where we use the lipid number deficiency m and the area per lipid in a uniform membrane to define the pore size. For a macroscopic pore, m is related to the pore radius r as $r \sim \sqrt{m}$. The first term can then be considered an operational definition of the line energy σ, which now represents all the excess free energy to the elastic free energy. Figure 3.3 insets show the behavior of σ as a function of m. In all three cases, for sufficiently large pores, σ approaches a constant value less than the equilibrium value given earlier for the tensionless membrane ($\sigma_{eq} = 5.16\ kT/\text{nm}^2$). We also see that for small m, there is a strong size dependence in the line energy, including a nonmonotonic dependence for case (c) that captures the initial penalty for forming a solvophobic hole. Importantly, when the critical nucleus involves a pre-pore state with molecular features that cannot be captured by CNT, the size dependence of σ becomes important.

Finally, if we associate rupture as occurring when the nucleation barrier is surmountable on experimentally relevant time scales, our results indicate that the strain at which rupture occurs can be significantly lower than the strain at the limit of mechanical stability of the membrane. Thus, thermally nucleated rupture may be an important factor for the low rupture strains observed in lipid membranes [7].

3.4 Conclusion

In conclusion, we have combined the string method with DSCF theory to obtain the MFEP to pore formation and rupture for a range of membrane tensions. For the experimentally relevant regime where $F^* \lesssim \mathcal{O}(10\ kT)$, the critical nucleus is somewhere between a stalk-like structure [Fig. 3.3(b)] and a thinned membrane leading to a hole that is partially exposed to solvents [Fig. 3.3(c)]. In this regime, CNT fails to capture the important local rearrangements of the lipids and significantly overpredicts the nucleation barrier. Within the framework of mean-field theory for describing spatially localized fluctuation phenomena, the present work (and that by Cheng et al. [20]) represents the most advanced methodology in treating nucleation in soft condensed matter, including membranes. The combination of the string method and DSCF theory opens the way to studying a wide range of related membrane nucleation phenomena beyond pore formation and rupture, such as membrane fusion and fission [28, 29], and particle insertion and penetration [30].

This work was supported by the Joseph J. Jacobs Institute of Molecular Engineering for Medicine and the NSF Center for the Science and Engineering of Materials at Caltech, and by an NIH training grant (to C.L.T.).

Bibliography

[1] C. L. Ting and Z.-G. Wang, *Phys. Rev. Lett.* **106**, 168101 (2011).

[2] B. Alberts, A. Johnson, J. Lewis, M. Raff, K. Roberts, and P. Walter, *Molecular Biology of the Cell* (Garland Science, New York and Abingdon, 2007).

[3] L. Yang, T. M. Weiss, R. I. Lehrer, and H. W. Huang, *Biophys. J.* **79**, 2002 (2000).

[4] D. Zhelev and D. Needham, *Biochim. Biophys. Acta* **1147**, 89 (1993).

[5] J. Ghel, *Acta Physiol. Scand.* **177**, 437 (2003).

[6] B. M. Discher, Y.-Y. Won, D. S. Ege, J. C.-M. Lee, F. S. Bates, D. E. Discher, and D. A. Hammer, *Science* **284**, 1143 (1999).

[7] K. Olbrich, W. Rawicz, D. Needham, and E. Evans, *Biophys. J.* **79**, 321 (2000).

[8] O. Sandre, L. Moreaux, and F. Brochard-Wyart, *Proc. Natl. Acad. Sci. USA* **96**,10591 (1999).

[9] R. Netz and M. Schick, *Phys. Rev. E.* **53**, 3875 (1996).

[10] V. Talanquer and D. Oxtoby, *J. Chem. Phys.* **118**, 872 (2003).

[11] M. Muller and M. Schick, *J. Chem. Phys.* **105**, 8282 (1996).

[12] Z. Wang and D. Frenkel, *J. Chem. Phys.* **123**, 154701 (2005).

[13] T. Tolpekina, W. K. den Otter, and W. Briels, *J. Chem. Phys.* **121**, 12060 (2004).

[14] J. Wohlert, W. K. den Otter, O. Edholm, and W. J. Briels, *J. Chem. Phys.* **124**, 154905 (2006).

[15] W. K. den Otter, *J. Chem. Phys.* **131**, 205101 (2009).

[16] W. E, W. Ren, and E. Vanden-Eijnden, *J. Chem. Phys.* **123**, 154701 (2005).

[17] J. Fraaije, *J. Chem. Phys.* **99**, 9202 (1993).

[18] K. Katsov, M. Muller, and M. Schick, *Biophys. J.* **87**, 3277 (2004).

[19] H. Morita, T. Kawakatsu, and M. Doi, *Macromolecules* **34**, 8777 (2001).

[20] X. Cheng, L. Lin, W. E., P. Zhang, and A.-C. Shi, *Phys. Rev. Lett.* **104**, 148301 (2010).

[21] J. Litster, *Phys. Lett. A* **53**, 193 (1975).

[22] C. Taupin, M. Dvolaitzky, and C. Sauterey, *Biochemistry* **14**, 4771 (2009).

[23] G. H. Fredrickson, *The Equilibrium Theory of Inhomogeneous Polymers* (Oxford University Press, New York, 2005).

[24] K. Hong and J. Noolandi, *Macromolecules* **13**, 964 (1980).

[25] C. L. Ting and Z.-G. Wang, *Biophys. J.* **100**, 1288 (2011).

[26] D. Needham and R. Nunn, *Biophys. J.* **58**, 997 (1990).

[27] G. Crawford and J. Earnshaw, *Biophys. J.* **52**, 87 (1987).

[28] L. Chernomordik, G. Melikyan, and Y. Chizmadzhev, *Biochim. Biophys. Acta* **906**, 309 (1987).

[29] T. Baumgart, S. Hess, and W. Webb, *Nature* **425**, 821 (2003).

[30] S. P. Hong, A. U. Bielinska, A. Mecke, B. Keszler, J. L. Beals, X. Shi, L. Balogh, B. G. Orr, J. R. Baker, Jr., M. M. Banaszak Holl, *Bioconjugate Chem.* **15**, 774 (2004).

Chapter 4

Minimum Free Energy Paths for a Nanoparticle Crossing the Bilayer Membrane

Within self-consistent field theory, we develop an “on-the-fly” string method to compute the minimum free energy path for several activated processes involving a charged, solvophobic nanoparticle and a lipid membrane. Under tensions well below the mechanical stability limit of the membrane, and in the regime where nucleation can occur on experimentally relevant time scales, our study suggests that there can be at least three competing pathways for crossing the membrane: (1) particle-assisted membrane rupture, (2) particle insertion into a metastable pore followed by translocation and membrane resealing, and (3) particle insertion into a metastable pore followed by membrane rupture. In the context of polymer-based gene delivery systems, we discuss the implications of these results for the endosomal escape mechanism.

4.1 Introduction

The interaction of nanoparticles with lipid membranes is a common theme underlying a number of important topics in bionanotechnology, ranging from cytotoxicity [1] to the delivery of therapeutics [2]. In polymer-based gene delivery systems [3], the nanoparticle is comprised of genetic material condensed with cationic polymers. Once internalized by the cell via endocytosis, the nanoparticles are enclosed within membrane-bound vesicles called endosomes, and are trafficked along the endolysosomal pathway, where acidification activates hydrolytic enzymes [4]. Hence, the nanoparticle must escape the endosome before crossing the nuclear envelope for successful gene expression. Clearly, membrane-particle interactions play a central role in several key steps along the gene delivery pathway. In particular, understanding the endosomal escape mechanism provides a direct motivation for the work described in this chapter.

In the proton-sponge hypothesis [5–7], the nanoparticle plays an *indirect* role in its own endosomal escape by serving as a buffering substrate for protons. As additional protons are pumped into the endosome with an attendant influx of counterions, the increase in osmotic pressure translates to increased tension on the endosomal membrane. Eventually the membrane ruptures, thus releasing the trapped nanoparticles into the cytosol. Importantly, membrane rupture is a thermally nucleated process [8–13] under the small-to-moderate tensions generated in the proton sponge hypothesis [7,14]. It is therefore possible to imagine that the nanoparticle takes a more *direct* role in the endosomal escape by interacting directly with the membrane to lower the nucleation barrier for rupture. We examine this scenario in the broader context of nucleated pathways involving membrane-particle interactions.

A number of computational studies on membrane-particle systems have been conducted to elucidate the equilibrium structures [15–19], as well as the dynamics under (nearly) spontaneous conditions [20, 21] or when induced by an external force [22]. However, these studies have not addressed the thermally nucleated processes we are interested in here. Besides the long time scales associated with these rare events, a significant challenge arises because of the high dimensional free energy surface due to the conformation degrees of freedom of the lipid molecules, characteristic of many soft matter systems. Hence, with any sizable nucleation barrier, direct computer simulation is unfeasible. The potential of mean constraint force method attempts to overcome this challenge by artificially choosing a reaction coordinate that (in general) does not coincide with the true nucleation pathway, while the transition path sampling method [23, 24] is impractical for systems involving large assemblies of complex molecules.

Recently, two groups [13, 25] have developed a powerful mean-field technique for studying minimum free energy paths (MFEP) in self-assembled polymeric systems. The technique combines the self-consistent field theory (SCFT) [26] with the string method [27,28], and overcomes the aforementioned time scale and dimensionality challenges. Ting et al. [13] have applied this technique to study nucleated pore formation and rupture in membrane bilayers; see also Chapter 3. To explore nucleated pathways involving the membrane-nanoparticle interactions of interest here, we must further account for the particle degree of freedom. This highly nontrivial task requires additional development in the methodology. We therefore start with a description of the model and method.

4.2 Model and Method

Our membrane bilayer consists of double-tailed amphiphiles (A) assembled in explicit solvent (S) containing ions ($\pm$). The amphiphiles are modeled as discrete Gaussian chains having a solvophilic head (H) segment of N_H negatively charged monomers with volume v_H and two solvophobic tail (T) segments, each consisting of N_T monomers with volume v_T. The solvents are modeled as monomers with volume v_S and the ions are represented as monovalent point charges of the elementary charge e. The short-ranged repulsion involving the monomer units is represented by an incompressibility condition everywhere in the system. We work in the grand canonical ensemble, where the number of molecules are determined from their respective chemical potentials μ_J ($J = A, S, \pm$). In addition to the fluid species, there is a positively charged nanoparticle (P), whose density profile is defined by a cavity function that excludes the fluid species from its interior:

$$h_P(|\mathbf{r} - \mathbf{r}_P|) = \frac{1}{2}\left(1 + \tanh[(R_P - |\mathbf{r} - \mathbf{r}_P|)/w]\right). \tag{4.1}$$

Here, R_P is the particle radius, w is the width of the interface and $\mathbf{r}_P$ is the particle position [29,30].

The essential contributions to the model are the chain connectivity of the amphiphiles, the incompressibility condition, the short-ranged pairwise interactions and the long-ranged electrostatic interactions. The derivation of the SCFT is described in detail in Refs. [13,18,26] and also Appendix

B. The final expression for the grand potential is:

$$
\begin{aligned}
F = &-\frac{\mathrm{e}^{\mu_A}}{v_A} Z_A[\xi_H, \xi_T] - \frac{\mathrm{e}^{\mu_S}}{v_S} Z_S[\xi_S] - \frac{\mathrm{e}^{\mu_\pm}}{v_\pm} Z_\pm[\psi] \\
&+ \int d\mathbf{r} \left\{ \sum_{JK} \left[\chi_{JK}\phi_J\phi_K + \frac{\kappa_J}{2}\left|\nabla\phi_J\right|^2 - \xi_J\phi_J \right] + \chi_{TP}\phi_T h_P + \psi\rho_c - \frac{\epsilon}{2}\left|\nabla\psi\right|^2 \right\}.
\end{aligned}
\tag{4.2}
$$

Here the summation is over $JK \in \{HT, TS, SH\}$ and the fields ϕ_J, ξ_J, and ψ denote the monomer volume fraction, its conjugate potential, and the electrostatic potential fields, respectively. For notational conciseness we omit the $\mathbf{r}$ dependence in these field variables. The partition functions in the first line account for the Boltzmann weight of a single molecule in its respective field(s), and are given by

$$
\begin{aligned}
Z_A[\xi_H, \xi_T] &= \int d\mathbf{r} q_H(\mathbf{r}, N_H) \mathrm{e}^{2v_H\xi_H} q_T^2(\mathbf{r}, N_T + 1), \\
Z_S[\xi_S] &= \int d\mathbf{r} \exp\{-v_S\xi_S\}, \\
Z_\pm[\psi] &= \int d\mathbf{r} \exp\{\mp\psi e - u_\pm^b\},
\end{aligned}
\tag{4.3}
$$

for the amphiphiles, solvents, and ions, respectively. Here q_H and q_T are the chain propagators used to obtain the single-chain statistics for each arm of the amphiphile [18]; see also Appendix C.

$$
u_\pm^b = e^2(8\pi a_\pm \epsilon)^{-1} \tag{4.4}
$$

is the Born self-energy of an ion, where ϵ is the spatially varying dielectric constant (assumed to be a simple local volume-fraction weighted average) and $a_\pm = 0.1$ nm is the Born radius.

In Eq. (4.2), the local and nonlocal parts of the pairwise interactions are captured by χ_{JK} and κ_J, respectively [31]. Their values (see Table 4.1) are chosen to reproduce some known experimental properties of lipid membranes; in particular, the linear stretching modulus for our model is found to be 210 mN/m [32]. The solvophobicity of the nanoparticle is modeled by a Flory-like parameter χ_{TP} that acts locally over the interfacial region of the particle and the total fixed charge density is defined $\rho_c = c_P h_P + (c_H/v_H)\phi_H$. Here c_P is the charge density on the nanoparticle and $c_H = -0.05$ is the

i	v_i	N_i	ϵ_i	κ_i	χ_{iH}	χ_{iT}	χ_{iS}
H	l0.05	5	50	0	—	75	—
T	0.05	10	2	8	—	—	22
S	0.15	1	80	0	0	—	—

Table 4.1: (L to R) The monomer volume, number of monomers, dielectric value [33], gradient coefficient, and Flory parameters. $c_{\pm} = 100$ mM for the bulk ion concentration.

charge per head monomer. The SCF equations are obtained by requiring that Eq. (4.2) be stationary with respect to variations in the fields, i.e., $\frac{\partial F}{\partial \omega}|_{\omega^*} = 0$, where $\omega = \phi_I, \xi_I, \psi$. These equations are then solved iteratively until convergence, with the solutions corresponding to (meta)stable equilibrium states of the system.

However, our interest here is in the nucleation pathways between equilibrium states, and in particular the transition state, i.e., the critical nucleus. To map out these pathways, which necessarily include nonequilibrium states, we apply the string method to Eq. (4.2). Briefly, we begin with a string of discrete states in the space defined by the density fields of the monomer species and the nanoparticle. The string is relaxed towards the MFEP by a two-step iterative procedure: (1) an evolution equation describing the steepest descent dynamics on the free energy landscape and (2) a redistribution of the states along the string. The latter step is key, as it prevents all the states from falling into one of the trivial equilibrium solutions. While the string method is easily implemented on a known free energy landscape, in SCFT the free energy as a functional of the densities is not known *a priori*. Thus we take an "on the fly" approach to traverse the free energy landscape by evaluating the gradients of Eq. (4.2) using a combination of the external potential dynamics (EPD) [34] and hybrid particle field (HPF) [29] methods.

More specifically, we first evolve the states for some time Δt according to the steepest descent dynamics of the density fields. This approach is similar to that taken in dynamic SCFT [35], but for computational convenience (see also Ceniceros and Fredrickson [36] for the target density problem), we choose to reformulate the dynamics in terms of the fields ξ_I, using the EPD method:

$$\frac{\partial \xi_I}{\partial t} = D_1 \frac{\delta F}{\delta \phi_I}. \tag{4.5}$$

Here D_1 is a scalar mobility coefficient and $\delta F/\delta\phi_I$ is the familiar functional derivative of Eq. (4.2) so that ξ_I is updated by simple time iteration methods [37]. ϕ_I follows as usual by solving the modified diffusion equation for the chain propagators in the presence of the new ξ_I [18]. Next, we evolve the particle position $\mathbf{r}_P$ according to the HPF method developed by Sides et al. [29]:

$$\frac{\partial \mathbf{r}_P}{\partial t} = -D_2 \frac{\partial F}{\partial \mathbf{r}_P} = -D_2 \frac{\delta F}{\delta h_P} \mathbf{g}(\mathbf{r_p} - \mathbf{r}), \tag{4.6}$$

where $\mathbf{g}(\mathbf{r}) \equiv \frac{1}{r}\frac{dh_P(r)}{dr}\mathbf{r}$ is a vector function related to the derivative of the cavity function. The density fields and the particle position are then updated, subject to the incompressibility condition.

The second step in the string method involves a redistribution of the states along the string. In the simplest case, this is enforced by an equal arc-length reparametrization of the string based on the current densities, followed by a linear interpolation to obtain the new densities. The two dynamical equations [Eq. (4.5) and Eq. (4.6)], followed by the reparametrization, are computed at every time step. Once converged, the string coincides with the MFEP. In what follows, we discuss the main results.

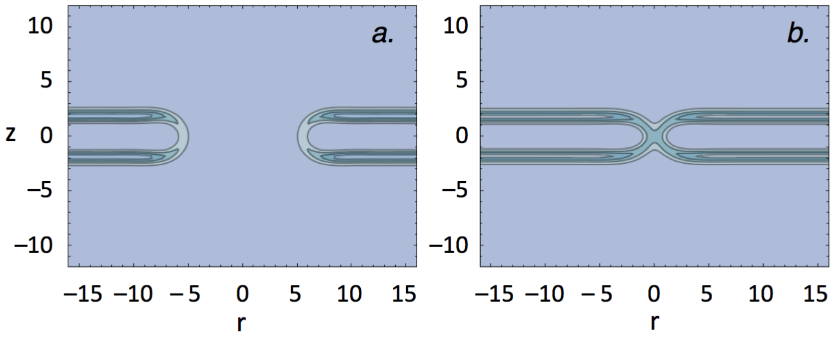

Figure 4.1: The transition state for homogeneous membrane rupture when $\gamma = 0.6$ (a) and $\gamma = 1.9$ (b). Contour plots show the lipid head densities in cylindrical coordinates.

4.3 Results

To understand the effect of the nanoparticle on membrane pore formation and rupture, we first consider the case in the absence of the nanoparticle, i.e., homogeneous rupture. The free energy

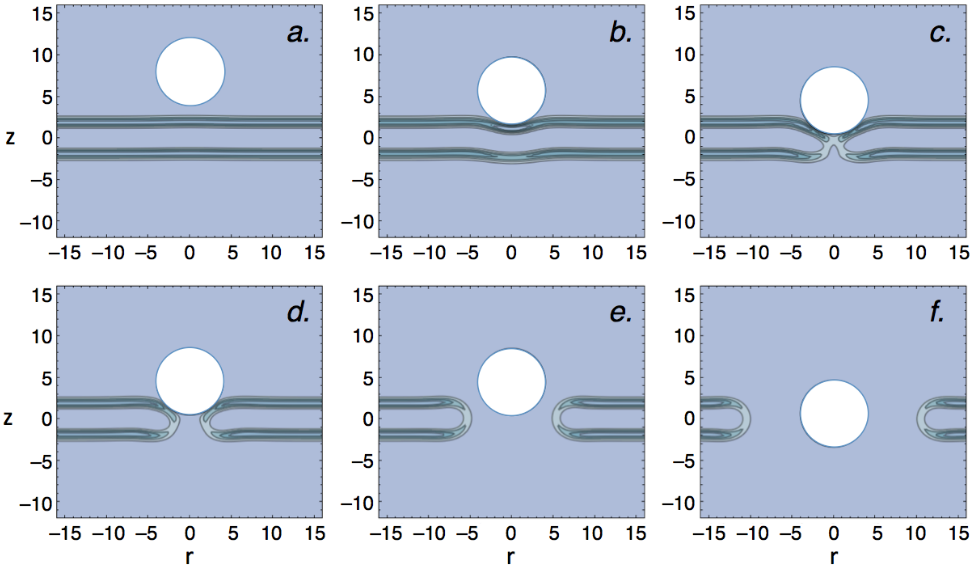

Figure 4.2: Membrane under low tension ($\gamma = 0.6$): states along the MFEP for membrane rupture in the presence of a nanoparticle ($R_P = 4$, $c_P = 0.5$, $\chi_{TP} = 0$)

barrier F_0^* diverges for a tensionless membrane and vanishes at a threshold tension $\gamma_t = 5.1$, corresponding to the onset of mechanical instability. The structure and free energy of the transition state in the intermediate regime will depend on the membrane tension. For low tensions ($\gamma = 0.6$) the transition state corresponds to a well-defined pore with $F_0^* = 75$, whereas for higher tensions ($\gamma = 1.9$) the transition state corresponds to a solvophilic stalk with $F_0^* = 24$; see Fig. 4.1. Assuming an Arrhenius rate expression of the form $k = \nu \exp[-F^*]$, where $\nu \sim 10$ μs is a transition frequency associated with the molecular relaxation [38], nucleation will take place on experimentally relevant time scales if $F^* \lesssim 25$. Thus, nucleation is a relevant mechanism for homogeneous rupture of a membrane under moderate tensions ($\gamma \gtrsim 1.9$).

Next, we proceed to examine the effect of a charged and/or solvophobic nanoparticle on the nucleation barrier to rupture, beginning with the low tension case ($\gamma = 0.6$). The string is initialized between two fixed end states [see Fig. 4.2(a) and (f)] and evolved according to the algorithms described earlier. The resulting MFEP reveals the following nucleation pathway. Through electrostatic attraction, the positively charged particle adsorbs onto the surface of the negatively charged membrane. This metastable state is shown in (b). From here, rupture takes place by a two-step nucleation process. First, the particle pushes into and punctures the membrane, overcoming the first

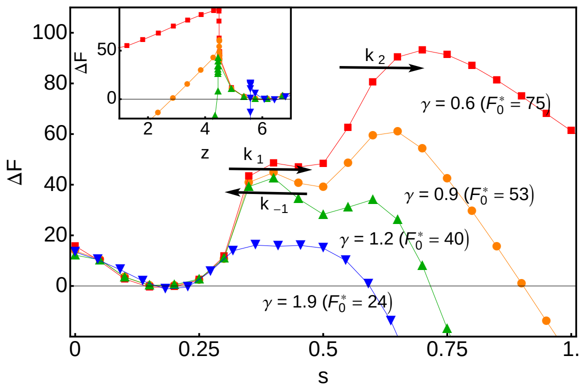

Figure 4.3: The MFEP for membrane rupture in the presence of a nanoparticle ($R_P = 4$, $c_P = 0.5$, $\chi_{TP} = 0$), as a function of the reaction coordinate s and the particle position z (inset) for several values of tension. The nucleation barrier for homogeneous rupture is shown in parentheses.

barrier; see (c). Note that the trans leaflet, which is already thinned in (b), is broken first, and the cis leaflet is held intact by the electrostatic attraction to the particle. Once the membrane bilayer is broken, the particle sits in a highly transient metastable pore that is lined by lipid head groups, as shown in (d). From here the membrane can expel the particle and reseal the defect. However to proceed to rupture, the pore must expand to some critical radius r^*; see (e). Importantly, $r^* > R_P$ for this case and hence the second transition state in the two-step nucleation pathway is essentially the same as the transition state for homogeneous rupture; compare (e) with Fig. 4.1(a).

In Fig. 4.3, the MFEP for rupture in the presence of a particle is plotted as a function of the true reaction coordinate s that defines the set of images along the string, and also as a function of the particle position z, for several values of membrane tension. In all cases, the charged nanoparticle first adsorbs onto the surface of the membrane, stabilizing the initial state. For the low tension case ($\gamma = 0.6$), rupture then proceeds by the two barrier crossings described above: puncturing the membrane with rate k_1 [Fig. 4.2(c)] and expanding the pore with rate k_2 [Fig. 4.2(e)]. The first of these is reversible, with backward rate k_{-1}, and the second, irreversible. Intermediate to the two transition states is the transient, metastable pore [Fig. 4.2(d)]. The mean first-passage time for this two-step nucleation process is given by

$$\tau = \frac{1}{k_1} + \frac{k_{-1}}{k_1 k_2} + \frac{1}{k_2}, \tag{4.7}$$

and the nucleation rate may be approximated as $J = \tau^{-1}$ [39,40]. Here, breaking the surface of the membrane is the more energetically costly step, with $F_1^* = 51$. Furthermore, because the reverse rate k_{-1} for the transient state to expel the particle and reseal the pore is high ($F_{-1}^* = 3$, whereas $F_2^* = 45$), rupture can effectively be considered crossing a single barrier with $F^* = 93$. Recall $F_0^* = 75$ for homogenous rupture; thus, for a membrane under low tension the particle does not assist in rupture.

In the proton sponge hypothesis, the membrane tension is believed to play an important role in the endosomal escape [7]. We find that with increasing tension, the metastable pore becomes more stable with respect to resealing k_{-1} but less stable with respect to rupture k_2, and eventually unstable altogether; see Fig. 4.3. In particular, for $\gamma = 1.9$ rupture becomes a one-step nucleation process. To understand this result, recall that for this tension the transition state for homogeneous rupture is a solvophilic stalk with $F_0^* = 24$ [Fig. 4.1(b)]. The transition state for particle-assisted membrane rupture also corresponds to a solvophilic stalk [Fig. 4.4(c)], but with a reduced barrier $F^* = 18$ (Fig. 4.3). Here the positively charged nanoparticle is able to interact with both leaflets of the membrane to facilitate the formation of the stalk-like structure, thereby lowering the nucleation barrier to rupture. This result suggests a *direct* role of the nanoparticle in the endosomal escape, not previously envisioned in the proton sponge hypothesis, and illustrates the importance of having an induced tension on the membrane.

Next, we consider particle translocation as an alternate path for the endosomal escape. Here the particle crosses without rupturing the membrane. Beyond the delivery of medical therapeutics,

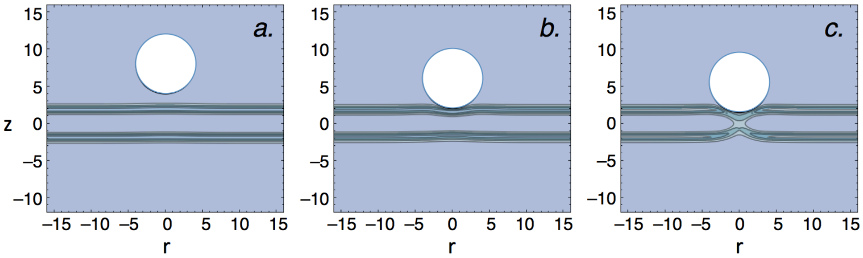

Figure 4.4: Membrane under moderate tension ($\gamma = 1.9$): states along the MFEP for membrane rupture in the presence of a nanoparticle ($R_P = 4$, $c_P = 0.5$, $\chi_{TP} = 0$)

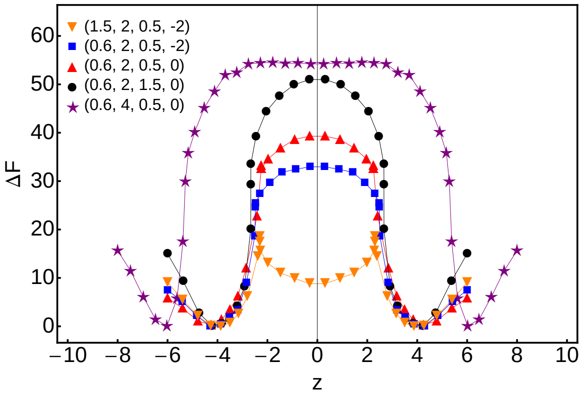

Figure 4.5: The MFEP for particle translocation as a function of the particle position z for different tensions and particle parameters, corresponding to $(\gamma, R_P, c_P, \chi_{TP})$

particle translocation is of interest for understanding the mechanisms of nanoparticle cytotoxicity [41] and viral cell entry [42], and is therefore of interest in its own right. We return to the membrane under low tension ($\gamma = 0.6$) and the same particle considered previously. The critical pore radius of the transition state for rupture is larger than the radius of the particle. For successful translocation the particle only needs to create a pore large enough to pass through, and thus we expect translocation to be the preferred pathway over rupture. Although still highly unlikely, translocation is indeed the more favorable mechanism for crossing the membrane, where $F^* = 54$ (Fig. 4.5$\star$).

To lower the barrier to the regime where translocation can occur on experimentally relevant time scales, we consider the effects of the particle size, charge, and solvophobicity. Particles smaller than the critical pore radius for homogeneous rupture should translocate more easily. Reducing the particle size to $R_P = 2$ while maintaining the same charge density and solvophobicity, we find that the free energy barrier is indeed lowered to $F^* = 39$ (Fig. 4.5$\triangle$), which is still on the high side for thermally nucleated translocation. With the reduced particle size, we increase the charge density to $c_P = 1.5$, and find the free energy barrier is *increased* to $F^* = 51$ (Fig. 4.5$\circ$). This result can be rationalized by noting that the density of negatively charged amphiphilic heads is higher for an intact membrane compared to a pore with high curvature. Thus the particle gains more favorable electrostatic interactions by adsorbing onto the surface rather than inserting into a pore. If instead we increase the particle solvophobicity by setting $\chi_{TP} = -2$, the particle is able to interact with the solvophobic tail region of the membrane, thereby *lowering* the free energy barrier for translocation to $F^* = 33$ (Fig. 4.5$\square$).

Based on these results, we find that translocation of a charged and/or solvophobic nanoparticle through a membrane under low tension is unlikely to occur by thermal nucleation. However, particle translocation becomes possible upon increasing the membrane tension. Taking the particle with the lowest free energy barrier for translocation ($R_P = 2$, $c_P = 0.5$, $\chi_{TP} = -2.0$), we increase the membrane tension to $\gamma = 1.5$ and find that the particle inserted into the middle of the membrane is now a metastable state along the MFEP; see (Fig. 4.5$_\triangledown$). Translocation is now a two-step process, the first barrier corresponding to particle insertion, with $F_1^* = 19$, and the second barrier corresponding to expelling the particle and resealing the pore, with $F_2^* = 10$. Using Eq. (4.7), we compute the nucleation rate for translocation and find $J = \nu \exp[-19.6]$, indicating that the process can occur on experimentally relevant time scales.

Interestingly, the critical nucleus for homogeneous rupture in this case is a pore on the order of the size of the particle. Therefore, the electrostatic attraction between the positively charged nanoparticle and the negatively charged amphiphilic heads are able to stabilize the pore, preventing rupture. Based on this result, we can imagine a third pathway for crossing the membrane barrier: particle insertion into the metastable pore followed by rupture. From our MFEP calculation, we find $F_1^* = 19$ and $F_{2'}^* = 8$ for insertion and rupture, respectively, so that the overall nucleation rate for crossing the two barriers is $J = \nu \exp[-19.1]$. Note that in the earlier mechanism depicted in Fig. 4.2 and Fig. 4.3, the metastable state is a partially punctured membrane, whereas here the metastable state is a membrane pore with a fully inserted particle.

4.4 Conclusion

We conclude with some general remarks on nucleated pathways for a nanoparticle to cross the bilayer membrane, and some implications for the endosomal escape in gene delivery systems. Our results indicate at least three competing pathways: (1) particle-assisted membrane rupture, (2) particle translocation followed by membrane resealing, and (3) particle insertion into a metastable pore followed by membrane rupture. These results suggest a direct role of the nanoparticle in the endosomal escape, not envisioned in the proton sponge hypothesis. In all cases, sufficiently high membrane tension is required for the nucleation barriers to be surmountable on realistic time scales, suggesting that the osmotic pressure component of the proton sponge hypothesis is crucial for the successful endosomal escape of the nanoparticles. This conclusion is consistent with the theoretical work of Yang and May [14], which found that the nanoparticle alone would not lead to enough osmotic pressure to induce sufficient membrane tension, and that some excess free polymers are needed. Experimental studies revealed that the presence of these free polymers can increase the gene transfection efficiency by up to two orders of magnitude [43,44]. In what follows, we summarize our findings on the three nucleated pathways.

For particle-assisted membrane rupture, a key consideration is the membrane structure at the transition state, which is primarily controlled by the membrane tension. In particular, the membrane tension must be sufficiently high, so that the size of the critical nucleus (e.g., a solvophilic stalk) is on the order of the particle radius. Once this criterion is met, the charges on the particle should be enough to promote the adsorption onto and subsequent puncture of the membrane but not so much as to stabilize the pore. The particle solvophobicity is unimportant in this case, since rupture occurs before the particle has had significant interaction with the solvophobic tail region of the membrane.

In the case of particle translocation, increasing particle charge *increases* the barrier because the particle gains more favorable electrostatic interactions by adsorbing onto the surface of the membrane rather than inserting into a pore. In contrast, increasing particle solvophobicity *decreases* the barrier for translocation because the particle inserted into a pore can interact favorably with the lipid tails. Again, membrane tension is critical to reaching barriers surmountable on realistic time scales. With sufficient tension, the pore with a particle inserted into the center of the membrane becomes a metastable state on the MFEP to translocation. This state suggests—and indeed we find—another nucleated pathway from this metastable state: pore expansion, leading to rupture.

The mode of crossing the membrane bilayer depends on the membrane tension and the particle properties. Here, we have considered particle radius, charge density and solvophobicity. Even within this set of parameters, we have not exhaustively explored the space for the most likely nucleation pathways. With the introduction of other types of interactions, for example, specific ligand-receptor interactions [21] or different geometries [22], it should be possible that any of the pathways can become most favorable. The types of calculations illustrated in this work can be used to identify the optimal conditions for selecting a particular pathway.

Finally, the methodology developed in this work represents the most advanced theoretical technique for describing nucleation pathways in soft condensed matter systems that also include hard-particle degrees of freedom. We expect the method to be useful for studying a wide range of nucleation phenomena beyond membrane systems, for example, in nanoparticle polymer composites [29, 45, 46].

The authors wish to thank Daniel Appelö for many helpful discussions. This work was supported by the Joseph J. Jacobs Institute for Molecular Engineering for Medicine and by a Sandia National Laboratory Fellowship to C.L.T.

Bibliography

[1] N. Lewinski, V. Colvin, and R. Drezek, *Small* **4**, 26 (2008).

[2] R. Duncan, *Nat. Rev. Drug Discov.* **2**, 347 (2003).

[3] D. W. Pack, A. S. Hoffman, S. Pun, and P. S. Stayton, *Nat. Rev. Drug Discov.* **4**, 581 (2005).

[4] B. Alberts, A. Johnson, J. Lewis, M. Raff, K. Roberts, and P. Walter, *Molecular Biology of the Cell* (Garland Science, New York and Abingdon, 2007).

[5] J. Haensler and F. C. Szoka, *Bioconj. Chem.* **4**, 372 (1993).

[6] J. Behr, *Chimia*, **51**, 34 (1997).

[7] N. D. Sonawane, F. C. Szoka, and A. S. Verkman, *J. Biol. Chem.* **278**, 44826 (2003).

[8] L. Fournier and B. Joós, *Phys. Rev. E* **67**, 051908 (2003).

[9] V. Talanquer and D. Oxtoby, *J. Chem. Phys.* **118**, 872 (2003).

[10] T. Tolpekina, W. den Otter, and W. Briels, *J. Chem. Phys.* **121**, 12060 (2004).

[11] O. Farago and C. D. Santangelo, *J. Chem. Phys.* **122**, 044901 (2005).

[12] P. A. Boucher, B. Joós, M. J. Zuckermann, and L. Fournier, *Biophys. J.* **92**, 4344 (2007).

[13] C. L. Ting, D. Appelö, and Z.-G. Wang, *Phys. Rev. Lett.* **106**, 168101 (2011).

[14] S. Yang and S. May, *J. Phys. Chem.* **129**, 185105 (2008).

[15] V. V. Ginzburg and S. Balijepalli, *Nano Lett.* **7**, 3716 (2007).

[16] A. Alexeev, W. E. Uspal, and A. C. Balazs, *ACS Nano* **2**, 1117 (2008).

[17] Y. Li and N. Gu, *J. Phys. Chem. B* **114**, 2749 (2010).

[18] C. L. Ting and Z.-G. Wang, *Biophys. J.* **100**, 1288 (2011).

[19] R. C. Van Lehn and A. Alexander-Katz, *Soft Matter* **7**, 11392 (2011).

[20] H. Lee and R. G. Larson, *Molecules* **14**, 423 (2009).

[21] R. Vácha, F. J. Martinez-Veracoechea, and D. Frenkel, *Nano Lett.* **11**, 5391 (2011).

[22] K. Yang and Y. Q. Ma, *Nat. Nanotech.* **5**, 579 (2010).

[23] C. Dellago, P. G. Bolhuis, F. S. Csajka, and D. Chandler, *J. Phys. Chem.* **108**, 1964 (1998).

[24] P. G. Bolhuis, D. Chandler, C. Dellago, and P. L. Geissler, *Annu. Rev. Phys. Chem.* **53**, 291 (2002).

[25] X. Cheng, L. Lin, W. E, P. Zhang, and A.-C. Shi, *Phys. Rev. Lett.* **104**, 148301 (2010).

[26] G. H. Fredrickson, *The Equilibrium Theory of Inhomogeneous Polymers* (Oxford University Press, New York, 2005).

[27] W. E, W. Ren, and E. Vanden-Eijnden, *Phys. Rev. B* **66**, 052301 (2002).

[28] W. E, W. Ren, and E. Vanden-Eijnden, *J. Chem. Phys.* **126**, 164103 (2007).

[29] S. W. Sides, B. J. Kim, E. J. Kramer, and G. H. Fredrickson, *Phys. Rev. Lett.* **96**, 250601 (2006).

[30] M. W. Matsen and R. B. Thompson, *Macromolecules* **41**, 1853 (2008).

[31] K. Hong and J. Noolandi, *Macromolecules* **13**, 964 (1980).

[32] D. Needham and R. Nunn, *Biophys. J.* **58**, 997 (1990).

[33] H. Brockman, *Chem. Phys. Lipids* **73**, 57 (1994).

[34] N. M. Maurits and J. G. E. M. Fraaije, *J. Chem. Phys.* **107**, 5879 (1997).

[35] J. G. E. M. Fraaije, *J. Chem. Phys.* **99**, 9202 (1993).

[36] H. D. Ceniceros and G. H. Fredrickson, *Multiscale Model. Sim.* **2**, 452 (2004).

[37] X. He and F. Schmid, *Macromolecules* **39**, 2654 (2006).

[38] G. Crawford and J. Earnshaw, *Biophys. J.* **52**, 87 (1987).

[39] N. G. van Kampen, *Stochastic Processes in Physics and Chemistry* (Elsevier, New York, 1992).

[40] W. Pan, A. B. Kolomeisky, and P. G. Vekilov, *J. Chem. Phys.* **122**, 17905 (2005).

[41] F. Zhao, Y. Zhao, Y. Liu, X. L. Chang, C. Y. Chen, and Y. L. Zhao, *Small* **7**, 1322 (2011).

[42] A. J. Cann, *Principles of Molecular Virology* (Academic Press, 2001).

[43] S. Boeckle, K. von Gersdorff, S. van der Piepen, C. Culmsee, E. Wagner, and M. Ogris, *J. Gene Med.* **6**, 1102 (2004).

[44] Y. Yue, F. Jun, R. Deng, J. Cai, Y. Chen, M. C. M. Lin, H.-F. Kung, and C. Wu, *J. Control. Release* **155**, 67 (2011).

[45] R. B. Thompson, V. V. Ginzburg, M. W. Matsen, and A. C. Balazs, *Science* **292**, 2469 (2001).

[46] A. C. Balazs, T. Emrick, and T. P. Russell, *Science* **314**, 1107 (2006).

Chapter 5

Beyond the Endosomal Escape

5.1 A Kinetic Model for the Enzymatic Action of Cellulase

We develop a mechanochemical model for the dynamics of cellulase, a two-domain enzyme connected by a peptide linker, as it extracts and hydrolyzes a cellulose polymer from a crystalline substrate. We consider two random walkers, representing the catalytic domain (CD) and the carbohydrate binding module (CBM), whose rates for stepping are biased by the coupling through the linker and the energy required to extract the cellulose polymer from the crystalline substrate. Our results show that the linker length and stiffness play a critical role in the cooperative action of the CD and CBM. Specifically, for a given linker length the steady-state hydrolysis shows a maximum at some intermediate linker stiffness, corresponding to a transition of the linker from a compressed to an extended conformation. Here the system exhibits maximum fluctuation, as measured by the variance of the separation between the two domains and the dispersion around the mean hydrolysis speed. In the range of experimentally known values for the parameters in our model, improving the intrinsic hydrolytic activity of the CD leads to a proportional increase in the overall hydrolysis rate [1]

5.1.1 Introduction

Cellulosic ethanol is a renewable, carbon neutral source of energy with the added benefit of possessing excellent liquid fuel properties. Economic production of ethanol from cellulosic biomass on commercial scales will help reduce our dependence on fossil fuels. Towards this aim, research efforts made to commercialize the process include, but are not limited to, the following areas [2]: (i) developing improved feedstocks, (ii) overcoming biomass recalcitrance through enhanced pretreatment options and more efficient enzymes, (iii) improving ethanol fermentation and recovery methods, and (iv) minimizing enzyme production costs. Although a concerted approach involving all aspects in the biomass-to-ethanol conversion will be necessary in surmounting the economic challenges, perhaps the greatest leverage arises from (ii) above, for which efforts are being made to develop better enzymes using, for example, directed evolution and protein engineering [3]. In this respect, a molecular, mechanistic understanding of how cellulase hydrolyzes the recalcitrant biomass can guide the design of more efficient enzymes.

Cellulase consists of two domains—a carbohydrate binding module (CBM) and a catalytic domain (CD)—connected by a peptide linker; see Fig. 5.1. How these two domains work together to extract a single polysaccharide chain from the crystalline cellulose and achieve the desired hydrolysis is a question of considerable controversy. In particular, the role of the linker region between the two domains is not known. Experimental efforts to reveal the structure of the linker remain inconclusive [4–6], while molecular dynamics simulations are limited by the inordinately long computation time necessary to model both the large size of the enzyme/substrate complex and the long timescale for the motion of the enzyme. For example, recently reported results based on nanosecond timescales concluded that the peptide linker is too flexible to store energy in a manner similar to spring [7]. This was subsequently contradicted by free energy calculations from the same group [8]. Developing a fully atomistic model is clearly a nontrivial task with current computation power.

In this chapter, we develop a mechanochemical model, whereby the free energy gain from the cellulose hydrolysis provides the driving force for the motion of the CD, which is then coupled to the motion of the CBM through the linker. Rather than attempt to accurately model the atomistic details of the system, we develop a stochastic model that captures the kinetic rates of the processive CD and the random CBM. Importantly, the model accounts for the mechanical deformation of the peptide linker joining the two domains and the energetics of the hydrogen bond disruption of

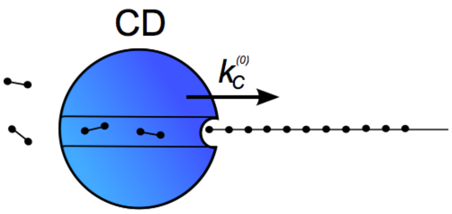

(a) Hydrolytic activity of the catalytic domain (CD) on a soluble cellulose polymer

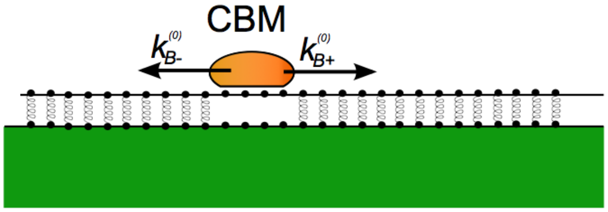

(b) Lateral diffusion of the carbohydrate binding module (CBM) on an unperturbed crystalline substrate. Springs represent noncovalent hydrogen bonds.

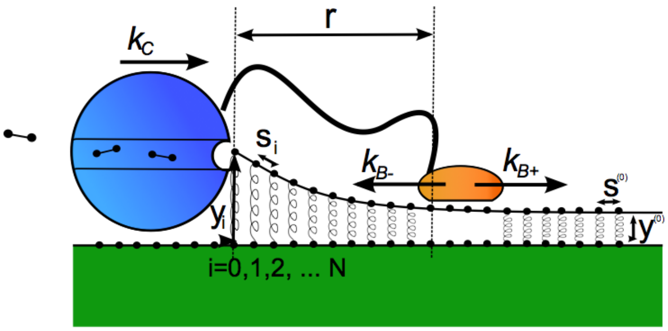

(c) Hydrolytic activity of the full cellulase, consisting of a CD and CBM coupled by a peptide linker

Figure 5.1: The cellulase enzyme

the crystalline cellulose substrate. Our results reveal that the two domains work cooperatively. In particular, as the CD hydrolyzes the cellulose polymer and advances forward, it must simultaneously extract the polysaccharide chain from the crystalline surface. This lifting, which is energetically unfavorable, significantly slows down the motion of the CD, rendering it effectively inactive without the assistance of the CBM, which disrupts the hydrogen bonds between the cellulose polymer and the crystalline surface [9–11]. At the same time, the CBM also depends on the CD's ability to lift the polymer, thus preventing it from re-associating with the crystalline surface. We find that the ability for the two domains to cooperate synergistically depends in a nontrivial way on their separation

r, which depends on the linker length and flexibility, and that there exists an optimum enzymatic rate. This observation suggests that the maximum hydrolytic activity is achieved by optimizing the cooperative action between the CD and the CBM.

5.1.2 Model

In this section, we develop a kinetic model that captures the essential features of the cellulase, while leaving out the atomistic details. Since binding to the substrate is an effectively irreversible process [12], we will study the *processive* dynamics of the two domains—represented by coupled random walkers—as they take discrete steps along the length of the cellulose polymer. Such stochastic models of molecular motor/enzyme dynamics have recently gained considerable popularity [13–19]. They require less microscopic information and can often be solved analytically.

5.1.2.1 Kinetic Scheme

We describe the state of the enzyme by the discrete position x of the CD along the cellulose polymer, and the distance r separating the two domains; see Fig. 5.1(c). We nondimensionalize these quantities using the length of a step δ, representing the distance between two neighboring monomers of the cellulose polymer. Generally speaking, for any state, three moves are allowed in the model: (1) the CD may step forward, (2) the CBM may step forward, or (3) the CBM may step backward. We denote $P(x, r, t)$ as the probability for the enzyme to be in a state described by position x and separation r at time t. Assuming a Markovian process, the master equation governing the time evolution of $P(x, r, t)$ is given by

$$\begin{aligned}\frac{dP(x,r,t)}{dt} &= k_C(r+1)P(x-1,r+1,t) + k_{B-}(r+1)P(x,r+1,t) \\ &\quad + k_{B+}(r-1)P(x,r-1,t) - [k_C(r) + k_{B+}(r) + k_{B-}(r)]P(x,r,t),\end{aligned} \tag{5.1}$$

where the positive and negative terms in the sum are the joint probabilities of transitioning into and out of, respectively, the state whose trajectory we are tracking. Note that the rate constants depend only on the relative separation of the two domains and not on the actual position, assuming translation invariance of the crystalline surface. The argument in the rate constant refers to the initial state. Thus, $k_C(r)$ is the transition probability per unit time for the CD to move to the right from a separation distance r to $r-1$, while $k_{B+}(r)$ is the transition probability per unit time for the CBM to move to the right from a separation r to $r+1$, since moving the CD to the right decreases the separation while moving the CBM to the right increases the separation. Eq. (5.1) describes a standard one-step process for a sufficiently small time step, where only one of the moves can take place [20]. In what follows we give an explicit description of the rate constants that enter into Eq. (5.1).

5.1.2.2 Two Random Walkers

Crystal structures of the catalytic domain reveal a long tunnel for the active site, containing many nonspecific and solvent-mediated interactions. This suggests a forward processive motion of the CD along the length of the cellulose polymer [21–23]; see Fig. 5.1(a). Thus, we choose to model the catalytic domain as a one-dimensional stochastic walker that may only step in the forward direction, as governed by an intrinsic rate constant $k_C^{(0)}$. Although the motion is a nonequilibrium process that likely involves complex mechanochemical dynamics, such as the conformational change of the enzyme and its grabbing and pulling of the polysaccharide chain, in the limit that the motion is tightly coupled to the hydrolysis, the intrinsic rate constant may be expressed as

$$k_C^{(0)} = \nu \mathrm{e}^{-\Delta U(g)} = \nu \mathrm{e}^{-[U(g)-U(0)]}. \tag{5.2}$$

Here ν is some transition frequency and $\Delta U(g)$ is the activation energy, in units of $k_B T$, of the intrinsic potential $U(x)$ at position g; see Fig. 5.2. Since nothing is known *a priori* about the shape of the potential, we can only say that g is some value between zero and the discrete step size δ of the model, which we nondimensionalize so that $0 < g < 1$. The assumption that the CD only steps in the forward direction is justified by imagining what must occur in order for the CD to take a reverse step: the hydrolyzed monomer must reattach to the polymer so that the CD has a track to step back on. Thus, in the absence of the CD detaching from the polymer—an unlikely event for

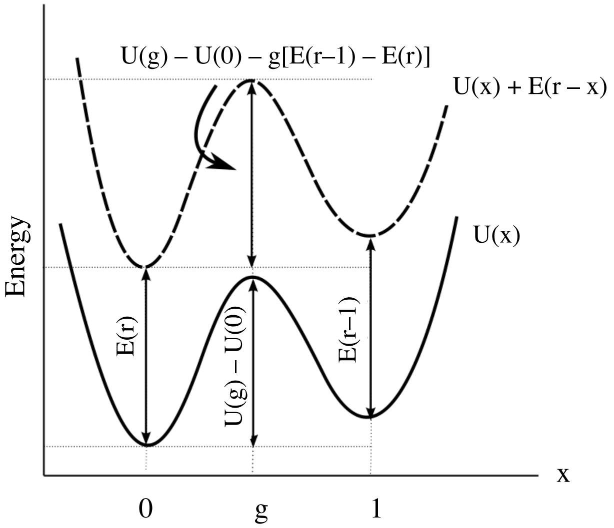

Figure 5.2: The intrinsic potential (solid) and the total potential (dashed)

the timescale of interest, considering that the enzyme binds strongly to the polymer through several hydrogen bonds [23]—the rate constant for a back step is effectively zero.

In all cases of practical interest, the cellulose polymer is bound to a crystalline surface. The presence of an active site enclosed within a tunnel requires that the CD disrupt and lift the cellulose polymer from the crystalline surface as it advances along the chain. Furthermore, there will be a compression energy for the linker, which couples the CD to the CBM. The relevant energy must therefore account for the coupling $E(r-x)$. Because the continuous form of $E(r-x)$ is not known, in particular the linker potential may depend on complex interactions with the substrate [8], we perform a linear expansion, which assumes that δ varies slowly over the length scale. The total potential may then be written

$$\begin{aligned}\tilde{U}(x) &= U(x) + E(r-x) \\ &\approx U(x) + E(r) - E'(r)x = U(x) + E(r) + \left[E(r-1) - E(r)\right]x.\end{aligned} \tag{5.3}$$

In general, the coordinates of the minima and the maxima of $\tilde{U}(x)$ will not coincide with those of $U(x)$. However, in the limit where $E(r-x)$ is a weak perturbation, we make the assumption that this is the case. Then the activation barrier of the total energy (see Fig. 5.2) is

$$\begin{aligned}\Delta\tilde{U}(g) &= U(g) + E(r-g) - [U(0) + E(r)] \\ &\approx U(g) - U(0) + [E(r-1) - E(r)]\, g\end{aligned} \tag{5.4}$$

and the rate constant for the forward motion of the catalytic domain, as biased by the lifting of the cellulose profile and the compression of the linker, becomes

$$k_C(r) = \nu \mathrm{e}^{-\Delta\tilde{U}(g)} \approx k_C^{(0)} \mathrm{e}^{-g[E(r-1)-E(r)]}, \tag{5.5}$$

where $k_C^{(0)}$ is the intrinsic rate constant given by Eq. (5.2). A similar strategy has been used by Kolomeisky and Fisher in their description of protein motors under various loading conditions [16,18] and by Betterton and Julicher in their work on helicase unwinding of DNA [14,24]. Notice that the rate constant is independent of the position x of the enzyme and is obtained for discrete values of r.

The carbohydrate binding module similarly follows a one-dimensional random walk along the length of the cellulose chain. However, its motion can be in both the forward (+) and backward (−) directions. For the diffusion of an isolated CBM on an unperturbed cellulose surface [Fig. 5.1(b)], the intrinsic rate constants are given by $k_{B+}^{(0)} = \omega \mathrm{e}^{-[U(f)-U(0)]}$ for the forward step, and $k_{B-}^{(0)} = \omega \mathrm{e}^{-[U(f)-U(1)]}$ for the backward step. As before, ω is some transition frequency ($\omega \neq \nu$) and f is the position of the activation barrier. Because the intrinsic dynamics of the CBM is unbiased, we set $U(0) = U(1)$ and $f = 1/2$, corresponding to a symmetric periodic potential, so that $k_{B+}^{(0)} = k_{B-}^{(0)}$. In the case where the CBM is connected to the CD, the peptide linker and the profile of the perturbed cellulose surface will bias the diffusion of the CBM; see Fig. 5.1(c). To capture these effects, we follow the same procedure as for the CD and obtain

$$k_{B+}(r) = k_{B+}^{(0)} \mathrm{e}^{-f[E(r+1)-E(r)]} = k_{B+}^{(0)} \mathrm{e}^{-\frac{1}{2}[E(r+1)-E(r)]} \tag{5.6}$$

for the forward rate constant, and

$$k_{B-}(r+1) = k_{B-}^{(0)} \mathrm{e}^{-(1-f)[E(r)-E(r+1)]} = k_{B-}^{(0)} \mathrm{e}^{-\frac{1}{2}[E(r)-E(r+1)]} \tag{5.7}$$

for the reverse rate constant. Note that $k_{B+}(r)/k_{B-}(r+1)$ satisfies the detailed balance requirement and is independent of the parameter f.

The master equation [Eq. (5.1)] and rate constants [Eq. (5.5)–Eq. (5.7)] completely describe the kinetics of our system. Before we proceed with obtaining explicit expressions for the rate constants, we point out two additional features of the model. Firstly, the CBM is always in front of the CD and the two cannot cross; if $r = 0$, only the CBM may step forward. To account for this blockage effect, we set $k_C(0) = k_{B-}(0) = 0$. Secondly, in the limit where the coupling includes an infinitely stiff spring, the CD and the CBM are forced to move as one unit. In the weak coupling case assumed here, the activation barrier for such a concerted move is roughly the sum of the activation barriers for the CD and the CBM. Therefore, the rate constant for such a process is much smaller than the rate constants for the individual moves allowed in the master equation. Together with the fact that Eq. (5.1) only allows for one-step processes, we ignore the higher-order event of joint moves by the CD and CBM.

In the next section, we obtain an explicit expression for the coupling potential $E(r)$, defined as the sum of the energy from the peptide linker $L(r)$ and the energy from the cellulose profile $H(r)$.

5.1.2.3 Coupling Potential

Because no satisfactory end-to-end probability distribution of the peptide linker can be found in the literature [4, 5, 8, 25], we choose to model the linker as a simple Hookean spring. This assumption is justified by the glycosylation and the high fraction of proline-threonine residues, both of which impart a high rigidity to the linker, leading to extended conformations in solution [5]. The energy of the linker as a function of the separation r is the familiar

$$L(r) = \frac{\kappa}{2}(r - r_0)^2. \tag{5.8}$$

Here κ is the spring constant representing the stiffness of the linker and r_0 is some equilibrium length in units of δ. In what follows, we only consider cases where $r_0 \neq 0$. The structure of the linker region varies widely among cellulases, anywhere from 5 to 100 residues in length [26] and an average of 3.0 to 0.7 Å/residue [4], depending on flexibility. We vary the length and the flexibility of the linker and examine their effects on the hydrolysis kinetics.

Next, we obtain $H(r)$ for the energy of the cellulose profile. Lignocellulose is a complex substrate composed primarily of cellulose microfibrils in association with hemicellulose and surrounded by a lignin seal. This makes modeling the enzymatic hydrolysis difficult without first noting that several pretreatment options exist, which can break the lignin seal and solubilize the amorphous hemicellulose, thus releasing the cellulose microfibril [27]. Furthermore, electron microscopy results indicate worn *edges* of the cellulose microfibril, suggesting that the enzyme preferentially binds to and processively hydrolyzes the most exposed chain on the surface, i.e., that with the fewest interactions to the underlying crystal [28]. Thus it is reasonable to simplify the substrate into a one-dimensional homopolymer that is bound to a surface through several noncovalent interactions.

To represent the cellulose polymer attached to the crystalline substrate, we adopt the Peyrard-Bishop potential used for the unzipping of two DNA strands [29]:

$$H = \sum_{i=0}^{N-1} \frac{1}{2}\lambda(s_i - s^{(0)})^2 + \sum_{i=0}^{N} \left\{ d\left(1 - \exp[-a(y_i - y^{(0)})]\right)^2 - d \right\}. \tag{5.9}$$

Here the summation is over the monomers of the cellulose chain and we keep track of $i = 0, 1, \ldots, N$ monomers, where 0 is always the monomer at the entrance of the tunnel, and N is taken to be sufficiently large as to be in the unperturbed region of the cellulose crystal; see Fig. 5.1(c). The first term represents the penalty for stretching the covalent bonds between the glucose monomers, where λ is the effective spring constant of the covalent bond, $s^{(0)} = \delta$ is the equilibrium bond length, and s_i is the bond length between monomers i and $i+1$:

$$s_i = \sqrt{(y_i - y_{i+1})^2 + (s^{(0)})^2}. \tag{5.10}$$

Here, y_i is the height of the i^{th} monomer from the surface. For small $y_i - y_{i+1}$, the first term in Eq. (5.9) can be approximated so that the sum becomes

$$H = \frac{\gamma}{8}\sum_{i=0}^{N-1}(y_i - y_{i+1})^4 + \sum_{i=0}^{N}\left\{d\left(1 - \exp[-a(y_i - y^{(0)})]\right)^2 - d\right\}, \tag{5.11}$$

with $\gamma \equiv \lambda/(s^{(0)})^2$. The second term is the Morse potential for the hydrogen bond interactions between the monomers of the chain to be extracted and the surface, where $y^{(0)}$ is the equilibrium bond length, d is the bond dissociation energy, and a determines the width of the potential well. Because each monomer is actually involved in several hydrogen bonds and we only model a single interaction, each term of the Morse potential actually represents an approximation of all the non-covalent interactions. In what follows, we refer to this as a single hydrogen bond for simplicity. The local disruptive effect of the CBM on the crystal is captured by rewriting the second sum so that the interaction energy for the monomers directly below the CBM, $i = \{r, \ldots, r + n_B\}$, are not included. n_B reflects both the size of the binding module and the number of monomers disrupted. For example, $n_B = 4$ in Fig. 5.1(c). Thus, we can rewrite Eq. (5.11) as

$$H = \frac{\gamma}{8}\sum_{i=0}^{N-1}(y_i - y_{i+1})^4 + \sum_{\substack{i=0 \\ i\notin\{r,\ldots,r+n_B\}}}^{N}\left\{d\left(1 - \exp[-a(y_i - y^{(0)})]\right)^2 - d\right\}. \tag{5.12}$$

In this expression, the dependence on r enters through the second sum. Minimizing the energy with respect to $\{y_i\}$, subject to the boundary conditions that $y_{i=0} = y_h$ (the height the chain must be lifted to enter the catalytic domain tunnel) and $y_{i=N} = y^{(0)}$ (the equilibrium bond length in the unperturbed region of the crystal), we obtain, for each discrete value of r, the profile $\{y_i^r\} = \{y_0^r, y_1^r\, y_2^r\, \ldots, y_\infty^r\} = \{y_h, y_1^r\, y_2^r\, \ldots, y^{(0)}\}$ and its corresponding potential $H(r)$.

In Fig. 5.3, we plot the coupling potential $E(r) = H(r) + L(r)$. The dashed line depicts the cellulose profile potential $H(r)$ determined by minimizing Eq. (5.12) with the following choice of parameters: $y^{(0)} = 0.4$, $y_h = 1.0$, $d = 12.89$, $a = 9.0$, and $\gamma = 33843.4$. The zero of energy is set relative to the unperturbed state of the cellulose crystal so that disrupting the surface by lifting the chain and/or breaking hydrogen bonds results in a positive energy. Because the monomers near

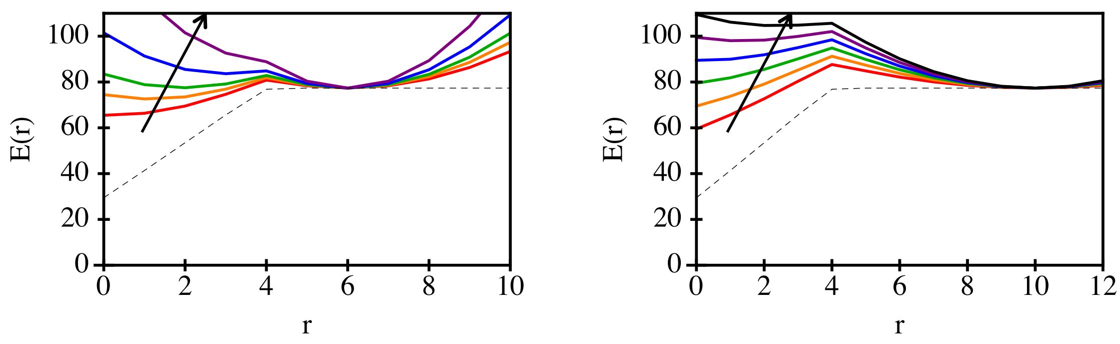

(a) $r_0 = 6$ and $\kappa = 2.0, 2.5, 3.0, 4.0, 6.0$ (b) $r_0 = 10$ and $\kappa = 0.6, 0.8, 1.0, 1.2, 1.4, 1.6$

Figure 5.3: The coupling potential. Arrow indicates direction of increasing κ.

the CD are lifted from the crystalline surface, their hydrogen bonds are highly stretched, perhaps even broken, according to the description given by the Morse potential. Thus, when the separation r is small, the bond disruption property of the CBM has little or no effect on the total energy of the cellulose profile. As r increases, the CBM is forced to break bonds that are increasingly more favorable to be intact, and eventually bonds that are in the unperturbed region of the crystal. For our parameters, this is achieved when $r = 4$, which we call r^*. For $r > r^*$, $H(r)$ is independent of r. As shown in Fig. 5.3 for two different initial linker lengths, $E(r)$ has a nontrivial dependence on both the linker length r_0 and the linker stiffness κ. In particular, $E(r)$ is bistable in a certain range of r_0 and κ. In the results section, we will discuss the implications of this observation.

5.1.3 Results

The key quantity of interest in developing more efficient enzymes is the net hydrolysis rate on the crystalline cellulose, which in our model is given by the mean velocity at steady state. To better understand the structure/function relationship of the linker, it is further useful to consider the mean separation between the CD and the CBM. We begin by discussing these two quantities, and their dependence on the properties of the linker. We follow this with a description of the fluctuation, which is informative in understanding the transition between the compressed and the extended conformations of the linker.

The mean separation of the two domains is given by the probability-weighted sum

$$\langle r\rangle = \sum_{r=0} r P_{ss}(r), \tag{5.13}$$

where $P_{ss}(r)$ is the steady-state probability of finding the enzyme in a state defined by the separation r. The mean velocity of the cellulase is similarly given by

$$\langle v\rangle = \langle v_C\rangle = \sum_{r=0} k_C(r) P_{ss}(r), \tag{5.14}$$

where we have used the fact that the mean velocity of the CD equals that of the enzyme and the velocity is related to the rate constant by $v_C(r) = k_C(r)$ when the velocity is given in number of steps δ per unit time. The dispersion around the mean velocity defines the effective diffusion coefficient and is given by [24]

$$D = \frac{1}{4} \sum_{r=0} \left[k_C(r) + k_{B+}(r) + k_{B-}(r)\right] P_{ss}(r). \tag{5.15}$$

To obtain the steady-state probabilities, we note that the stationary distribution corresponds to a constant probability flux, i.e., $dP_{ss}(r)/dt = 0$, where we have dropped the x and t dependence from Eq. (5.1). Beginning from $r = 0$, we can write

$$\frac{dP_{ss}(0)}{dt} = 0 = k_{B+}(0) P_{ss}(0) - \left[k_{B-}(1) + k_C(1)\right] P_{ss}(1), \tag{5.16}$$

from which, generalizing for any r, we obtain the following recursion relation [24]

$$P_{ss}(r+1) = \frac{k_{B+}(r)}{k_{B-}(r+1) + k_C(r+1)} P_{ss}(r). \tag{5.17}$$

Following the proper normalization, Eq. (5.17) is used to generate the steady-state probability distribution of the enzyme during the hydrolysis.

Having obtained expressions for the steady-state behavior of the hydrolysis, we next compute the mean separation $\langle r\rangle$ and the mean velocity $\langle v\rangle$ for a cellulase with an equilibrium linker length

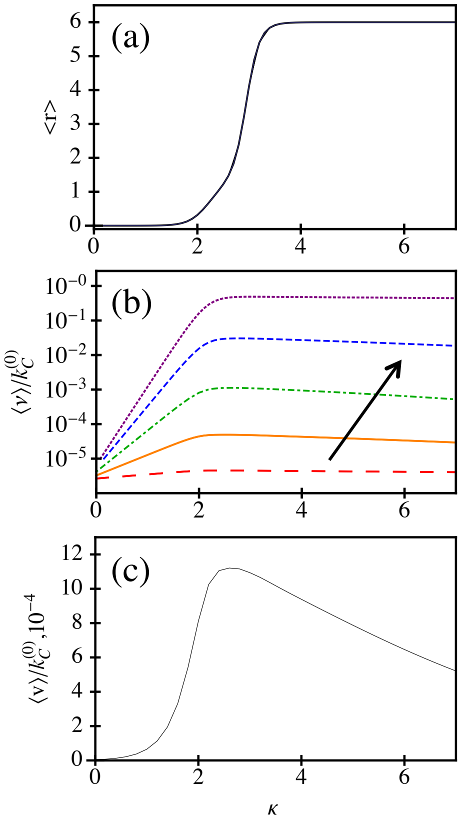

Figure 5.4: For $r_0 = 6$, $k_C^{(0)}/k_B^{(0)} = 0.1$: (a) $\langle r \rangle$ for a range of values of the parameter g, where all curves coincide. (b) logarithmic plot of $\langle v \rangle / k_C^{(0)}$ for $g = 0.05, 0.25, 0.50, 0.75, 0.95$. Arrow indicates direction of increasing g. (c) linear plot of $\langle v \rangle / k_C^{(0)}$ for $g = 0.50$.

$r_0 = 6$. From the experiments, which show that the diffusion of the CBM does not appear to hinder the hydrolysis [30], we set $k_C^{(0)} = 10s^{-1}$ and $k_{B\pm}^{(0)} = 100s^{-1}$ based on the simple requirement that the intrinsic rate constants satisfy $k_C^{(0)} < k_{B\pm}^{(0)}$. The persistence length l_p of a polyproline peptide sequence [31] has been estimated to be ~ 44 Å, which is on the order of the contour length of the peptide linker. Therefore, the linker can be viewed as an elastic rod of length r_0. Relating the bending energy to the spring energy and taking the step length δ to be 5Å, we estimate $\kappa^{\max} \sim 7$. In what follows, we only consider the cases for $0 \le \kappa \le \kappa^{\max}$.

As shown in Fig. 5.4(a), the mean separation increases monotonically with κ and is insensitive to the parameter g of the activation barrier for the CD (the curves for 5 different values of g coincide with each other). However, the mean velocity depends strongly on g, through the rate constant $k_C(r)$ in Eq. (5.14), as shown in Fig. 5.4(b). In particular, the maximum attainable $\langle v \rangle$ increases

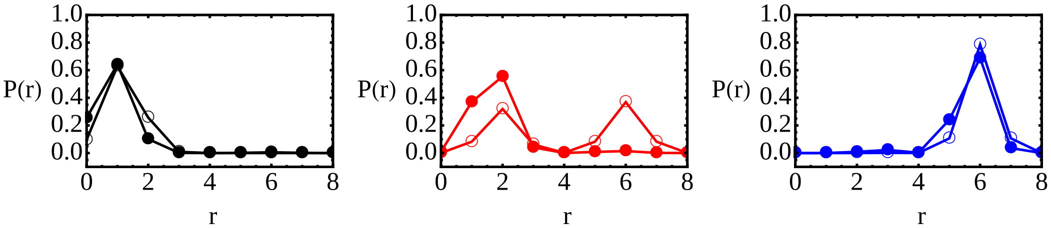

Figure 5.5: Probability distribution of the separation r for $r_0 = 6$ and $\kappa = 2.5, 3.0, 4.0$ (L–R). Empty markers correspond to $k_C^{(0)}/k_B^{(0)} = 0.1$ and filled markers correspond to $k_C^{(0)}/k_B^{(0)} = 1000$.

with g. Furthermore, $\langle v \rangle$ depends nonmonotonically on the stiffness of the linker, as shown more clearly on the linear scale plot in Fig. 5.4(c) for $g = 0.5$. In all cases, the peak in velocity occurs during the transition from the compressed to the extended conformation of the cellulase as depicted by the corresponding plot in Fig. 5.4(a) of the average separation. The origin of the transition can be understood if one considers the two components of the coupling potential $E(r)$. In Fig. 5.3(a), we show that as the stiffness is increased the linker begins to dominate the coupling potential so that the minimum in energy shifts from $r = 0$ (for $\kappa < 2$) to $r = r_0$ (for $\kappa > 4$), with a double well potential occurring for $\kappa \sim 3$. This corresponds to a doubly peaked steady-state probability distribution $P_{ss}(r)$, as shown in Fig. 5.5. We note that a dynamic transition in the separation distance between two domains has also been observed for two motor proteins coupled by a linear potential [32]. However, in that case the transition is a result of the balance between energetic and rate effects, whereas here the transition is driven primarily by the energetics of the coupling potential.

The double well feature of the energy function and the shift of the (global) energy minimum from one value of the separation r to another as the stiffness changes are reminiscent of first-order phase transitions in thermodynamics. However, because of the small number of degrees of freedom in the current problem, no true discontinuous transitions take place; only the relative weights of the two peaks change. The maximum mean velocity is obtained when the two peaks are of roughly equal weights. Because of the finite barrier that separates the two energy minima, the dynamics of the system is one where the system fluctuates between the two values of the separation, with some characteristic lifetime around each. To directly observe this feature, we have performed kinetic Monte

Carlo simulations, which produce the time evolution of a process when the rates are known [33–35]. Fig. 5.6(c) shows that the system jumps between $r = 2$ and $r = 6$ for the transition at $\kappa = 3.0$, which also corresponds to the peak of the mean velocity. If we compare this trajectory to Fig. 5.6(d) for $\kappa = 1.0$, we see that the fluctuation of the system is considerably greater at the transition. As another measure of the fluctuation, we plot the variance of the separation

$$\sigma^2 = \sum_r (r - \langle r \rangle)^2 P_{ss}(r), \tag{5.18}$$

from which we observe a strong peak at the transition; see Fig. 5.6(a). The large fluctuation is also manifested in a maximum for the diffusion coefficient; see Fig. 5.6(b). Together, these results suggest that the fluctuation is at a maximum during the transition from a compressed to a more extended conformation of the linker, where the maximum mean velocity is obtained. The ability to adopt different separations between the two domains is what gives rise to the positive synergy between the two domains, i.e., the CD helps lift the polysaccharide chain from the crystalline surface as it hydrolyzes the polymer (which is more easily accomplished at the shorter separation) while the CBM disrupts the hydrogen bonds between the polymer and the crystalline surface (which is more effectively achieved at a larger separation).

We next consider how the system behavior depends upon the intrinsic rate constants, $k_C^{(0)}$ and $k_B^{(0)}$, as these are the parameters that protein engineering aims to alter. Using the rate constants obtained in Eq. (5.5)–Eq. (5.7), Eq. (5.17) can be rewritten in the form

$$P_{ss}(r+1) = \frac{k_{B+}^{(0)} e^{-\frac{1}{2}[E(r+1)-E(r)]}}{k_{B-}^{(0)} e^{-\frac{1}{2}[E(r)-E(r+1)]} + k_C^{(0)} e^{-g[E(r)-E(r+1)]}} P_{ss}(r). \tag{5.19}$$

As before, if we assume $k_{B+}^{(0)} = k_{B-}^{(0)}$, then

$$P_{ss}(r+1) = \frac{e^{-[E(r+1)-E(r)]}}{1 + \frac{k_C^{(0)}}{k_B^{(0)}} e^{-(1/2-g)[E(r+1)-E(r)]}} P_{ss}(r). \tag{5.20}$$

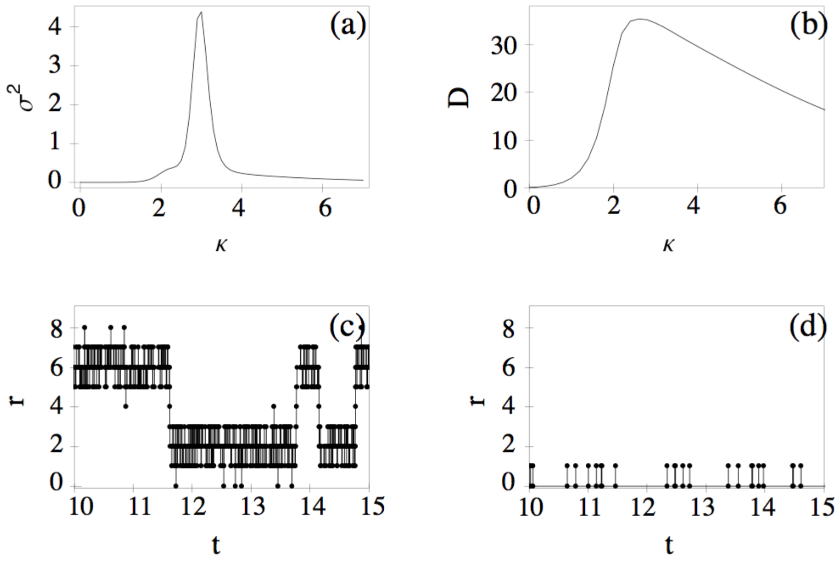

Figure 5.6: (a) and (b): The variance of $\langle r \rangle$ and the effective diffusion constant D as a function of the linker stiffness κ. (c) and (d): Separation r as a function of simulation time generated using the kinetic Monte Carlo algorithm for $\kappa = 3.0$ and $\kappa = 1.0$, respectively

Setting $f = g = 1/2$, Eq. (5.20) can be further simplified to the form

$$P_{ss}(r+1) = \frac{e^{-[E(r+1)-E(r)]}}{1 + \frac{k_C^{(0)}}{k_B^{(0)}}} P_{ss}(r). \tag{5.21}$$

This recursion equation can be easily solved to yield

$$P_{ss}(r) = \frac{1}{Q} \frac{e^{-[E(r)-E(0)]}}{\left(1 + \frac{k_C^{(0)}}{k_B^{(0)}}\right)^r} = \frac{1}{Q} \exp\left[-E(r) - r\ln\left(1 + \frac{k_C^{(0)}}{k_B^{(0)}}\right)\right], \tag{5.22}$$

where Q is a normalization factor given by

$$Q = \sum_{r=0}^{\infty} \exp\left[-E(r) - r\ln\left(1 + \frac{k_C^{(0)}}{k_B^{(0)}}\right)\right]. \tag{5.23}$$

For an immobile enzyme in which $k_C^{(0)} = 0$, Eq. (5.22) produces the Boltzmann distribution. For nonvanishing $k_C^{(0)}$, $P_{ss}(r)$ remains close to the equilibrium distribution as long as $k_C^{(0)}/k_B^{(0)} < 1$, as shown in Fig. 5.5, for the parameters $k_C^{(0)} = 10$ and $k_B^{(0)} = 100$ (empty markers). As this ratio increases, the probability distribution begins to favor smaller values of r (solid markers)—as

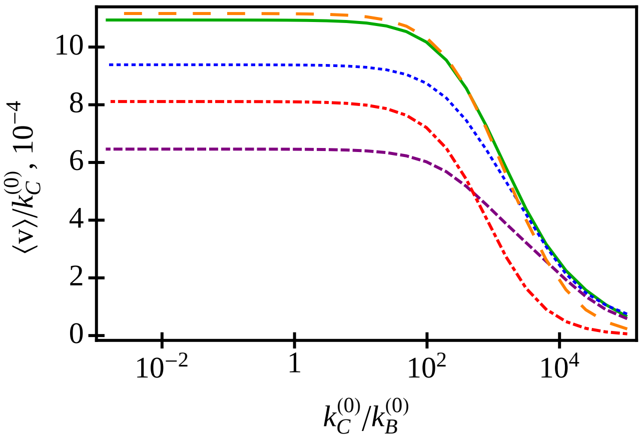

Figure 5.7: The nondimensionalized velocity, as a function of $k_C^{(0)}/k_B^{(0)}$, for $r_0 = 6$ and κ= 2 (red, dot-dashed), 2.5 (orange, long-dashed), 3 (green, solid), 4 (blue, dotted), 6 (purple, dashed)

compared with the equilibrium distribution—because the CD advances faster than the CBM can diffuse back to equilibrium, forcing the linker into a more compressed conformation. In the limit where $k_C^{(0)}/k_B^{(0)} \to \infty$, the two domains are adjacent to each other and the CBM blocks the hydrolysis of the CD.

To better understand the dependence of the average velocity on the ratio of the intrinsic rate constants, we plot the nondimensionalized velocity, $\langle v\rangle/k_C^{(0)}$, as a function of $k_C^{(0)}/k_B^{(0)}$; see Fig. 5.7. The nondimensionalized velocity remains essentially constant up to $k_C^{(0)}/k_B^{(0)} \sim 100$, implying that the velocity is linearly proportional to the intrinsic rate constant $k_C^{(0)}$ in this regime. Note that the plateau (maximum) values of $\langle v\rangle/k_C^{(0)}$ for the curves in Fig. 5.7 show the same nonmonotonic dependence on κ. We also see that the blockage effect at large $k_C^{(0)}/k_B^{(0)}$ is greater for flexible linkers ($\kappa = 2$) where the decay to $\langle v\rangle/k_C^{(0)} = 0$ occurs more rapidly than for rigid linkers ($\kappa = 6$). We note that the un-scaled velocity does not decay to zero, but reaches a plateau in the limit of large $k_C^{(0)}/k_B^{(0)}$. In the biological regime, $k_C^{(0)}/k_B^{(0)} << 1$ [30]. This suggests that engineering more efficient catalytic domains, without having to consider the binding module, can already provide significant gains in improving the overall efficiency of the enzymatic hydrolysis. In this regime, increasing $k_C^{(0)}$ leads to a linear increase in $\langle v\rangle$ through Eq. (5.14).

Lastly, we examine the effect of the linker length on the hydrolysis. As can be seen in Fig. 5.3,

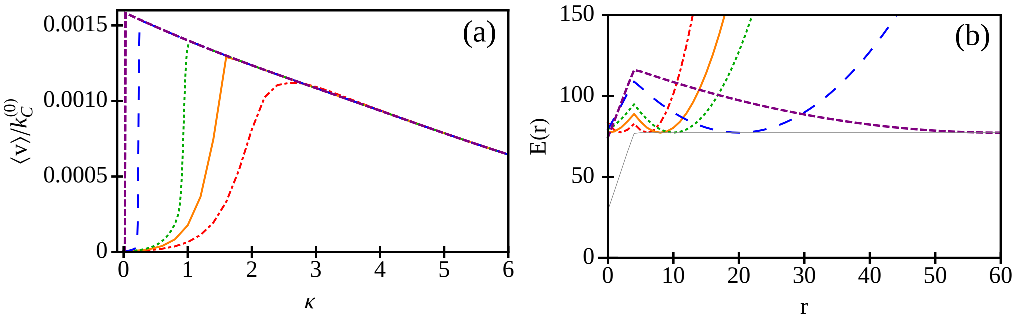

Figure 5.8: (a) Nondimensionalized velocity $\langle v\rangle/k_C^{(0)}$ as a function of the linker stiffness κ, for $r_0 = 60$ (purple, dashed), 20 (blue, long-dashed), 10 (green, dotted), 8 (orange, solid), 6 (red, dot-dashed). (b) The coupling potential $E(r)$, corresponding to the κ that maximizes $\langle v\rangle/k_C^{(0)}$ for the respective values of r_0 given in (a)

the coupling potential $E(r)$ of the longer linker ($r_0 = 10$) shows a marked difference from that of the shorter linker ($r_0 = 6$). Rather than a double well potential arising as κ is increased, the position of the minimum jumps from $r = 0$ to $r = r_0$, which is analogous to a phase transition from the compact to extended conformation. As shown in Fig. 5.8(a), this corresponds to a sharp turn of the slope at the peak of $\langle v\rangle$ (dotted line) rather than a smooth slope (dot-dashed line). We note that because of the finite number of degrees of freedom, there is no singularity in the system, but rather what appears to be a cusp in the scale of the figure. Secondly, there is a clear trend that longer linkers are able to reach higher $\langle v\rangle_{\max}$. To understand this, recall that the maximum velocity is obtained when the separation between the CD and the CBM is free to fluctuate. This requires that the force be small, or equivalently, the slope of the composite potential be relatively flat; see Fig. 5.8(b). The spring constant should be just enough so that $L(r)$ can counterbalance the effect of the fairly deep minimum at $r = 0$ in $H(r)$. Too soft of a linker, and the enzyme will get stuck in the compact conformation; too stiff of a linker, and the enzyme will be trapped at $r = r_0$. The linker functions to provide the separation necessary to get the CBM out of the range of influence of $H(r)$, where larger values of r_0 will need smaller values of κ. However, for $r_0 >> r^*$, where r^* is the range of influence of the potential $H(r)$, additional increase in the linker length will not provide more gains in increasing the efficiency of the hydrolysis. As shown in Fig. 5.8(a), the maximum in $\langle v\rangle$ approaches a limit of roughly $0.0016k_C^{(0)}$. This limit is nearly attained with the linker length so that there is little benefit for increasing the linker length beyond 20.

5.1.4 Conclusion

We have developed a kinetic, mesoscopic model for cellulase, using two random walkers whose dynamics are coupled by the peptide linker and the cellulose polymer. The role of the linker in the hydrolysis has been a topic of considerable controversy. Our results show that the composite potential due to the peptide linker and the cellulose polymer can give rise to a bimodal distribution for the separation of the CD and CBM. Furthermore, the optimal hydrolysis rate is obtained at the transition from a compressed to an extended conformation. At this transition, the system exhibits maximum fluctuation as measured by the variance of the separation distance between the two domains and the dispersion around the mean procession velocity. For a given linker length, the mean velocity shows a nonmonotonic dependence on the stiffness of the linker, with a peak at some intermediate stiffness value. We also find that the optimal stiffness value decreases and that the maximum hydrolysis rate increases with increasing linker length.

Our study provides useful mechanistic insight to the action of the cellulase complex, as the CD and CBM domains cooperate to extract and hydrolyze a single cellulose polymer from the recalcitrant biomass. The results of this work can be useful for the design and engineering of more efficient enzymes. For example, within the range of experimentally known values of the parameters of our model, improving the intrinsic hydrolytic activity of the CD can serve to make significant gains in the overall efficiency of the enzyme, without having to alter the CBM. However, our results also suggest the importance of optimizing the linker length and stiffness, an insight that would not be obvious without the help of a model.

We thank Bradley Olsen, Frances Arnold, and Pete Heinzelman for helpful discussions. C.L.T. appreciates financial support from an NIH training grant.

5.2 Thermodynamic Basis for the Genome-to-Capsid Charge Relationship in Viral Encapsidation

We establish an appropriate thermodynamic framework for determining the optimal genome length in electrostatically driven viral encapsidation. Importantly, our analysis includes the electrostatic potential due to the Donnan equilibrium, which arises from the semipermeable nature of the viral capsid, i.e., permeable to small mobile ions but impermeable to charged macromolecules. Because most macromolecules in the cellular milieu are negatively charged, the Donnan potential provides an additional driving force for genome encapsidation. In contrast to previous theoretical studies, we find that the optimal genome length is the result of combined effects from the electrostatic interactions of all charged species, the excluded volume, and, to a very significant degree, the Donnan potential. In particular, the Donnan potential is essential for obtaining negatively overcharged viruses. The prevalence of overcharged viruses in Nature may suggest an evolutionary preference for viruses to increase the amount of genome packaged by utilizing the Donnan potential (through increases in the capsid radius), rather than high charges on the capsid, so that structural stability of the capsid is maintained [36].

5.2.1 Introduction

The most prevalent viruses in Nature are single-stranded RNA viruses with the genetic material enclosed in icosahedral-shaped capsids made up of 60T protein units, where the T-number is a small integer index. The protein units (capsomers) often contain highly basic peptide arms that extend into the capsid interior and, under physiological conditions, are positively charged. Electrostatic attraction provides the driving force for encapsidating the negatively charged RNA, which, in turn, helps to overcome the electrostatic repulsion among the capsomers during the capsid assembly.

In a series of classic experiments, Bancroft et al. [37, 38] demonstrated that certain viruses can encapsidate nonnative RNA and even generic polyanions. Dominance of the electrostatics as the driving force for viral assembly has led to the expectation of a simple relationship between the total capsid charge Q_P and the genome charge Q_R, as every nucleotide carries one unit of negative charge. Belyi and Muthukumar [39] compiled data for 19 wild-type viruses from several viral families and found an apparent "universal" charge ratio of $Q_R/Q_P \approx 1.6$, which they explained by combining the ground-state dominance approximation for polyelectrolyte binding to an oppositely charged polymer brush with the Manning condensation theory [40]. The former predicts a 1:1 charge ratio and the latter is used as a qualitative argument for the actual charge on the RNA being less than the nominal charge. Hu et al. [41], however, assumed that the RNA winds around individual peptide arms and found that the viruses are most stable when the total contour length of the RNA is close to the total length of the peptide arms; this roughly gives a charge ratio of 2. In other works that ignore the peptide arms completely, there is additional disagreement for the charge ratio. For example, van der Schoot and Bruinsma [42] obtained a charge ratio of 2, whereas the work of Angelescu et al. [43] yielded a ratio of 1 as the most favorable condition (but predicted that encapsidation can remain favorable up to a ratio of 3.5). Implicit in any expected relationship between the total capsid charge Q_P and the genome charge Q_R is the assumption that at a given Q_P, there exists an optimal genome length N^* that can be encapsidated. However, the definition of N^* has not been clearly articulated in the literature, and the issue of a "universal" charge ratio remains unresolved.

In this chapter, we first clarify the meaning of an optimal genome length N^*. This requires a clearly defined thermodynamic setup from which minimization of an appropriate free energy can emerge in a way that is consistent with the assembly mechanism under typical in vitro or in vivo conditions. We then use self-consistent field (SCF) theory [44] to calculate the free energy required to determine N^*. We find that N^* is not uniquely determined by the total charge of the capsid Q_P, but depends on the placement of the capsid charges, the excluded volume effects and, most significantly, the negative electrostatic potential outside the viral capsid. This Donnan potential [45] has been neglected in all previous theoretical and computational studies. We find that this contribution is essential for obtaining overcharged viruses.

By including the Donnan potential, we are able to vary the parameters in our model—the charge density and length of the peptide arms, and the charge density and radius of the capsid shell—

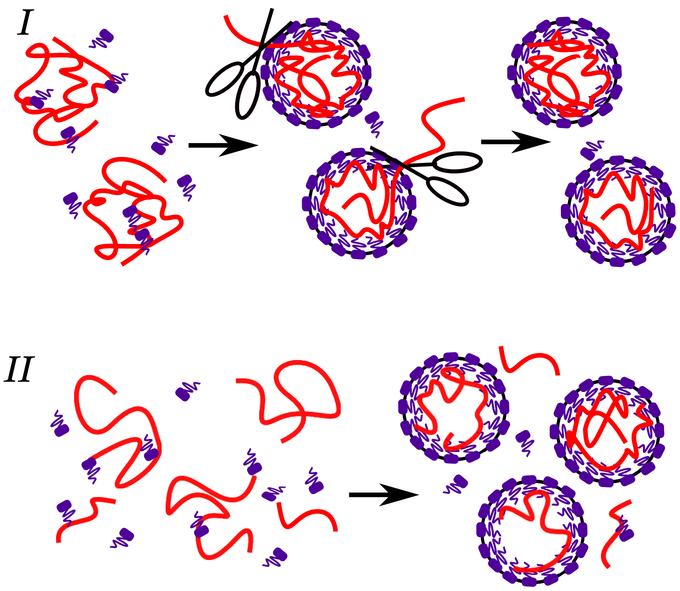

Figure 5.9: Two scenarios for viral assembly giving rise to an optimal genome length. Scenario I: a monodisperse solution of RNA of length $N_0 > N^*$, where the optimal length N^* corresponds to the largest population of viral particles containing N^* segments inside the capsid. Here, the outside fragment of RNA can be removed by nucleases, as represented by scissors. Scenario II: a polydisperse solution of RNA, where viruses containing fully encapsidated molecules of length N^* dominate the population of singly encapsidated viral particles

to generate a set of hypothetical viruses for which the genome-to-capsid charge ratio behavior of the genome length vs. the total capsid charge resembles data on real overcharged viruses from Ref. [39]. On the basis of our analysis, the prevalence of overcharged viruses in Nature may suggest an evolutionary preference for viruses that primarily utilize the Donnan potential, rather than highly charged capsomers, to increase the amount of genome packaged, while still maintaining the structural stability of the capsid shell.

5.2.2 Clarification of the Optimal Genome Length

Bancroft et al. [38] showed that viral assembly occurs by a nucleation and growth mechanism, with the RNA acting as the nucleating agent. If the RNA are sufficiently large, and on account of their electrostatic repulsion with each other, the likelihood of multiple RNA nucleating one capsid is low and, for the optimal length question, we may confine ourselves to the population of single RNA-encapsidated viral particles. Also, following previous theoretical works [39, 41–43, 46–51], we treat the RNA as a linear polyelectrolyte, and ignore the secondary structures [52]. This is in part a computational necessity and in part guided by the motivation to elucidate the generic features of electrostatically driven viral assembly by using simple models. It will be shown that changing the polyelectrolyte from a linear chain to a multi-armed star considerably reduces its physical dimension, one of the main effects of the secondary structure, but has little effect on the results. As depicted in Fig. 5.9, we consider two scenarios for the encapsidation. Under reasonable conditions, these two scenarios yield identical results.

5.2.2.1 Scenario I

Consider a monodisperse solution of sufficiently long RNA ($N_0 > N^*$) mixed with capsomers. Upon nucleation around the RNA, the capsomers aggregate to form viruses of various T-number sizes with N segments inside and $N_0 - N$ segments outside. It has been suggested that the outside fragments can be removed by nucleases [53, 54]. We focus on the subpopulation of singly encapsidated viral particles of a *particular* T-number. Treating viral assembly as an equilibrium system subject to the laws of mass action (see [42] and references therein), the number concentration of viral capsids containing a genome length N inside is

$$C(N) = C^{ref} \exp\left[-f(N) - \Delta f_{cap} + \mu + 60T\lambda\right]. \tag{5.24}$$

Here $f(N)$ is the free energy of interaction between the RNA and the capsid, Δf_{cap} is the free energy of formation for an empty capsid, μ and λ are the chemical potentials of the free RNA and the free capsomers, respectively, and C^{ref} is a reference concentration that is assumed to be independent of N. $f(N)$ and Δf_{cap} are really semi-grand free energies, as the capsid is open with respect to small salt ions and solvent. However, for notational conciseness, we do not explicitly include the chemical potentials of these species in the expression. Throughout this work, we take the thermal energy k_BT as the energy unit. Clearly, the fraction of viral particles with N segments inside is given by

$$P(N) = \frac{\exp\left[-f(N)\right]}{\sum_{N'} \exp\left[-f(N')\right]}, \tag{5.25}$$

where the summation runs from N_{min}, as required to nucleate the capsid [38], to N_0. Importantly, the free energy of formation of the capsid and the concentrations of RNA and capsomers, while determining the concentration of the viral particles, play no role in $P(N)$. If we ignore the connectivity between the inside and outside portions of the RNA, then the free energy of interaction may be separated into $f(N) = f_{in}(N) + f_{out}(N_0 - N)$. The main contribution to f_{out} arises from the external osmotic pressure Π and the finite electrostatic potential difference $\Delta\psi$, i.e., the Donnan potential. The former is due to the presence of other macromolecules, such as proteins and nucleic acids or added osmolytes [55], and the latter due to the fact that these macromolecules are usually charged. Thus, we have

$$f_{out}(N_0 - N) = (N_0 - N)(v_R \Pi + e\Delta\psi), \tag{5.26}$$

where v_R is the monomer volume of a nucleotide and e is the elementary charge. Under usual solution conditions, $v_R \Pi << kT$ so that we can safely ignore the osmotic pressure term. Substituting the free energy back into $P(N)$, we get

$$P(N) = \frac{\exp[-g(N)]}{\sum_{N'} \exp[-g(N')]}, \tag{5.27}$$

where $g(N) = f_{in}(N) - eN\Delta\psi$. It is now clear that the largest population corresponds to the minimum of this free energy.

5.2.2.2 Scenario II

We envision a polydisperse solution of RNA mixed with capsomers. Once packaged we assume that the RNA molecules reside entirely within the viral capsid. Again, we focus on the subpopulation of singly encapsidated viral particles of a particular T-number. Following arguments similar to those in Scenario I, the fraction of viral particles with chain length N is given by

$$P(N) = \frac{\exp[-f_{in}(N) + \mu_N]}{\sum_{N'} \exp[-f_{in}(N') + \mu_{N'}]}. \tag{5.28}$$

Here μ_N is the chemical potential of free RNA of length N. Assuming ideal solution behavior for the free RNA,

$$\mu_N = \mu_N^{ref} + \log(\rho_N/\rho_N^{ref}) + eN\Delta\psi, \tag{5.29}$$

where ρ_N^{ref} is a reference concentration and μ_N^{ref} is its respective chemical potential. These reference terms contain contributions from the momentum and conformation integration of the reference Gaussian chain and exactly cancel those in f_{in}. The distribution then becomes

$$P(N) = \frac{\rho_N \exp[-f_{in}(N) + eN\Delta\psi]}{\sum_{N'} \rho_{N'} \exp[-f_{in}(N') + eN'\Delta\psi]}. \tag{5.30}$$

When the concentrations of RNA with different chain lengths are the same, the ρ_N exactly cancel and Eq. (5.30) becomes identical to Eq. (5.27). In fact, because the free energy in the exponential is $O(N)$ (see Fig. 5.10), its contribution will dominate the distribution and the concentration prefactors can be safely ignored. Therefore, for all practical purposes, the determination of N^* is again a minimization of the free energy, $g(N)$.

We note that it is possible to include the part-in, part-out configuration of Scenario I in Scenario II. Here, chain lengths longer than N^* will likely have some fragments outside the capsid that can be removed by nucleases. This will make the distribution $P(N)$ even more dominated by N^*, but the determination of N^* remains unchanged. Also, for long enough chains, $g(N)$ is primarily determined by the total number of nucleotides in the capsid and is insensitive to the the actual number of chains n_R or the architecture of the polyelectrolyte; see Fig. 5.10. In particular, the results for a 12-arm star and for a linear chain with the same number of nucleotides are essentially identical, indicating that packaging is insensitive to the radius of gyration or degree of branching—two main effects of the RNA secondary structure [52]. In what follows, we briefly describe the components of our SCF model used to obtain $g(N)$, but refer the reader to the Appendix D for details, including the model parameters.

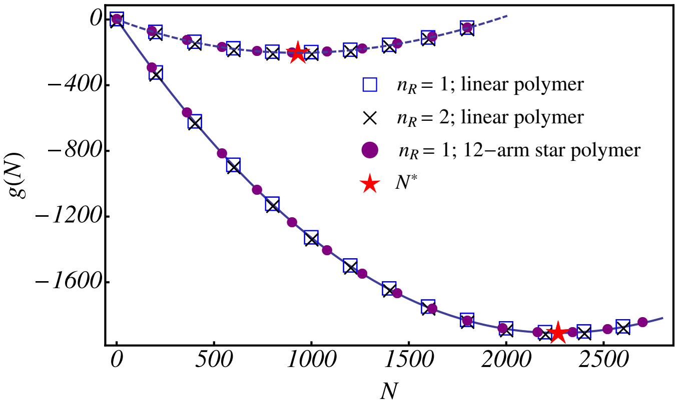

Figure 5.10: T= 4 virus with $Q_P = 1847$e in the presence (solid) and absence (dashed) of the Donnan potential

5.2.3 Model

We approximate the icosahedral viral capsid by a spherical shell of some finite thickness with inner radius r_{cap}, uniform charge density of magnitude c_{cap}, and $n_P = 60$T peptide arms grafted to the inner surface. The capsid is treated as a semi-permeable shell, open with respect to solvent and ions, but closed with respect to the RNA and peptide arms. We represent the flexible RNA molecule, whose persistence length $l \sim 1$ nm is an order of magnitude smaller than the capsid radius, by a discrete Gaussian chain of N monomers, each carrying a unit negative charge and having a volume v_R. The capsid proteins are represented by end-grafted polyelectrolyte chains of uniform charge distribution and are similarly modeled by a discrete Gaussian chain of N_P monomers, each with volume v_P and charge c_P. The solvent molecules are represented by monomers of volume v_s and the monovalent salt ions are taken to be point charges of the elementary charge e. The essential contributions to the model are the chain connectivity, the excluded volume effects, and the electrostatic interactions from all charged species, with total charge density

$$\rho_c = c_{cap}\phi_{cap} - \rho_- + \frac{c_P}{v_P}\phi_P - \frac{\phi_R}{v_R}. \tag{5.31}$$

Here ρ_- is the charge density, assumed to be uniform, of the negatively charged macromolecules outside the capsid. Following the usual SCF derivation (see Appendix B), we obtain the semi-grand

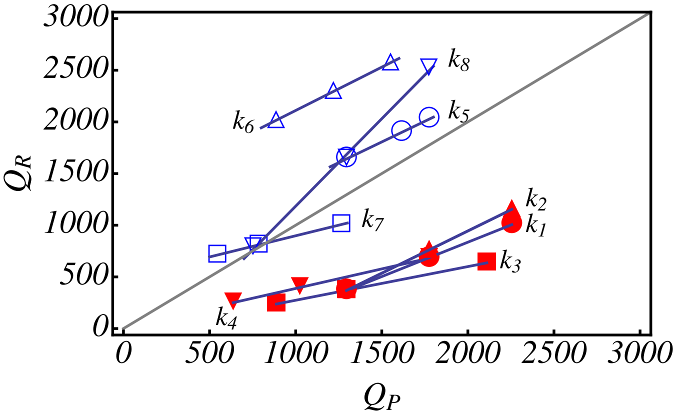

Figure 5.11: $k = \Delta Q_R/\Delta Q_P$ without the Donnan potential (filled): $k_1 = 0.67$ $[N_P]$, $k_2 = 0.82$ $[c_P]$, $k_3 = 0.33$ $[c_{cap}]$, $k_4 = 0.38$ $[r_{cap}]$; and with the Donnan potential (empty): $k_5 = 0.80$ $[N_P]$, $k_6 = 0.84$ $[c_P]$, $k_7 = 0.41$ $[c_{cap}]$, $k_8 = 1.69$ $[r_{cap}]$. The method of varying Q_P is given in brackets; see Appendix D for details.

free energy:

$$\begin{aligned} f_{in} = & -\ln\left(\frac{Z_R}{v_R}\right) - \ln\left(\frac{Z_P^{n_P}}{v_P^{n_P} n_P!}\right) - \frac{\mathrm{e}^{\mu_s}}{v_s} Z_s - \frac{\mathrm{e}^{\mu_\pm}}{v_\pm} Z_\pm \\ & + \int d\mathbf{r}\left[- \sum_{I=R,P,S} \xi_I \phi_I + \psi\rho_c - \frac{\epsilon}{2}(\nabla\psi)^2 \right]. \end{aligned} \tag{5.32}$$

In this expression, the Z_α ($\alpha = R, P, S, \pm$) are the single-molecule partition functions in their respective self-consistent fields ξ_{I}, ψ is the electrostatic potential (measured in reference to a monovalent salt solution when $\rho_- = 0$), and the dielectric constant ϵ depends on the *local* volume fraction of the species.

5.2.4 Results

To understand how each of the different capsid parameters affects the optimal genome length N^*, we begin by varying one parameter at a time, holding all else fixed. For different ways of changing the capsid charges, we obtain the optimal genome charge $Q_R = eN^*$ from the free energy minimization with respect to N. In Fig. 5.11 we show the relationship between Q_R and the total capsid charge Q_P. In all cases, an approximately linear relationship is obtained in the range of charges considered, with a slope $k = \Delta Q_R/\Delta Q_P$.

We first examine the situation in the absence of the Donnan potential, when $\rho_- = 0$ mM and

$c_{\pm} = 130$ mM (filled markers). Changing the charge density of the capsid shell c_{cap} has the smallest effect ($k_3 = 0.33$) on the optimal genome charge, while changing the charge density of the peptide arms c_P has the largest effect ($k_2 = 0.82$). Intermediate to these, we find $k_4 = 0.38$ for increasing the radius of the capsid shell r_{cap} (at fixed grafting density) and $k_1 = 0.67$ for increasing the length of the peptide arms N_P. To understand these different dependencies, we consider a reference T = 4 capsid with a total charge $Q_P = 1440e$ distributed only on the $n_P = 240$ peptide arms. In Fig. 5.12(a), we plot (solid line) the radial density profile for the optimal genome with $Q_R = 769e$. We observe, as expected, a region of RNA density near the capsid surface, with most of the capsid interior devoid of genome. In this case, the main contribution comes from the electrostatic interactions with the peptide arms grafted to the inner surface of the capsid. We subsequently double Q_P by changing N_P, c_P, c_{cap}, and r_{cap} individually. From the density profiles, it is clear that increasing c_{cap} (dashed) has a local effect and the resulting optimal genome only increases to $Q_R = 1171e$. The region where the genome can benefit from additional electrostatic interactions is limited to a concentrated shell at the inner surface of the capsid, where additional layers are hindered by excluded volume from the genome and peptide arms. In contrast, delocalizing the charges onto the peptide arms allows the genome to interact with the entire region of the peptide brush and we find $Q_R = 2011e$ or $Q_R = 1802e$, depending on whether we increase c_P (dotted) or N_P (dot-dashed), respectively. The discrepancy between the two can be understood again from the excluded volume effect. Increasing N_P increases the volume fraction of the protein arms and therefore the excluded volume effect, while increasing c_P does not. Finally, one could double the capsid charge by doubling the number of peptide arms at fixed grafting density, thus increasing r_{cap} (note that this is a hypothetical case, since the number of peptide arms is restricted by the T-number). We find that the density profile is largely the same, except for a shift in position with the capsid shell. Not surprisingly, the optimal genome has approximately doubled with the number of peptide arms, where we find $Q_R = 1488e$. In all cases considered, we find undercharged viruses, where $Q_R/Q_P < 1$.

We next consider the effect of negatively charged macromolecules outside the viral capsid and set $\rho_{-} = 100$ mM, $c_{+} = 130$ mM and $c_{-} = 30$ mM [56]. As usual, the small ions, which can diffuse

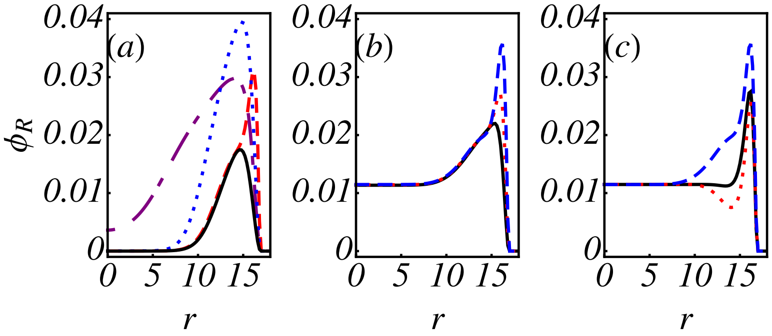

Figure 5.12: Radial density profiles (nm) corresponding to the optimal genome length for a T= 4 virus. (a) For $n_P = 240$, $N_P = 36$, $c_P = 0.167$, and $c_{cap} = 0.0$ (solid) we double the charge by changing one of the following: $N_P = 72$ (dot-dashed), $c_P = 0.33$ (dotted), and $c_{cap} = 0.177$ (dashed). (b) For $N_P = 36$ and $c_P = 0.083$ we increase the capsid charge density: $c_{cap} = 0.00$ (solid), 0.05 (dotted), 0.10 (dashed). (c) For $c_{cap} = 0.10$ without protein arms (solid), with neutral protein arms $N_P = 36$ (dotted), and with charged protein arms $N_P = 36$, $c_P = 0.083$ (dashed)

freely, maintain charge neutrality subject to equality of chemical potential for each of the small ion species across the viral capsid. This combination of charge neutrality with equality of chemical potential gives rise to a negative electrostatic potential (relative to a neutral monovalent salt solution) that makes it favorable for an RNA molecule to be inside the viral capsid. The optimal genome length occurs when the potential inside the capsid becomes comparable to this Donnan potential. In Fig. 5.11 (empty markers), we show that increasing r_{cap} at constant grafting density now has the greatest effect on increasing the optimal genome length, where $k_8 = 1.69$. In contrast, the optimal genome lengths for changing N_P, c_P, or c_{cap} have primarily shifted by a constant, while the slopes $\Delta Q_R/\Delta Q_P$ remain largely unchanged. These observations can be explained from the density profiles in Fig. 5.12(b), where we note that accounting for the negative background charge fills the capsid interior with RNA. When we increase c_{cap}, the concentrated density of RNA near the surface increases (as is the case when $\rho_- = 0$ mM), while the density in the interior remains unchanged. We note that it is possible to increase Q_R simply by increasing the volume of the capsid so that even negative slopes can be obtained, e.g., by increasing r_{cap} while decreasing Q_P.

Lastly, in Fig. 5.12(c), we demonstrate the combined effects of the excluded volume, electrostatics and Donnan potential. We start with a charged capsid shell without protein arms (solid). As

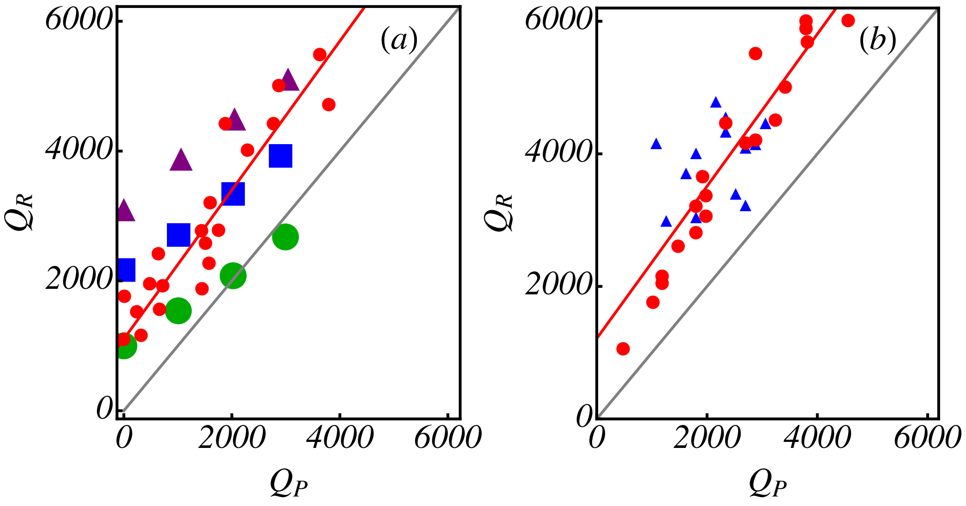

Figure 5.13: (a) Q_R as a function of Q_P for hypothetical small (green circles), medium (blue squares), and large (purple triangles) T = 4 viruses obtained from our model. For a given T-number, Q_P is increased by varying N_P, c_P, and/or c_{cap} using no particular methodology. Also shown is a set of overcharged viruses (red circles) with a slope of 1.1 and intercept 1192. (b) Q_R as a function of Q_P for a selection of WT virus obtained from [39] (red circles) and [41] (blue triangles), with a combined slope of 1.1 and intercept 1214

expected, we find a concentrated density of RNA near the inner surface of the capsid and a lower density throughout the interior of the capsid. We next add neutral protein arms (dotted) to isolate the effect of the excluded volume, and find that the peptide arms repel the RNA from the surface of the capsid, resulting in a decrease in Q_R. If we add back charges to the peptide arms (dashed), we find that the favorable electrostatic interactions overcome the excluded volume effect and, as before, the delocalization of the capsid charges creates an extended region of enhanced RNA density.

From these results, it is clear that no universal relationship exists between the optimal genome length and the total capsid charge. The optimal genome length depends in a nontrivial way on the placement of charges, the peptide arm length, and, importantly, the capsid radius (through the Donnan potential). In real viruses, the variation in the total capsid charge from one virus to another almost certainly occurs by a combination of these parameters. Therefore, very different genome vs. capsid charge relationships can be obtained. To illustrate this, in Fig. 5.13(a) we generate three data sets designated by the green circles, blue squares, and purple triangles, corresponding, respectively, to hypothetical small, medium, and large T = 4 viruses at different values of the total capsid charge. Here the size refers to $r_{cap} = 17$, 22, and 25 nm for small, medium, and large, respectively. Several interesting observations can be made. First, even at zero capsid charge, there is a finite Q_R that depends on the volume of the capsid available to the genome. This is a direct consequence of the negative Donnan potential outside the capsid, which fills the interior with a nearly constant density of genome; see Fig. 5.12(b) and (c). Second, it is obvious that the same total capsid charge Q_P can correspond to multiple values of the optimal genome charge Q_R. Finally, there are multiple ways to connect these 12 data points, each defining a different genome-to-capsid charge relationship. In fact, there is essentially a continuum of points in the general area covered by these 12 points, corresponding to different combinations of N_P, c_P, c_{cap}, and r_{cap}.

5.2.5 Discussion

We have developed a thermodynamic framework for viral assembly and clarified the notion of the optimal genome length as the minimization of an appropriate free energy, which we obtain using SCF theory. Importantly, we have accounted for the Donnan potential due to the presence of charged macromolecules outside the viral capsid and find it to be *essential* for obtaining overcharged viruses. Based on the minimization of the free energy defined in our work, we find that the optimal genome length depends in a nontrivial way on the placement of the capsid charges, the excluded volume inside the capsid and, significantly, the Donnan potential. We conclude that there is no "universal" genome to capsid charge ratio.

What, then, can be made of the apparent linear relationship $Q_R \approx 1.6 Q_P$ that was obtained from 19 wild-type viruses in Ref. [39]? To address this question, we first note that if we exclude the three obvious outliers in the data used in that study, a slope of 1.3 with an intercept of 668 is obtained instead. On the other hand, another set of viruses chosen by Hu et al. [41], when fitted to a linear function, yields a slope of 0.3 and an intercept of 3275. If we combine both sets of data, an apparent linear relationship with slope 1.1 and intercept 1214 is obtained; see Fig. 5.13(b). These data therefore suggest that a fitted linear relationship between the genome and capsid charge is quite sensitive to the choice of which viruses to include in a set; this is consistent with our discussion of Fig. 5.13(a) in the last section. Whether an apparent linear relationship can be obtained if data on all available viruses are compiled remains an open question. However, it is safe to say that there is nothing particularly meaningful about 1.6 being the genome-to-capsid charge ratio.

Nevertheless, it can be seen from Fig. 5.13(b) that all the viruses selected in Refs. [39] and [41] are overcharged. Indeed, overcharged viruses are prevalent in Nature [57]. To understand this, we have generated a set of hypothetical viruses by tuning the parameters (peptide arm length N_P and charge density c_P; and capsid shell radius r_{cap} and charge density c_{cap}) in our model so that only overcharged viruses are obtained. It is in fact possible to make the genome vs. capsid charge relationship for these hypothetical viruses appear similar to real viruses; see Fig. 5.13(a) and (b), red circles. A common attribute of these hypothetical viruses is that the charges on the peptide arms and capsid shell are relatively low. The primary driving force for packaging comes from the Donnan potential, which fills the capsid volume with genome (the finite positive offset in Q_R at $Q_P = 0$ for both the real viruses and our hypothetical viruses is also consistent with this). Thus, the greatest increases in Q_R come from increasing the capsid radius. We emphasize that without the Donnan potential, we cannot obtain overcharged viruses because the genome is limited to electrostatic interactions near the inner surface of the capsid, where the excluded volume effects become an issue. We recognize that many factors contribute in the evolutionary pressure on the genome-to-capsid ratio in naturally occurring viruses. However, in light of our thermodynamic analysis, the prevalence of overcharged viruses in Nature suggests that there may be an evolutionary advantage for viruses that primarily use the Donnan potential, and not the electrostatic attraction between the RNA and the capsomers, for increasing the amount of genome encapsidated. The charges on the capsomers should be just enough to help nucleate viral assembly [38], but not so large as to compromise the structural stability of the capsid.

5.2.6 Conclusion

In conclusion, our study offers a resolution to the issue of a "universal" charge ratio, highlights the importance of the negative Donnan potential in viral assembly, and provides an explanation for the prevalence of overcharged viruses in Nature. The thermodynamic framework developed in this study should be useful for interpreting results from experimental studies of in vitro assembly of viruses and virus-like particles [58–62], as well as for the design of viral vectors for gene therapy, where, in addition to minimizing toxicity, a major goal is to successfully deliver the appropriate amount of therapeutic gene [63]. More generally, because the presence of charged macromolecules in cells is ubiquitous, we expect the associated Donnan effects, much like the well-known crowding effects [64], to significantly influence a wide range of biomacromolecular behaviors and cellular processes.

The authors acknowledge support from the Jacobs Institute for Molecular Engineering for Medicine at Caltech. CLT is thankful for financial support from an NIH training grant.

Appendix D: SCFT Model for the Virus

Consider a spherical capsid shell with uniform charge density of magnitude c_c, whose density profile we define

$$\phi_{cap}(\mathbf{r}) = \frac{1}{2}\left[\tanh\frac{(\mathbf{r} - r_{cap})}{\delta} - \tanh\frac{(\mathbf{r} - r_{cap} - 2d)}{\delta}\right]. \tag{D-1}$$

In this expression, r_{cap} is the capsid radius at the inner surface, $2d$ is the thickness of the shell, and δ is the characteristic width of the interface. The RNA is represented by a polyanion of N identical monomers, each carrying a unit negative charge and having a volume $v_R = 0.22$ nm^3 [65]. The peptide arms are represented by end-grafted polycation chains of N_P monomers, each with volume $v_P =$ 0.065 nm^3 [65] and charge magnitude (per monomer) c_P, where c_P is allowed to vary. The solvent molecules are represented by monomers of volume $v_s = v_P$ and the salt ions are taken to be simply point charges of elementary charge e and valency $z_\pm = 1$. Outside the capsid, we account for the negatively charged macromolecules by setting $\rho_- = 100$ mM. As usual, the salt ions maintain charge neutrality, where $c_+ = 130$ mM and $c_- = 30$ mM (when $\rho_- = 0$ mM we set $c_\pm = 130$ mM).

The particle-based Hamiltonian for the model, which captures the essential contributions to viral encapsidation, is

$$\mathcal{H} = h^R(\{\mathbf{r}\}) + \sum_{i=1}^{n_P} h_i^P(\{\mathbf{r}\}) + \frac{e^2}{2}\int d\mathbf{r}d\mathbf{r}'\hat{\rho}_c(\mathbf{r})C(\mathbf{r},\mathbf{r}')\hat{\rho}_c(\mathbf{r}'). \tag{D-2}$$

The first and second terms account for the chain connectivity of the RNA and peptide arms, respectively. The third term is the Coulomb energy of the system, accounting for the long-ranged electrostatic interactions from the total charge density of all charged species. This includes the capsid shell, peptide arms, RNA, salt ions, and negatively charged macromolecules outside the capsid. $C(\mathbf{r},\mathbf{r}')$ is the Coulomb operator satisfying $-\nabla\cdot[\epsilon(\mathbf{r})\nabla C(\mathbf{r},\mathbf{r}')] = \delta(\mathbf{r}-\mathbf{r}')$, where $\epsilon(\mathbf{r})$ is the dielectric constant, which is spatially varying and depends on the volume fractions of the different species. We set $\epsilon_{cap} = \epsilon_P = 12$ for the capsid [66], $\epsilon_R = 2$ for the RNA [67], and, as usual, $\epsilon_s = 80$ for the solvent.

The semi-grand canonical partition function is obtained by summing over all particle degrees of freedom, including the position of each solvent and ion molecule, as well as the position and conformation of each polyelectrolyte:

$$\begin{aligned}\Xi = &\sum_{n_s,n_\pm=0}^{\infty} \frac{\mathrm{e}^{(\mu_s n_s + \mu_\pm n_\pm)}}{n_s! n_\pm! {v_s}^{n_s} {v_\pm}^{n_\pm}} \int \mathcal{D}\mathbf{r}_i \prod_{j=0}^{n_P}\mathcal{D}\mathbf{r}_j \prod_{k=0}^{n_s} d\mathbf{r}_k \prod_{l=0}^{n_\pm} d\mathbf{r}_l \\ &\times \prod_{\mathbf{r}} \delta\Big[1 - \hat{\phi}_R(\mathbf{r}) - \hat{\phi}_P(\mathbf{r}) - \phi_{cap}(\mathbf{r})\Big]\mathrm{e}^{-\mathcal{H}}.\end{aligned} \tag{D-3}$$

Here, $\hat{\phi}_P(\mathbf{r})$ and $\hat{\phi}_R(\mathbf{r})$ are the instantaneous volume fractions of the peptide arms and RNA molecule, respectively, and the delta functional accounts for the incompressibility (excluded volume) at all positions $\mathbf{r}$ within the system volume.

In SCFT, the first step is to replace the above particle-based model with a field-theoretic model, using a series of techniques related to Hubbard-Stratonovich transformations [44]. This decouples the interactions among particles and replaces them with interactions between single particles and effective fields. The final result for the field-theoretic partition function can be generically written in the form

$$\Xi = \int D\omega \exp(-F[\omega]), \tag{D-4}$$

where F is an effective Hamiltonian that is complex and depends on the (multidimensional) field variable ω. In general, the field-theoretic partition function cannot be evaluated in closed form. The mean-field, or self-consistent field approximation, amounts to assuming that a single field configuration ω^* dominates the functional integral, i.e., $\Xi \approx \exp(-F[\omega^*])$, where $F[\omega^*]$ in our model is given by Eq. (5.32). In this expression, the partition functions are for a single particle in its respective field and are given by

$$\begin{aligned} Z_{\pm}(\psi) &= \int d\mathbf{r} \exp\{\mp\psi e z_{\pm} - u^b_{\pm}\}, \\ Z_s(\xi_s) &= \int d\mathbf{r} \exp\{-v_s \xi_s\}, \\ Z_I(\xi_I) &= \int d\mathbf{r} q_I(\mathbf{r}; N_I), \quad \mathrm{I} = \mathrm{R}, \mathrm{P}, \end{aligned} \tag{D-5}$$

for ions, solvents, RNA, and protein arms, respectively. $Z_{\pm}(\psi)$ contains the Born self-energy of the ions $u^b_{\pm} = z^2_{\pm} e^2 / 8\pi a_{\pm} \epsilon$, where ϵ is the spatially varying dielectric constant. This term cannot be absorbed into a redefinition of the chemical potential for a spatially varying dielectric medium [68]. Although the volume of the salt ions does not enter into the incompressibility, with respect to the self-energy of an ion, we specify $a_{\pm} = 0.18$ nm as the radius. We have introduced the chain propagator $q_I(\mathbf{r}; i)$, where i is the monomer index, to obtain the single-chain statistics of the polyelectrolytes. The propagator accounts for the chain connectivity and the Boltzmann weight due to the self-consistent potential field, with the initial conditions that

$$\begin{aligned} q_R(\mathbf{r}; 1) &= \exp[-v_R \xi_R(\mathbf{r})], \\ q_P(\mathbf{r}; 1) &= \exp[-v_P \xi_P(\mathbf{r})] \delta(\mathbf{r} - r_{cap}). \end{aligned} \tag{D-6}$$

Here the delta function accounts for the fact that the initial monomer of the peptide arm must be grafted to the inner surface of the capsid shell at $\mathbf{r} = r_{cap}$. Because of the lack of inversion symmetry of the peptide arm, it is necessary to introduce a complimentary chain propagator $q^*_P(\mathbf{r}; i)$ that propagates from the free end of the protein arm with the initial condition $q_P^*(\mathbf{r};1) = \exp[-v_P\xi_P(\mathbf{r})]$.

The self-consistent field equations are obtained by requiring that Eq. (5.32) is stationary with respect to variations in the fields. Variation with respect to the volume fraction fields ϕ_I gives,

$$\xi_R = \xi_s - \frac{1}{v_R}\psi - (\epsilon_R - \epsilon_s)\left[\frac{(\nabla\psi)^2}{2} + \frac{z_\pm^2 e^2 c_\pm}{8\pi a_\pm \epsilon^2}\right], \tag{D-7}$$

$$\xi_P = \xi_s + \frac{c_P}{v_P}\psi - (\epsilon_P - \epsilon_s)\left[\frac{(\nabla\psi)^2}{2} + \frac{z_\pm^2 e^2 c_\pm}{8\pi a_\pm \epsilon^2}\right]. \tag{D-8}$$

Here, $c_\pm = \mathrm{e}^{\mu_\pm} v_\pm^{-1} \exp\big\{\mp z_\pm e\psi - u_\pm^b\big\}$ is the ion distribution. Variation with respect to ψ gives,

$$-\nabla(\epsilon\nabla\psi) = \left(c_{cap}\phi_{cap} - \rho_- + \frac{c_P}{v_P}\phi_P - \frac{\phi_R}{v_\mathrm{R}}\right) \pm (z_\pm e c_\pm); \tag{D-9}$$

with respect to ξ_s gives,

$$1 - \phi_R - \phi_P - \phi_{cap} = \mathrm{e}^{\mu_s}\exp\{-v_s\xi_s\}, \tag{D-10}$$

and with respect to ξ_R and ξ_P gives,

$$\phi_R = \frac{v_R}{Z_R}\sum_{i=1}^{N} q_R(\mathbf{r};i)\mathrm{e}^{v_R\xi_R(\mathbf{r})} q_R(\mathbf{r};N-i+1), \tag{D-11}$$

$$\phi_P = \frac{v_P n_P}{Z_P}\sum_{i=1}^{N_P} q_P(\mathbf{r};i)\mathrm{e}^{v_P\xi_P(\mathbf{r})} q_P^*(\mathbf{r};N_P-i+1). \tag{D-12}$$

To correct for over-counting the monomer when the propagators are joined, we include an extra exponential factor in the expressions for ϕ_R and ϕ_P. Numerical SCFT requires solving Eq. (D-7) to Eq. (D-12), together with the chain propagators, iteratively until convergence. From these solutions, the free energy is obtained from Eq. (5.32).

Finally, additional parameters used in Fig. 5.11 are given in Table 5.1 of this Appendix.

	Variable parameter	Fixed parameters
k_1	$N_P = 12, 24, 36$	$c_P, r_{cap}, c_{cap} = 1/3, 17, 0.10$
k_2	$c_P = 1/6, 1/3, 1/2$	$N_P, r_{cap}, c_{cap} = 12, 17, 0.10$
k_3	$c_{cap} = 0.05, 0.10, 0.20$	$N_P, c_P, r_{cap} = 12, 1/6, 17$
k_4	$r_{cap} = 10, 12.8, 17$	$N_P, c_P, c_{cap} = 24, 1/6, 0.10$
k_5	$N_P = 12, 20, 24$	$c_P, r_{cap}, c_{cap} = 1/6, 17, 0.10$
k_6	$c_P = 1/12, 1/6, 1/4$	$N_P, r_{cap}, c_{cap} = 12, 20, 0.05$
k_7	$c_{cap} = 0.05, 0.10, 0.20$	$N_P, c_P, r_{cap} = 12, 1/6, 12.8$
k_8	$r_{cap} = 12.8, 17, 20$	$N_P, c_P, c_{cap} = 12, 1/6, 0.10$

Table 5.1: Additional model parameters used for Fig. 5.11

Bibliography

[1] C. L. Ting and Z.-G Wang, *J. Phys. Chem. B* **113**, 4970 (2009).

[2] C. E. Wyman, *Trends. Biotechnol.* **25**, 153 (2007).

[3] M. E. Himmel, S. Y. Ding, D. K. Johnson, W. S. Adney, M. R. Nimlos, J. W. Brady, and T. D. Foust, *Science* **315**, 804 (2007).

[4] D. K. Y. Poon, S. G. Withers, and L. P. McIntosh, *J. Biol. Chem.* **282**, 2091(2007).

[5] V. Receveur, M. Czjzek, M. Schulein, P. Panine, and B. Henrissat, *J. Biol. Chem.* **277**, 40887 (2002).

[6] I. von Ossowski, J. T. Eaton, M. Czjzek, S. J. Perkins, T. P. Frandsen, M. Schulein, P. Panine, B. Henrissat, and V. Receveur-Brechot, *Biophys. J.* **88**, 2823 (2005).

[7] L. Zhong, J. F. Matthews, M. F. Crowley, T. Rignall, C. Talon, J. M. Cleary, R. C. Walker, G. Chukkapalli, C. McCabe, M. R. Nimlos, C. L. Brooks, M. E. Himmel, and J. W. Brady, *Cellulose* **15**, 261 (2008).

[8] C. Zhao, T. R. Rignall, C. McCabe, W. S. Adney, and M. E. Himmel, *Chem. Phys. Lett.* **460**, 284 (2008).

[9] N. Din, H. G. Damude, N. R. Gilkes, R. C. Miller, R. A. J. Warren, and D. G. Kilburn, *P. Natl. Acad. Sci. USA* **91**, 11383 (1994).

[10] M. Linder and T. T. Teeri, *J. Biotechnol.* **57**, 15 (1997).

[11] A. B. Boraston, D. N. Bolam, H. J. Gilbert, and G. J. Davies, *Biochem. J.* **382**, 769 (2004).

[12] B. W. McLean, M. R. Bray, A. B. Boraston, N. R. Gilkes, C. A. Haynes, and D. G. Kilburn, *Protein Eng.* **13**, 801 (2000).

[13] M. N. Artyomov, A. Y. Morozov, and A. B. Kolomeisky, *Phys. Rev. E.* **77**, 040901 (2008).

[14] M. D. Betterton and F. Julicher, *Phys. Rev. Lett.* **91**, 058105 (2003).

[15] T. Chou, *Phys. Rev. Lett.* **99**, 058105 (2007).

[16] M. E. Fisher and A. B. Kolomeisky, *Proc. Natl. Acad. Sci. USA* **96**, 6597 (1999).

[17] F. Julicher and J. Prost, *Phys. Rev. Lett.* **75**, 2618 (1995).

[18] A. B. Kolomeisky and M. E. Fisher, *Annu. Rev. Phys. Chem.* **58**, 675 (2007).

[19] H. Qian, *Biophys. Chem.* **83**, 35 (2000).

[20] N. G. Van Kampen, *Stochastic Processes in Physics and Chemistry*, 3 ed.; North Holland, (2007).

[21] C. Divne, J. Stahlberg, T. T. Teeri, and T. A. Jones, *J. Mol. Biol.* **275**, 309 (1998).

[22] C. Divne, J. Stahlberg, T. Reinikainen, L. Ruohonen, G. Pettersson, J. K. C. Knowles, T. T. Teeri, and T. A. Jones, *Science* **265**, 524 (1994).

[23] A. Varrot, T. P. Frandsen, I. von Ossowski, V. Boyer, S. Cottaz, H. Driguez, M. Schulein, and G. J. Davies, *Structure* **11**, 855 (2003).

[24] M. D. Betterton and F. Julicher, *Phys. Rev. E* **72**, (2005).

[25] M. Srisodsuk, T. Reinikainen, M. Penttila, and T. T. Teeri, *J. Bio. Chem.* **268**, 20756 (1993).

[26] M. L. Rabinovich, M. S. Melnick, and A. V. Bolobova, *Biochemistry—Moscow* **67**, 850 (2002).

[27] N. Mosier, C. Wyman, B. Dale, R. Elander, Y. Y. Lee, M. Holtzapple, and M. Ladisch, *Bioresource Technol.* **96**, 673 (2005).

[28] J. Lehtio, J. Sugiyama, M. Gustavsson, L. Fransson, M. Linder, and T. T. Teeri, *Proc. Natl. Acad. Sci. USA* **100**, 484 (2003).

[29] M. Peyrard and A. R. Bishop, *Phys. Rev. Lett.* **62**, 2755 (1989).

[30] E. J. Jervis, C. A. Haynes, and D. G. Kilburn, *J. Biol. Chem.* **272**, 24016 (1997).

[31] B. Schuler, E. A. Lipman, P. J. Steinbach, M. Kumke, and W. A. Eaton, *Proc. Natl. Acad. Sci. USA* **102**, 2754 (2005).

[32] E. B. Stukalin and A. B. Kolomeisky, *Phys. Rev. E* **73**, (2006).

[33] D. T. Gillespie, *J. Comp. Phys.* **22**, 403 (1976).

[34] A. F. Voter, *Phys. Rev. B* **34**, 6819 (1986).

[35] H. Metiu, Y.-T. Lu, and Z. Zhang, *Science* **255**, 1088 (1992).

[36] C. L. Ting, J. Z. Wu, and Z.-G. Wang, *Proc. Natl. Acad. Sci USA* **108**, 16986-16991 (2011).

[37] E. Hiebert, J. B. Bancroft, and C. E. Bracker, *Virology* **34**, 492-508 (1968).

[38] J. B. Bancroft, E. Hiebert, and C. E. Bracker, *Virology* **39**, 924-930 (1969).

[39] V. A. Belyi and M. Muthukumar, *Proc. Natl. Acad. Sci. USA* **103**,17174-17178 (2006).

[40] G. S. Manning, *J. Chem. Phys.* **51**, 924-933 (1969).

[41] T. Hu, R. Zhang, and B. I. Shklovskii, *Physica A* **387**, 3059-3064 (2008).

[42] P. van der Schoot and R. Bruinsma, *Phys. Rev. E* **71**, 061928 (2005).

[43] D. G. Angelescu, R. Bruinsma, and P. Linse, *Phys. Rev. E* **73**, 041921 (2006).

[44] G. H. Fredrickson, *The Equilibrium Theory of Inhomogeneous Polymers* (Oxford University Press, New York, 2005).

[45] S. Kurbel, *J. Theor. Biol.* **252**, 769-772 (2008).

[46] D. G. Angelescu and P. Linse, *Phys. Rev. E* **75**, 051905 (2007).

[47] A. Siber and R. Podgornik, *Phys. Rev. E* **78**, 051915 (2008).

[48] R. Zandi and P. van der Schoot, *Biophys. J.* **96**, 9-20 (2009).

[49] C. Forrey and M. Muthukumar, *J. Chem. Phys.* **131**, 105101 (2009).

[50] O. M. Elrad and M. F. Hagen, *Phys. Biol.* **7**, 045003 (2010).

[51] A. Kivenson and M. F. Hagen, *Biophys. J.* **99**, 619-628 (2010).

[52] A. M. Yoffe, P. Prinsen, A. Gopal, C. M. Knobler, W. M. Gelbart, and A. Ben-Shaul, *Proc. Natl. Acad. Sci. USA* **105**, 16153-16158 (2008).

[53] K. M. Ostrow and D. D. Loeb, *J. Virol.* **78**, 2179-2186 (2004).

[54] S. Le Pogam, P. K. Chua, M. Newman, and C. Shih, *J. Virol.* **79**, 1871-1877 (2004).

[55] A. Evilevitch, M. Castelnovo, C. M. Knobler, and W. M. Gelbart, *J. Phys. Chem. B* **108**, 6838-6843 (2004).

[56] B. Alberts, A. Johnson, J. Lewis, M. Raff, K. Roberts, and P. Walter, *Molecular Biology of the Cell* (Garland Science, New York and Abingdon, 2007).

[57] H. W. Ackermann and M. S. Dobow, *Viruses of Prokaryotes* (CRC Press, Boca Raton, 1987).

[58] Y. Hu, R. Zandi, A. Anavitarte, C. M. Knobler, and W. M. Gelbart, *Biophys. J.* **94**,1428-1436 (2008).

[59] S. Mukherjee, M. V. Thorsteinsson, L. B. Johnston, P. A. DePhillips, and A. Zlotnick, *J. Mol. Biol.* **381**, 229-237 (2008).

[60] M. J. Abedin, L. Liepold, P. Suci, M. Young, and T. Douglas, *J. Am. Chem. Soc.* **131**, 4346-4354 (2009).

[61] J. Z. Porterfield, M. S. Dhason, D. D. Loeb, M. Nassal, S. J. Stray, and A. Zlotnick, *J. Virol.* **84**, 7174-7184 (2010).

[62] R. D. Cadena-Nava, Y. F. Hu, R. F. Garmann, B. Ng, A. N. Zelikin, C. M. Knobler, and W. M. Gelbart, *J. Phys. Chem. B.* **115**, 2386-2391 (2011).

[63] M. A. Kay, J. C. Glorioso, and L. Naldini, *Nat. Med.* **7**, 33-40 (2001).

[64] S. B. Zimmerman and A. P. Minton, *Annu. Rev. Biophys. Biomol. Struct.* **22**, 27-65 (1993).

[65] T. Jiang, Z.-G. Wang, and J. Z. Wu, *Biophys. J.* **96**, 3065-3073 (2009).

[66] Z. J. Tan and S. J. Chen, *Biophys. J.* **90**, 1175-1190 (2006).

[67] J. J. Dwyer, A. G. Gittis, D. A. Karp, E. E. Lattman, D. S. Spencer, W. E. Stites, and B. Garcia-Moreno E., *Biophys. J.* **79**, 1610-1620 (2000).

[68] Z.-G. Wang, *Phys. Rev. E* **81**, 021501 (2010).